UNIVERSITY OF NAPLES FEDERICO II

POLYTECHNIC AND BASIC SCIENCES SCHOOL

PHD SCHOOL IN CHEMICAL SCIENCES

Development of theoretical-computational methods for the study of photophysics and photoreactivity occurring far from the Franck-Condon region

---

*PhD Candidate: Federico **Coppola***
*Supervisor: Prof. Nadia **Rega***

A thesis submitted in fulfillment of the requirements
for the degree of Doctor of Philosophy

in the

TheCraft - Theoretical and Computational Chemistry @ UniNa
Department of Chemical Sciences

XXXII Cycle 2017/2020

*Coordinator: Prof. Angela **Lombardi***

Declaration of Authorship

I, Federico Coppola, declare that this thesis titled, Development of theoretical-computational methods for the study of photophysics and photoreactivity occurring far from the Franck-Condon region, and the work presented in it are my own. I confirm that:

- This work was done wholly or mainly while in candidature for a research degree at this University.
- Where any part of this thesis has previously been submitted for a degree or any other qualification at this University or any other institution, this has been clearly stated.
- Where I have consulted the published work of others, this is always clearly attributed.
- Where I have quoted from the work of others, the source is always given. With the exception of such quotations, this thesis is entirely my own work.
- I have acknowledged all main sources of help.
- Where the thesis is based on work done by myself jointly with others, I have made clear exactly what was done by others and what I have contributed myself.

Signed:

Date:

Abstract

Federico COPPOLA

Development of theoretical-computational methods for the study of photophysics and photoreactivity occurring far from the Franck-Condon region

The main vibrational spectroscopy techniques are based on the processes of infrared radiation absorption and Raman scattering, which are daily used by chemist to provide deep information on chemical structures and physical phases of matter even in complex chemical environment. Laser technology has contributed greatly to the evolution of spectroscopy, introducing even the time domain (from *as* to *ps*) associated with the frequency domain increasing the resolution and overcoming some limitations of ordinary radiative sources allowing the observation of ultrafast and transient phenomena in real time. Such advanced time resolved and non-linear vibrational spectroscopies such as, i.e., Femtosecond Stimulated Raman spectroscopy and Transient absorption which are part of the present work, can give further insight at atomistic/molecular level on very short time scale about excited state structural dynamics, proton and electron transfer reactions, isomerizations and so on. The interpretation of vibrational spectra and the subtle relationships between the experimental data and the molecular dynamics can be very challenging to unravel because of numerous concomitant effects (ultrafast transient phenomena, broadening, vibrational couplings, complex matrices) for this reason it is source of debate. In this regard, the atomistic-level description provided by a reliable and careful theoretical-computational approach can be a valuable aid in interpretation, prediction and further clarification of experimental evidence. The aim pursued in this PhD project is to study the pivotal phenomena behind photophysical and reactive events affecting photoactive molecules in condensed phase, using a reliable and accurate theoretical-computational

methodology. In this work we focus on photoinduced charge transfer reactions of two non-covalent π-stacked dimers, which have been recently characterized by means of Femtosecond Stimulated Raman Spectroscopy that show a complex and intriguing photophysical behavior both in the ground and excited states. In order to unravel the vibrational dynamics of key vibrational modes and relaxation processes occuring far from Franck-Condon region we propose a non-canonical theoretical approach based on the Wavelet Analysis of suitable time dependent signals obtained through *ab-initio* molecular dynamics simulations, within methods rooted in Density Functional Theory (DFT) and it's time dependent version TD-DFT - as the best compromise between accuracy and computational demands - within the adiabatic approximation for the ground and electronic excited state description. Our aim is to know what happens on the ultrafast time scale of electronic excited states translating the inherently anharmonic nuclear motion in terms of vibrational couplings and relaxation processes along with the time domain. We also linked vibrational fingerprints to electronic properties, as ultimate goal. We were able to careful assign the ground and excited state vibrational frequencies, to quantify the anharmonic vibrational couplings among those vibrational modes that play a key role in the photophysics at stake. By analyzing the temporal evolution of some selected structural parameters, we have identified the vibrational modes that most affect the adiabaticity between the electronic states involved contributing to the activation of non-radiative relaxation channels of the entire charge transfer complex from the excited to the ground state. This PhD project involved a period of study and training abroad: at the University of Minnesota under the guidance of Prof. R.R. Frontiera we investigated a recently synthetized electron acceptor, which presumably undergoes to Singlet Fission when photoexcited. We used Transient Absorption and Femtosecond Stimulated Raman microscopy to unveil the structural dynamics and identify the vibrational fingerprint probes of the formation and separation of triplets in crystalline phase. Along with this experimental study, a suitable model and computational method is being developed that can provide an atomistic description and further insights. In conclusion, the study of transient and far from equilibrium processes, which represent an emerging challenge in the field of physical chemistry, is the cornerstone for a deep knowledge of excited state chemistry which can be monitored and handled to pave the way for a rational design of more performing photovoltaic, efficient light harvesting and sensor devices.

Acknowledgements

I would like to thank my supervisor prof. Nadia Rega for supporting me in this project, for her patience and for all the time she dedicated to my education. I am extremely grateful to you for all the opportunities I have had. I would like to thank Dr. Alessio Petrone for all the work done together and for all that he also taught me and my adventure mate the stoic Dr. Fulvio Perrella. I wish Mara and Luigi a good job and a great future in research. I would like to express my gratitude to all the past members of this group, Dr. Greta Donati, Dr. Umberto Raucci and Dr. Maria Gabriella Chiariello who initially accompanied me on this adventure, I wish you a bright future. I thank prof. Luigi Petraccone for our scientific discussions during these three years and for all the suggestions and recommendations. Special thanks go to prof. R.R. Frontiera and her awesome research team for making me feel at home during my stay in Minneapolis and for everything you have taught me. Thanks for contributing to this work. None of this work would have been completed without the loving support of my family for understanding me during all the ups and downs of this work.

Financially this work was supported by MIUR (Italian Ministry of Education, University and Research) national scholarship for the Ph.D. program in Chemical Sciences.

Minneapolis (MN), January 2020

F.C.

Contents

List of Abbreviations

AIMD	**A**b-**I**nitio **M**olecular **D**ynamics
ADMP	**A**tom **C**entered **D**ensity **M**atrix **P**ropagation
AE	**A**bsolute **E**rror
B3LYP	**B**ecke **3**-parameters **L**ee **Y**ang **P**arr
BOMD	**B**orn-**O**ppenheimer **M**olecular **D**ynamics
CAM-B3LYP	**C**oulomb-**A**ttenuated **M**ethod **B**ecke **3**-parameters **L**ee **Y**ang **P**arr
1ClN	**1-Cl**oro**N**aphtalene
CI	**C**onical **I**ntersection
COM	**C**enter **O**f **M**ass
C-PCM	**C**onductor-like **P**olarizable **C**ontinuum **M**odel
CT	**C**harge **T**ransfer
cWT	**c**ontinuous **W**avelet **T**ransform
DCM	**DiC**hloro**M**ethane
DFT	**D**ensity **F**unctional **T**heory
DimethoxyASI	2-Methoxy-9-(4-methoxyphenil)-10-phenylindeno[1,2,3-fg]-tetracene
EDA	**E**lectron **D**onor **A**cceptor
ES	**E**xcited **S**tate
ET	**E**lectron **T**ransfer
f	Oscillator Strength
FSRS	**F**emtosecond **S**timulated **R**aman **S**pectroscopy
FT	**F**ourier **T**ransform
FWHM	**F**ull **W**idth at **H**alf **M**aximum
GD3	**G**rimme's **D**ispersion correction
GS	**G**round **S**tate
H-F	**H**artree-**F**ock
HMB	**H**exa**M**ethyl**B**enzene
HOMO	**H**ighest **O**ccupied **M**olecular **O**rbital
IC	**I**nternal **C**onversion
ISC	**I**nter **S**ystem **C**rossing

LUMO	**L**owest **U**noccupied **M**olecular **O**rbital
MDs	**M**olecular **D**ynamics
MOs	**M**olecular **O**rbitals
NACs	**N**on **A**diabatic **C**oupling matrix elements
NBO	**N**atural **B**ond **O**rbitals
NMs	**N**ormal **M**odes
NTOs	**N**atural **T**ransition **O**rbitals
PCM	**P**olarizable **C**ontinuum **M**odel
PES	**P**otential **E**nergy **S**urface
RR	**R**esonance **R**aman
SCF	**S**elf **C**onsistent **F**ield
SF	**S**inglet **F**ission
SP	**S**ingle **P**oint
TA	**T**ransient **A**bsorption
TCNE	**T**etra**c**ya**n**o**e**thylene
TCNQ	7,7,8,8-**T**etra**c**ya**n**o**q**uinodimethane
TD-DFT	**T**ime-**D**ependent **D**ensity **F**unctional **T**heory
TMB	1,2,4,5-**T**etra**m**ethyl**b**enzene
VEE	**V**ertical **E**xcitation **E**energy
XCfunctional	E**X**change - **C**orrelation functional

To those who believed in
me...

1 Introduction

1.1 Far from equilibrium processes in chemistry and theoretical-computational challenges

Despite the long millennial history of chemistry, the atomic motion during a chemical reaction has not been possible to observe in real time. The breaking and formation of chemical bonds, as well as structural changes occur very fast, the time required is about 100 fs. These ultrafast transformations involve the movement of atomic nuclei and electrons. In 1900 the technological advancement has allowed to reach time intervals below the *second* time scale and since the 80s it has been possible to reach the femtosecond time scale (1 fs = 10^{-15} s), i.e. the time scale of motion of atoms and molecules, thanks to the invention of lasers that revolutionised the scenario. [1, 2, 3] This made it possible to extend the arrow of time to orders of magnitude lower (from pico to femto) and to make the measurement of transient dynamics, routinely. The advent of this temporal resolution kicked off the so-called Femtochemistry field, Zewail's pioneering work earned him the Nobel Prize in Chemistry in 1999. [4, 5, 6, 7] Femtochemistry deals with observing nuclear motion and is based on the use of optical spectroscopies in pump-probe configuration (or combined techniques) to trigger chemical reactions and follow their temporal evolution, mostly, following the change in molecule's absorption spectrum. Initially the studies were focused on model molecular systems (alkali halide reactions) to establish the correct experimental procedures and develop the theoretical foundations underlying the observed processes and then embraced a wide range of chemical problems, from the study of elementary reactions and transition states to the study of complex reactions of organic chemistry, proton and electron transfer phenomena, up to the dynamics of complex biological systems. Currently, thanks to Femtochemistry, it has been possible to study covalent, ionic, metallic bonds and weaker ones

such as hydrogen bonds and weakly van der Waals bounds. The complexity has gradually increased from simple diatomic molecules to proteins and nucleic acids as well as in different phases of matter. From isolated systems, to clusters, to liquids, in solids, to the interface and so on. Many advances in the field of Femtochemistry have been made possible by new and improved theoretical tools. Furthermore theoretical tools have also reached a predictive power that guide the experimentalist in designing new experiments. Likewise, recent developments in the theory of nonlinear optics [8, 9] paved the way for modern and powerful multidimensional spectroscopic techniques that have extended Infrared and Raman techniques to new dimensions. [10, 11, 12, 13, 14, 15, 16, 17] This has allowed chemists to go beyond deciphering and elucidating the molecular structure and vibrational relaxation processes towards studying the vibrational couplings quantitatively. [18, 19] Recently, new techniques have been developed to probe molecular structural dynamics which provide a direct way of observing the dynamic evolution of a chemical system by offering the possibility of recording a molecular movie. [20, 21, 22, 23, 24] The methodologies developed to date are very versatile and general, and extend investigations even in the excited state as well as in the fundamental state. Combined with several other spectroscopy techniques the complete sequence of events of a biological function from the first instants to the final outcome is now described. [25, 26, 27] Further progress of chemical interest which deserves to be mentioned, albeit briefly, concerns the recent implementations aimed at the study of electronic dynamics. [28, 29] Electrons are the main actors in forming and transforming chemical bonds and travel at such a speed that a temporal resolution of the order of attoseconds is required (1 as = 10^{-18} s). The attosecond technology has offered a number of tools to observe the ultrafast motion of electrons and could give the possibility in the near future to precisely control electronic dynamics in complex systems, extending the possibility to a new way of doing and manipulating chemistry, the era of the attochemistry. Currently the scientific literature on the subject is more and more vast. [30, 31] Even the development of modern attochemistry would not have been possible without the fundamental theoretical foundations. Modeling and numerical simulations have allowed on the one hand the development of new experiments and on the other hand they help in the prediction and understanding of complex data analysis although the accurate description of what happens following attoseconds pulses is still a challenge. In order to predict and understand the complex outcome of such experiments, the resolution of time-dependent Schrödinger equation

for all the electrons and nuclear degree of freedom immerse in a strong electric field neglecting the powerful Born-Oppenheimer approximation, become mandatory. But the exact solution is computationally inaccessible except for very simple systems. Recently some methods have been developed to describe dynamics on multiple surfaces [32, 33, 34, 35, 36] and some of them allow to take into account the effect of the laser field. [37, 38, 39] To the full quantum mechanical treatment an appealing alternative approach is the *ab-initio* molecular dynamics that relies on semiclassical trajectories to describe the nuclear dynamics and an ab-initio treatment of the electronic structure. [40, 41, 42]

1.1.1 Normal modes definition from molecular dynamics

The *ab-initio* molecular dynamics (MD) and in particular the molecular dynamics based on the Extended Lagrangian methods are extremely important and revolutionary in the MD framework because they have given access to the study of very large systems. The first implementation is to be attributed to Car and Parrinello, [43, 44] methods such as Born-Oppenheimer (BO) and Ehrenfest molecular dynamics also belong to this family approach, too. [45, 46, 47, 48] The basic idea is to consider the electron density as a dynamic variable by introducing in addition to the real phase space, a fictitious phase space by introducing an inertia (a fictitious mass) to the electron density. By critically choosing the fictitious mass, the Born-Oppenheimer approximation is still valid, the nuclear motion is decoupled from the electronic motion, but it is possible to propagate nuclei and electrons simultaneously. The term *ab-initio* does not configure a quantum molecular dynamics, the dynamics is still classic in fact the nuclear motion (and therefore the equations to be integrated) does not differ from the classical MD. On the contrary, the energies and its first derivative with respect to the coordinates (forces) are calculated through the electronic structure methods using an integrators to integrate Newton's equations of motion. The energies and the forces acting on the nuclei are computed from electronic structure calculation performed on-the-fly at every step of the dynamics trajectory, the SCF-iteration procedure is calculated only at the first step. According to the variational principle, it is possible to solve the electronic problem (by means of DFT or post-HF methods) for each point of the Born-Oppenheimer single PES starting from an initial configuration of the nuclei by calculating energy and forces from first principles. With these methods we consider the temporal evolution of the nuclei and for

each instant the electron density is perfectly relaxed to them, we are not following the temporal evolution of the Schrödinger equation in which electrons and nuclei are described by the respective wave functions, therefore is not a quantum dynamics. In this work we used the propagation scheme known as Atom-centered Density Matrix Propagation (ADMP) [49, 50, 51, 45, 52] rather than the Car-Parrinello dynamics. In this representation, the density matrix it is constructed using the coefficients of the gaussian based atomic orbitals and are centered on the nuclei. The ADMP scheme is more suitable for the description of molecules (non-periodic systems) as well as performing hybrid Quantum Mechanical / Molecular Mechanic (QM / MM) methods if necessary. Moreover, the problem of parameterization of the force fields of molecular mechanics is avoided. With AIMD it is possible to access time scales of the order of pico or sub-picoseconds, rather than nanoseconds time scale of classical MD, and therefore study reactivity, fast photophysical events, rotational and vibrational motion, charge transfer events, as well as having an accurate statistics of nuclear motion up to hundreds of atoms. The *ab-initio* molecular dynamics simulations presented below refer to the ADMP scheme for the fundamental electronic state and BO/TDDFT in the linear response formalism, for the simulations of the excited electronic state.

Vibrational spectroscopy techniques (such as IR and Raman) allow to have deep information about the molecular structure, also taking into account the effects of the chemical environment. The interpretation of vibrational spectra can be very challenging to disentangle due to numerous concomitant effects (broadening, vibrational couplings, complex environment). Computational spectroscopy and in general a theoretical-computational approach can be a valuable aid in interpretation, prediction and for further clarification. The resolution of the vibrational problem relies on a system of non-interacting molecules by decoupling the nuclear degree of freedom from the electronic one (Born-Oppenheimer adiabatic approximation); the models of the harmonic oscillator and the rigid rotor also allow the vibrational motion to be treated separately from the rotational motion. The so-called *Hessian-based* methods solve the vibrational problem from a quantum mechanical point of view of vibrational states. They are based on a stationary-state picture of the system, indeed the geometry used for vibrational analysis must be a minimum on the potential energy surface, then differences with the experimental data is often the result (in addition to methodological errors) of an

inadequate inclusion of anharmonic effects. Often the quickest solution consists in scaling the vibrational frequencies through suitable scaling factors. [53, 54, 55] Nowadays, harmonic and anharmonic vibrational frequencies can be straightforwardly computed for isolated or condensed-phase systems up to medium-sized molecules. [56, 57, 58, 59, 60, 61] The resolution of the vibrational problem by a quantum mechanical approach can be not suitable when large molecular systems like proteins or other biological macromolecules are considered especially if they are characterized by large number of degrees of freedom (such as in condensed phase), finite temperature effects, strong anharmonicity and not negligible coupling between modes. In these cases, an alternative approach able to overcome these limitations should be invoked. Vibrational spectra can be alternatively computed exploiting dynamic and statistical mechanic approaches based on the Fourier Transform analysis of atomic velocities or dipole moment time correlation functions. [62, 63, 64, 65, 66, 67] In principle it is possible to obtain a complete description of the vibrational modes activated at the temperature of the molecular dynamics simulation, the couplings between vibrational modes as well as anharmonicity are intrinsically included. AIMD approach is essential to obtain a reasonable physical picture of the system under study. From the AIMD trajectories the so-called *generalized-normal modes* can be extracted and their relative vibrational spectra (comparable to IR and Raman spectra) are computed by means of the Fourier Transform. [68, 69, 70, 71, 72] In the following we describe the main features of our approach comparing our findings with more rigorous methods, based on quantum mechanical anharmonic treatment and experimental findings when available. We get the so-called *generalized-normal modes* by using covariances of cartesian atomic velocities extracted from AIMD simulations. The basic assumption is that *generalized-normal modes* correspond to uncorrelated momenta of atoms. These modes are described by the vector $\mathbf{Q} = \{Q_i, i = 1,3N\}$ where N is the number of atoms. The protocol employed for the ground state sampling consists of: for each step of the trajectory, rotational modes of the system have been projected out by a minimization procedure of the angular momentum with respect the orientation assumed by the molecule in the first time step - in this work, the angular momentum minimization procedure required for this analysis (see Ref. [72] for a more detailed discussion) was applied only for coordinates and momenta of the subsystem of interest rather than for the entire complex, since in this way an improved description (less noisy spectra and smoother peaks) of the vibrational modes composition and relative spectra have been

obtained. *Generalized-normal modes* **Q** are obtained by the transformation matrix **L**, which diagonalizes the covariance matrix of the mass weighted atomic velocities **K**, with elements:

$$K_{ij} = \frac{\sqrt{m_i m_j}}{2} \left\langle (\dot{x_i} - \langle \dot{x_i} \rangle) \left(\dot{x_j} - \left\langle \dot{x_j} \right\rangle \right) \right\rangle \tag{1.1}$$

where i and j run over the $3N$ Cartesian coordinate and $\dot{\mathbf{x}}$ are the mass-weighted displacements from an average structure $\langle \mathbf{x} \rangle$. The normal modes have been obtained as eigenvectors of **K** while eigenvalues of **K** provide averaged kinetic energy for each mode.

For the excited state *ab-initio* molecular dynamics simulations we assume that the unitary transformation matrix **L** is unchanged with respect to the ground state quantity, this approximation allowed us to project the excited state mass weighted atomic velocities along ground state *generalized-normal modes* vectors:

$$\dot{Q}'(t) = L^{\dagger} \dot{x}' \tag{1.2}$$

The system velocities have been projected along each normal mode in order to obtain the time evolution of the normal mode $\dot{\mathbf{Q}}$ and then their autocorrelation functions have been calculated:

$$P_k(\omega) = \int_{-\infty}^{+\infty} \left\langle \dot{Q}_k(0)) \cdot \dot{Q}_k(t) \right\rangle e^{-i\omega t} dt \tag{1.3}$$

The vibrational frequencies of specific internal coordinates (time evolution of selected structural parameters) were also investigated, when necessary. At this point we can sketch the advantages and disadvantages of *static* and *dynamical* approaches in solving the vibrational problem. The calculation by the static approach can extend up to small-medium sized molecules and is not feasible for large molecules or in solution, the anharmonic contributions can be included variationally, self-consistently and perturbatively and recovered almost entirely. The anharmonic couplings are obtained from the study of the cubic and quartic force constants, the combination bands and the overtones are obtained automatically. The time-dependent approach, from *ab-initio* molecular dynamics, allows to calculate the electronic structure via the extended Lagrangian scheme and in principle, the systems under study are not limited by the number of atoms. Unlike static methods, there is a correct description of floppy modes (i.e. hydrogen bonds), anharmonic intensities

and fundamental bands. The drawbacks of the two classes of methods are: the calculation of the electronic structure implies the SCF convergence, the PES is approximate, the anharmonic calculation is limited by the size and the floppy modes are poorly described, in the non-dynamic approach. While from AIMD the anharmonic contribution is partially recovered, the anharmonic couplings are, at the moment, qualitative, and the determination of combination bands and overtones is laborious. Our theoretical-computational protocol relies on the Wavelet Transform (described below, in the next section) for the analysis of suitable signals extracted from the AIMD trajectories. Due to its ability to catch the instantaneous time-frequency correlations it is now possible discerning whether and what modes are coupled, when a specific mode is activated afterward the shutdown of another. In this way theoretical calculations can get closer to modern time-resolved spectroscopy techniques.

1.1.2 Wavelet-based transient vibration analysis

Most of the natural physical signals (acoustical, electrical, optical) is inherently non-stationary, this means that it is variable in time domain. A non-stationary signal is well represented by a combination of periodic functions and in order to understand origin and properties contained, it must be analysed. Transforms are mathematical processes adequate to get such information; a certain number of transforms exists and one of the most employed in the chemical field is the Fourier Transform (FT). In this work, for example, we computed the FT of the normal modes velocities autocorrelation function $C(t)$ to get the related vibrational power spectra:

$$F(\omega) = \int C(t) e^{-i\omega t} dt \tag{1.4}$$

where ω is the angular frequency. Fourier analysis is suitable when a signal is stationary-type, i.e., that does not vary in time. The FT gives an average description being local in frequency and global in time preventing to know when an event has occurred. When dealing with non-stationary signals, such as signals extracted from excited state non-equilibrium molecular dynamics, the Fourier analysis becomes no more appropriate by construction because the time dependence of the signal is not retained, for this reason a different kind of analysis is strictly necessary for our purposes. A significant contribution was introduced by Gabor (Short Time Fourier Transform, STFT) [73]

accommodating the FT to the analysis of small temporal range, decomposing the signal via the "windowing" procedure. In the STFT a gaussian window function g(t) is introduced in the standard FT and therein the signal is assumed to be stationary. This technique has been recently used to unravel the role of nuclear dynamics on plasmon lifetime. [74] The drawback (Gabor limit) of this approach is that, the resolution is the same for all frequencies present in the signal. The nature of many signals, instead, requires a more flexible analysis in order to determine more accurately both *time* and *frequency* domains with higher resolution. Simultaneous localization of a signal both in time and frequency domain is an appreciate feature also for comparisons with modern time-resolved spectroscopic signals. In this context the Wavelet Transform, seems to be the best fit to analyze the signals extracted from time-dependent MD simulations. Fourier analysis consists in decomposing a signal into sinusoids of different frequencies and, similarly for the Wavelet based analysis, the signal decomposition is carried out by means of wavelet functions. However many key differences characterize such two techniques. A time resolved vibrational protocol was applied to analyze time dependent quantities extracted from AIMD trajectories, relying on the continuous Wavelet Transform (cWT). [75, 76] At variance with other available techniques for signal analysis, such as Fourier Transform (FT) and Short-Time Fourier Transform, the continuos wavelet transform allows for multiresolution analysis enabling to observe the underlining peaks in the time domain. A comparison of the different resolution achieved from STFT and the WT is well described in the following figure 1.1.

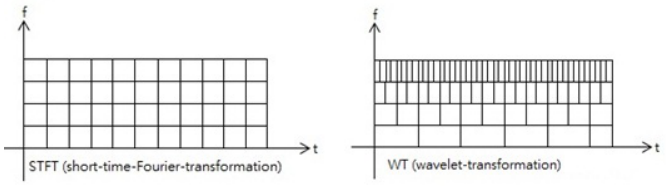

Figure 1.1. Comparison of STFT and WT in time-frequency plane

This technique has been vastly used to obtain accurate analysis for transient phenomena such as time-resolved fluorescence [77], reactivity in excited states [78, 79], polaron pairs formation in excited semiconducting organic polymers [80] and photorelaxation in solution [81]. The cWT acts on

a given time-dependent signal *S(t)* in accordance with the relation reported below:

$$W(a,b) = \int S(t)\psi_{a,b}(t)dt \tag{1.5}$$

The mathematical expression of a wavelet *mother* function is the following one:

$$\psi_{a,b}(t) = |a|^{-\frac{1}{2}}\psi\left(\frac{t\text{-}b}{a}\right)(a,b \in Re; a > 0) \tag{1.6}$$

$|a|^{\frac{1}{2}}$ is a normalization factor, a is the scale parameter, proportional to the inverse of frequency and b is the translation parameter which shifts the ψ function along the time axis for each value of a. By varying these two parameters it is possible to analyze a given signal evolution extracted from AIMD simulations preserving the temporal information in addition to the frequency one. In the present work we chose the Morlet wavelet as *mother* function [76], ψ which provides optimal time-frequency resolution for the nature of our time-series according to previous studies [77, 78, 79, 80, 81]. The cWT of signals computed from AIMD trajectories in both ground and first singlet excited states, these last ones conducted considering an average over the excited state trajectories, are presented as 2D (perspective) maps to facilitate reading. The time domain was reported on the x-axis in femtosecond (fs), on the ordinate the frequency range in wavenumber (cm^{-1}) with a frequency resolution of about 30 cm^{-1} and the color scale states for the magnitude $|W(\nu,t)^2|$ of the power spectrum.

1.2 The new frontiers of vibrational spectroscopy

All chemical, physical and biological processes that occur on timescales of less than microsecond are generally referred to as *ultrafast processes*. The most challenging and interesting processes take place within sub ps - fs time regime, which is why they are difficult to access and to understand. [82] To follow an ultrafast process is required an adequate temporal resolution which can be achieved through a fine control of the light sources during the experiments. Raman vibrational spectroscopy relies on the inelastic scattering of photons and is a powerful spectroscopic techinque that provides chemical

and structural information about chemical systems regardless of the physical phase. Today is employed, along with numerous variations that exist [83], in many various field as chemistry, life sciences, geology and because it can be used remotely (with the use of fibre optic) and is a non-destructive technique, in cultural heritage. [84, 85, 86] One of its downsides is that spontaneous Raman scattering is typically very weak (small cross-section) which can be hidden by fluorescence, and it is also difficult to obtain Raman spectra with a favorable signal-to-noise ratio. The *pump-probe* and nonlinear implementations has made this technique sensitive to the study of the time-resolved structural dynamics. In such an experiment, a *pump* pulse excites and induces modifications to the molecular structure of the sample under examination and the structural evolution of the system is subsequently interrogated by a *probe* pulse, whose wavelength is close to resonance with an electronic transition. By varying the time delay between the two pulses, one can retrieve the time scales of the ongoing processes. This setup is limited only to the picosecond domain, therefore it is not suitable for the study of events that occur between tens of fs and 1 ps.[87]

For the purposes of this research work, we therefore need a spectroscopic technique capable of probing the molecular structure on the time scale of atomic motion. In recent years some research work [77, 81, 78, 79] carried out in this research group has often interfaced with the experimental evidence obtained through advanced time-resolved vibrational spectroscopic techniques, first of all the Femtosecond Stimulated Raman Spectroscopy (FSRS) which has allowed over time to develop a computational protocol aimed at simulation and detailed analysis of such experiments. FSRS is a new ultrafast spectroscopic technique which allows access to vibrational structural dynamics with a high temporal and spectral resolution (up to 50 fs and 10 cm^{-1}, respectively) [88, 89, 90], as well as the direct observation of anharmonic couplings in the time domain. [91] These incredible features paved the way for the study of reactive events in the time domain in small molecules up to complex biological systems. [25, 92, 27, 93, 94] The concept behind this technique in the standard implementation is that a femtosecond pump pulse or *actinic* pulse excites a ground state population to an excited state initiating the photochemistry of interest. The structural evolution onto the reactive potential energy surface is then interrogated, after a variable time delay, by the simultaneous interaction of a narrow bandwidth picosecond Raman pulse and a broadband femtosecond continuum Raman probe which are responsible of

the stimulated Raman scattering.

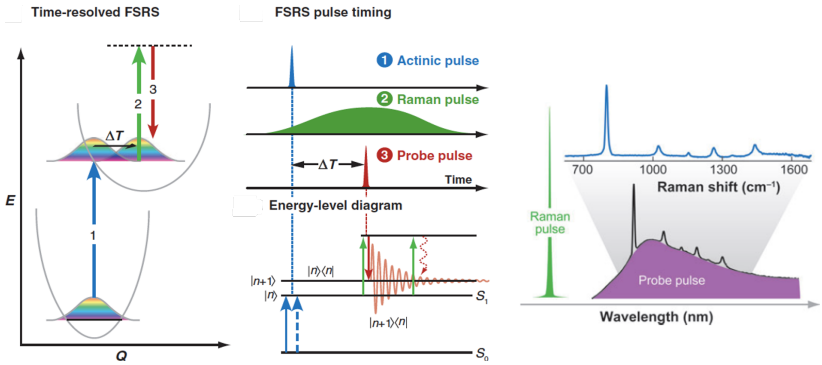

Figure 1.2. Left panel: pictorial potential energy surfaces involved in a typical FSRS experiment. A fs-actinic pulse (1) triggers the photophysical/photochemical process of interest. After a time delay ΔT, the interactions with ps-Raman pulse (2) and fs-Probe pulse (3) create a vibrational coherence on the excited state PES (central panel, FSRS in the time domain). At a later time, another interaction with ps-Raman pulse leading to emission of a photon at the same energy as the vibrational transition. Right panel: the ground state Raman spectrum of cyclohexane is generated by the narrow bandwidth Raman pulse (green) and a broadband Raman probe (purple) on the red edge of Raman pump. When both pulses are sent to the sample, features appear on the top of probe spectrum (blue). Images from Ref.[88].

In the present PhD project, we used Femtosecond stimulated Raman spectroscopy to provide new insight about the structural dynamics occurring during the Singlet Fission event in a brand-new molecule promising in the organic photovoltaic field. Our results are discussed in Chapter 4, a detailed experimental procedure of the FSRS setup is reported in the Appendix A.

1.3 Charge transfer systems

Following the light-matter interaction, a chemical species it is promoted from the fundamental electronic state to an electronically excited one which has its own chemical and physical properties. The excess of energy it is readily distributed in the various degrees of freedom to which the system has access, then follow multiple and competitive relaxation pathways - to photoreactivity, to radiative or radiationless energy dissipation - until it returns to thermodynamical equilibrium state. A comprehensive schematization of the photophysical processes and the time scales within which they occur is reported in the well-known Jablonski energy diagram in 1.3. This study aims to investigate about the vibrational energy redistribution in far from

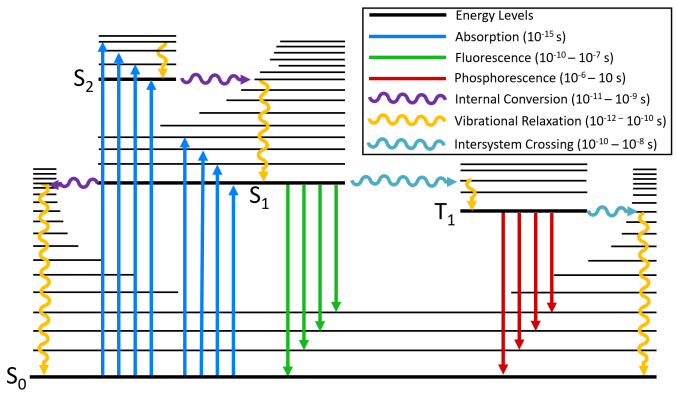

Figure 1.3. Jablonski energy diagram. The electronic states are indicated with thick lines, vibrational states with thinner lines. Straight arrows are for radiative transitions, wavy arrows indicate non radiative processes. The legend (inset) shows the time intervals with which these processes take place.

equilibrium processes through a theoretical and computational approach tailored to simulate and disentangle, at molecular level, the experimental data from modern ultrafast time-resolved spectroscopic techniques. In this context, discrete molecular systems that undergo to significant rearrangements of electron density as in charge transfer (CT) state, are of particular interest although their modeling is actually quite challenging due to the number of crucial issues to consider as geometries, weak interactions, electronic structure and dynamics. Charge transfer process is an ubiquitous phenomenon of paramount importance in chemistry, [95, 96] biology [97, 98] and materials science [99, 100] and is a very active area of research due to the constant demand for new forms of energy based on chemical devices more durable, safe and performing, numerous studies are now being conducted on charge transfer systems to increase their potential and attempt to replace costly rare-earth metals and / or toxic materials. Such a process can be photoinduced at the interface between two materials [101, 102] in conjugated polymers [103, 104], intra- [105, 106, 107, 108] or intermolecularly [94, 93] and in metal-ligand coordination complexes. [109, 110, 111] An *intermolecular* charge transfer complex - the focus of the present work - is an intensely coloured molecular system formed by the weak interaction of a π-electron donor (D) and π-electron acceptor (A). Weak D-A complexes have attracted interest since the discovery of the conductive metal-like properties of the tetrathiafulvalene-tetracyanoquinodimethane complex in early seventies [112, 113, 114, 115, 116] and recently they have regained popularity due

to their versatility in a wide range of fields such as organic opto-electronic [117], solar energy conversion [118, 119, 120, 121] and non-linear spectroscopy. [122, 123, 124] According to the Mulliken D-π-A complexes theory, [125, 126] a CT complex is constituted by the two independent subunits forming a non-covalent dimer with an acid-base Lewis character, thus a partial donation of electronic density stabilizes the dimer formation giving rise to mutual Coulomb interactions. When in solution, the complexation lead to a small charge transfer which strongly increases upon photoexcitation leading to a CT state ($D^{\rho+}/A^{\rho-}$) in which the electron density reorganization is overall markedly different from that in the ground state. The electronic spectra of these adducts show new absorption bands, absent in each monomer, that usually correspond to transitions from the donor-acceptor frontier orbitals, for example, the first CT state involves the electron density redistribution from the HOMO to the LUMO, respectively. Regarding non-covalent molecular systems, such CT bands are typically observed in well-planar aromatic molecules and high electron affinity acceptors in which their interplanar distance and relative orientations are of particular interest and play a key role in the CT event modulation. Upon photoexcitation the sudden electronic density reorganization induces relevant forces and structural reorganizations which cause vibrational frequency shifts, allowing to probe the ultrafast nuclear reorganization in the so called Franck-Condon region, until the system rapidly decays into the electronic ground state. Two CT systems studied in the following work are shown in the following figure 1.4.

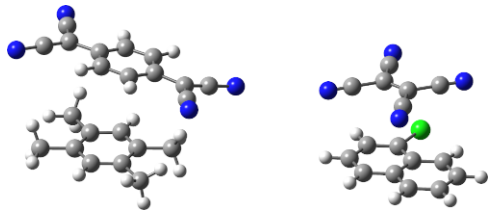

Figure 1.4. Ball and stick graphical representation of Tetracyanoquinodimethane: π :Tetramethylbenzene (TCNQ:TMB) (left) and Ethenetetracarbonitrile: π :1-chloronaphthalene (TCNE:1ClN) CT complexes. Carbons are reported in grey, hydrogens in white, nitrogens in blue and light green for chlorine.

The advent of ultrafast pulse laser (fs pulses) and LEDs technologies has meant a remarkable enhancement of the time and frequency resolution of modern mono- and multi-dimensional spectroscopic techniques [89, 127, 128,

129] paving the way to the investigation of fast transient dynamic photophysical and photochemical processes in real time. Despite of this, a detailed interpretation of such non equilibrium phenomena at the molecular level can be only provided by *ab-initio* simulations. The required theory has to simultaneously deal with an accurate description of the weak dispersion forces between the subunits, non equilibrium processes, and the inherently challenging excited states hypersurfaces topology. CT systems require also a very good description of both non covalent interactions and spatially delocalized excitations (i.e., valence-Rydberg, doubly excited, $\pi\pi^*$). Both phenomena need an accurate description of electronic correlation by employing multiconfigurational methods. On the other hand, these methods remain impractical for medium-large sized molecular systems since they scale with the fourth or higher power of the number of basis employed.[130, 131, 132, 133, 134] Density Functional Theory (DFT), due to its relative lower computational cost compared with ab-initio post Hartree-Fock methods and competitive accuracy, is today the most widely used electronic structure method that can come in the aid for the study of problems ranging from biological macromolecules in complex environments to molecular crystals in materials science. A well-known DFT shortcomings of common exchange-correlation (XC) functionals is the inability to describe long-range asymptotic Coulomb electronic and dispersion interactions (e.g., van der Waals forces) accurately because they are just functionals of local electron density or its gradient. In this framework, the performances of pure, hybrid and double hybrid XC-functionals have been systematically reported in dealing with interaction energies or optical properties prediction. [135, 136, 137, 138, 139] These interactions can play a fundamental role in determining the PES shape and therefore the correct physical and chemical interpretation of the phenomenon under study and then should not be neglected. [140, 141, 142, 143] It is clear that an accurate description of weak interactions within computationally less demanding methods would be ideal especially for the study of large systems. Numerous approaches have been developed to attempt to include dispersion forces in methods based on density functional theory. One approach relies on developing core potentials to account for London dispersion forces. [144] The parameterization of exchange-correlation functionals by exploiting high-quality benchmark databases, in which weak interactions play a predominant role, has led to the development of the family of functionals known as Minnesota functionals [145, 146, 147, 148] which have proven successful for modeling

weakly bound complexes. Although these functional ones have been extensively tested and used in quantum chemical calculations they are not free from doubts about their accuracy. [149, 150, 151] Empirical dispersion corrections provide a reliable way of including dispersive interactions without affecting DFT computational cost. The main idea is based on the addition of empirically computed damped dispersive interactions to the usual self consistent Kohn-Sham energy. A damping function [152, 153] is accounted to avoid double-counting of correlation effects and to determine the range of the correction. This approach has led over the years to the development of the so-called DFT-D methods of which Grimme [154, 155, 156, 157] is among the most active in the field. The current implementation, named DFT-D3, is applicable to all elements of the periodic table, both for organic and metallic systems, and is typically 10% accurate compared to CCSD(T) accuracy. Cutoff radii and dispersion coefficient are computed ab-initio by DFT and TDDFT methods along with extended basis set and this makes this method less empirical than the previous ones. [158, 159] The methods briefly illustrated here are now widely used in the modeling of systems interacting in ground state and have proved satisfactory compared with the highly demanding wavefunction-based method. Dispersion corrected time-dependent density functional calculations on weakly bound complexes, is proven to be satisfactory for excitations to different valence states, compared to EOM-CCSD and MP2 calculations, but still inaccurate for excitations to Rydberg states and electronically excited states for which the electron density is strongly different from the ground state and would require a state specific dispersion correction. [160]

1.4 Singlet fission in diarylindenotetracene semiconductor

Currently one of the greatest challenges facing humanity is the exhausting search for new energy sources that are clean, easy to use and that can avoid the worst consequences of climate change induced by the combustion of fossil fuels. Among the various forms of alternative energy to those based on petroleum products, the organic electronic [161, 162, 163, 164] has an exceptional potential in converting energy from sunlight to usable energy forms, that can lead to renewable, cheap and clean energy sources which are starting to become part of our everyday life. Solar energy is considered to be the best

alternative to fossil fuels but around 1% is now used to meet the incredible demand for energy. This demand for cheap, sustainable and small electronic devices has driven chemists, from both academia and industry communities to advance the field of the organic electronics through the rational synthetic approach to get new electron-donor (p-type) and electron-acceptor (n-type) molecules to be used in organic solar cells. n-type materials based on perylene diimides [165, 166, 167, 168, 169] and fullerene C_{60} [170, 171, 172, 173] dominated the organic photovoltaic scene due to the high electronic affinity and the excellent solid state properties of this latter (as the isotropic charge transport). But a number of disadvantages of fullerene compounds (low stability, high cost and poor absorption in the visible range) have led to the development of novel electron acceptors based on *non-fullerene* moieties, to overcome such limitations, that show greater potential in the framework of organic photovoltaic materials (OPVs) [174, 175, 176, 177, 178, 179, 180, 181]. Organic electronics showed several advantages and competitiveness compared to inorganic materials including the potential for the production of flexible, lightweight, cheaper, and easily tunable devices. The inclusion of functional groups on a specific molecular core, can modulate the frontier molecular orbitals gap (HOMO and LUMO), modify the crystalline structure, enhance the light absorption, the solubility or the photostability and the efficiency of charge transport from one unit to another. To improve the efficiency of these organic materials it is necessary to have a detailed knowledge about the mechanisms of energy exchange and charge transport (excitons). In this context computational modeling, combined with time resolved vibrational spectroscopy techniques, can provide the necessary tools in prediction, understanding of structure-function relationships and in the discovery of new suitable materials going beyond a static view of nuclear and electronic properties as the dynamics aspect of photoinduced processes are of paramount importance. Taking into account the dimensions of the systems under study, sometimes very large, modeling requires a very tailored approach which is the result of the compromise between computational cost and accuracy. A whole family of compounds based on indene scaffold derivatized in different ways has recently been proposed as a promising replacement for fullerene compounds for photovoltaic materials. [182, 183] Among these new classes of n-type compounds, in the present work we intend to study a recently synthetized diarylindenotetracene-based compound asymmetrically functionalized with two methoxy groups, from an experimental and computational point of view. The structure of the diarylindenotetracene under study is shown in

1.5, consisting of a tetracene backbone fused with a methoxy derivatized indene in the center and two phenyl rings on the opposite side, of which one of them bears a second methoxy group. We will use an acronym to refer to this system much more easily: *DimethoxyASI*.

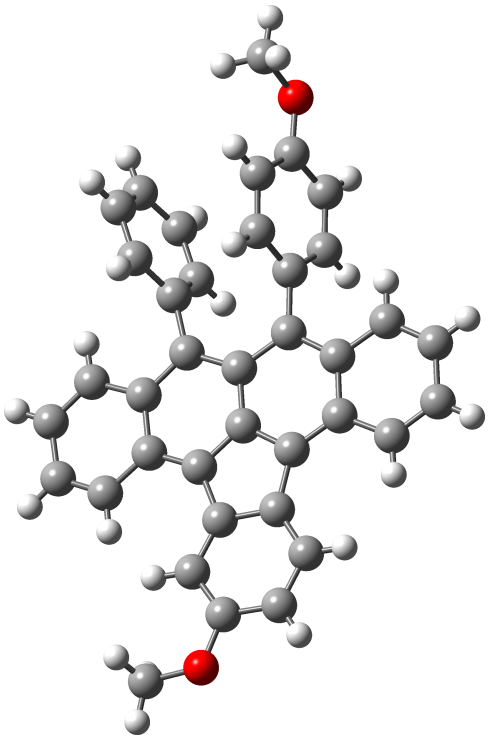

Figure 1.5. Monomeric structure of the electron-deficient asymmetrically substituted diarylindenotetracene, IUPAC name: *2-Methoxy-9-(4-methoxyphenil)-10-phenylindeno[1,2,3-fg]-tetracene*, Carbons are reported in grey, hydrogens in white, red is for oxygens.

The ability of these compounds to act as electron acceptor arises from the anti-aromatic 4n π-system conjugated five membered ring. The uptake of 2 electrons turns this molecules aromatic and then good electron acceptors. The characterization and synthesis can be found in the reference literature. [182, 183]

The efficiency of a photovoltaic device is limited at only 32% by the theoretical Shockley-Queisser limit [184] due to unabsorbed photons or to the energy excess conversion to heat. Several strategies have been proposed so far to overcome such limitations and to design systems that can be useful in new generation solar cells. This limit can be increased up to 45% [185] through

a process known as Singlet Fission (SF) [186, 187] that is a photophysical process which takes place in specific molecular chromophores in which the excited singlet state S_1 of a chromophore shares its excitation energy to a neighbouring ground-state chromophore converting both into two triplet excited states (T_1-T_1). SF does not occur in single molecules, the presence of multichromophoric system is required. The process occurs when the energy of the S_1 state is greater or equal to twice the energy of the triplet state T_1 ($E(S_1) \geq 2E(T_1)$). SF is a spin-allowed process reverse to T_1-T_1 annihilation and is a special case of internal conversion (IC). It can be very fast in crystals, on a sub-picosecond timescale competing with vibrational relaxation. Net one photon excitation creates two hole-electron pairs. This high efficiency in singlet - triplet conversion and the long lifetime of the generated triplets makes SF particularly appealing for practical applications as high-performance devices, solar cells with improved efficiency. [188, 189, 190] The overall process of the SF can be simplified as in eq. 1.7:

$$\begin{aligned} a)&S_{0A} + S_{0B} \rightarrow S_{1A} + S_{0B} \\ b)&S_{1A} + S_{0B} \rightarrow CT(S_A^{\pm} S_B^{\mp}) \leftrightarrow {}^1(T_1 T_1)_{AB} \rightleftharpoons {}^1(T_1 \cdots T_1)_{AB} \rightleftharpoons T_{1A} + T_{1B} \\ c)&S_{1A} + S_{0B} \leftrightarrow {}^1(T_1 T_1)_{AB} \rightleftharpoons {}^1(T_1 \cdots T_1)_{AB} \rightleftharpoons T_{1A} + T_{1B} \end{aligned} \quad (1.7)$$

Considering a multichromophoric system, the incident photon excites the A molecule from the ground S_{0A} to the first excited state S_{1A}, eq 1.7a), the B molecule is still in its ground state S_{0B}. At this stage two different mechanism have been proposed, a *two step mechanism*, eq 1.7b), in which the conversion of the singlet to the triplet state is mediated by a stable CT intermediate ($S_A^{\pm}$ $S_B^{\mp}$) with strong cationic and anionic character to then continue towards the formation ${}^1(T_1\ T_1)_{AB}$ and separation of the two triplet states T_{1A}+T_{1B}; or the *direct mechanism* eq 1.7c), in which the excited S_{1A} chromophore shares its energy with the S_{0B} chromophore and then proceed towards the last stages, triplet formation and separation ${}^1(T_1\ T_1)_{AB}$, ${}^1(T_1 \cdots T_1)_{AB}$, T_{1A}+T_{1B}. The process is distinct from intersystem crossing (ISC), in that singlet fission does not involve a spin flip, but is mediated by two triplets coupled into an overall singlet. Typical for acenes and polyacenes, the exciton multiplication may improve photovoltaic cells efficiency since the back electron transfer to the ground state would be spin-forbidden. The long lifetime of the triplets would help the exciton diffusion on the one hand, but there may be a greater

chance of quenching. Since its first discovery in anthracene crystals [191], further classes of compounds are known today [192] which can absorb high energy photons and give more than 100% of quantum yield (QY)[190], it is theoretically possible to achieve a QY of 200%. We intend to investigate the structural dynamics associated with the SF event from an experimental and theoretical-computational point of view, and possibly study the migration phenomena of the excitons to give further useful insights in understanding the photophysics at stake and provide ideas into the rational design of performing devices.

This experimental part of this project was carried out in the Chemistry Department of the University of Minnesota in the laboratories of prof. R.R. Frontiera.

2 Excited State Time-Resolved Vibrational Dynamics: the Challenge of Charge Transfer Complexes

2.1 Background and motivation

In this Chapter we will discuss our results about a non-covalent CT dimer which consists of an electron donor, tetramethylbenzene (TMB), and an electron acceptor, 7,7,8,8-tetracyanoquinodimethane (TCNQ). TCNQ is a versatile electron acceptor [193] due to high electron affinity (between 2.88 and 3.38 eV) and its ability to form charge transfer complexes [114, 194, 96] with a wide variety of electron donors, from organic and inorganic [195] molecules to metal surfaces. [196] Since its synthesis to date has attracted great interest and has assumed a very important role also in the solid state chemistry research area. [197, 198, 199] Recently, Femtosecond Stimulated Raman Spectroscopy (FSRS) [89, 93] has been used to examine the vibrational dynamics of the photoinduced charge transfer within this non-covalent electron donor/acceptor (EDA) complex. Once in solution they combine in a π-stacked dimer and following the photoexcitation an electron transfer (ET) from the TMB to the TCNQ molecule is supposed to happen. In dichloromethane solution the TMB:TCNQ complex has a broad, featureless CT absorption band in the 600 - 450 nm region (2.07 - 2.76 eV). The CT transition is supposed to be characterized by an intermolecular excitation from the HOMO of the TMB to the LUMO of the TCNQ. Considering also that the Raman spectra of the chemically generated anion $TCNQ^{-}$ and the excited state complex (formed almost immediately following photoexcitation)

are similar, frequencies are within 10 cm^{-1}, led to think that the excited state of the CT complex can be accurately described as a transient bi-radical specie, i.e. $TCNQ^{\dot{-}}$:$TMB^{\dot{+}}$.

Additional studies have employed Transient Absorption (TA) [200] providing that the back ET process takes place in about 10 ps. From FSRS studies it has been assumed that the excited-state dynamics involves a Conical Intersection (CI) [201], that promotes the relaxation on the ground state (GS) potential energy surface (PES), which is facilitate by an anharmonic coupling between an high and a low frequency vibrational modes, mainly located on the TCNQ's acceptor monomer. Thanks to the unique capabilities of advanced spectroscopic technique such as ultra-fast Raman techniques, in terms of time and frequency resolutions, Transient Absorption and Resonance Raman (RR) measurements it was observed that a low frequency vibrational mode (peaked at 323 cm^{-1}) is strongly excited upon photoexcitation and it persists for about 5 ps. This latter should also be involved in the intensity and frequency modulation of a higher frequency mode at 1271 cm $^{-1}$. This large anharmonic coupling should lead to a degeneration of the excited and ground state PES at a certain point, generating then a CI which allows the system to reach the thermal equilibrium in a non-radiative way. We recall here that at least two vibrational modes are required to form a CI and describe the branching space of the nonadiabatic transition: a totally symmetric mode which modulate the energy gap between two PES, known as *tuning mode*, and a nontotally symmetric mode, the *coupling mode*, which operates on symmetry between them. [93] In 2.1 the CT complex under study is pictorially presented along with the constituent monomers. We performed an extensive

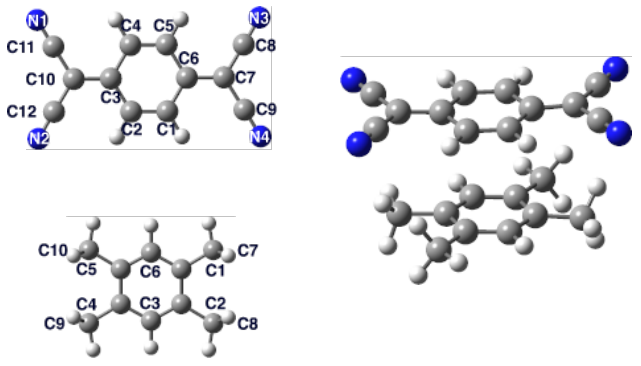

Figure 2.1. Subunits forming the CT complex (left) with bond label scheme, and side view of the TCNQ:π:TMB complex. Carbons are reported in grey, hydrogens in white, blue is for nitrogens.

characterization of the model system in both ground and first singlet excited states (S_0 and S_1), within methods rooted in the Density Functional Theory (DFT) [202, 203, 204] and its Time Dependent version for excited states (TD-DFT), from a static and dynamical point of view. We mainly focused on photophysical and photoreactive events in excited molecular system using a recently developed theoretical-computational method for time resolved vibrational analysis. [77, 78, 79, 80, 81] Furthermore, the structural analysis performed by molecular dynamics simulations in both electronic states, has highlighted how nuclei have adapted to the new electron density of excited state and how they relax starting from the Franck-Condon region. Our aim was to unravel the vibrational dynamics of key vibrational modes focusing on the excited state vibrational relaxations of two vibrational modes moving towards quantification of the anharmonic coupling especially between high and low frequencies modes. The hypothesis we intend to validate is that this coupling drives and modulates the charge recombination in the ground state. Considering the non-adiabatic nature of the photophysics involved for this CT molecular system, in what follows we will discuss only the relaxation phenomena for which the Born-Oppenheimer approximation still holds.

2.2 Methodology

2.2.1 Computational details

In this section we illustrate the computational details related to static and molecular dynamics calculations.

Optimization calculations without any constraints, energies, harmonic, anharmonic frequencies and IR intensities were performed on S_0 and S_1 in gas phase starting from at least two molecular guesses. The ground state electronic structures were obtained by solving the Kohn-Sham equation using the range-separated version of the hybrid Becke three-parameter Lee-Yang-Parr (B3LYP) density functional [202, 203, 204] and with the Coulomb-attenuating approach (CAM-B3LYP) [205] for excited states in its time dependent approach. The long-range corrected Coulomb attenuated hybrid functionals class [205, 206, 207, 208, 209] have been shown to predict charge transfer and Rydberg-like excitations energies/bands more accurately due to their high sensitivity to the treatment of exact exchange [210, 211, 212, 213, 214, 215, 216, 217, 218, 219, 220, 221, 222] with respect to the hybrid density

functionals (i.e. B3LYP, Perdew-Burke-Ernzerhof-0 [223, 224]). Weak interactions between monomers have been described correcting potentials with Grimme's dispersion (GD3 [225, 154, 226, 155, 156, 157]). Since there are no vibrational couplings with the vibrational modes of solvent we didn't account for solvation in our investigation, furthermore due to the low dielectric constant of DCM (ε=8.93) the effects on geometry, vertical excitation and so on are negligible. All *ab-initio* calculations have been performed by using GAUSSIAN suite program. [227] By exploiting the atom centered density matrix propagation formalism (ADMP, [49, 50, 51, 45, 52]) we collected a 10 ps-long ground state ab-initio molecular dynamics trajectory after 1 ps of equilibration and ran over potential calculated at B3LYP/6-31G(d,p)/GD3 theory level; a constant thermal energy (300 K) has been enforced by scaling nuclear velocities every 100 fs, with a time step of 0.2 fs. One of the energy minimum optimized geometries (the less stable one) have been chosen as starting point. We performed TDDFT single point calculations on several geometries randomly extracted from the GS sampling comparing performances of two different basis set (6-31G(d,p) and 6-31+G(d,p)) for checking the accuracy of the smaller basis set. The vertical excitation energy (VEE), oscillator strength and the largest molecular orbitals coefficients are presented, for thirteen geometries, in 2.1 and 2.2.

Comparing the values obtained with two different basis sets, it is possible to evaluate that the presence of diffuse functions induces only a slight redshift of the excitation energies with a maximum discrepancy calculated equal to 0.04 eV. Excited state AIMD simulations, according to the BOMD propagation scheme [228, 229], have been sampled at CAM-B3LYP/6-31G(d,p)/GD3 theory level for about 7,5 ps simulation time, with a time step of 0.7 fs starting from three coordinates and momenta sets chosen from GS-AIMD. The choice of the initial points, sketched in 2.2, was carried out considering the distance between the center of mass of the two monomers, the total ground and excited NBO (Natural Bond Orbital) charges [230, 231, 232, 233, 234, 235] and we have taken into account the values of the vertical transitions $S_1 \leftarrow S_0$ and $S_2 \leftarrow S_1$.

The molecular dynamics trajectories was then analysed in terms of a detailed structural analysis and to extract the *generalized-normal modes* for the equilibrium and far from equilibrium time-resolved vibrational analysis. Results from excited state molecular dynamics are presented as an average of three trajectories.

Time (fs)	**VEE (eV)**	***f***	**MOs coeff.**	**Electronic Transition**
607.2	2.029	0.0292	0.11218	**L** ← **H-2**
			0.69143	**L** ← **H**
1103.8	1.887	0.0205	0.70408	**L** ← **H**
1600	2.050	0.0117	0.70469	**L** ← **H**
1820.2	1.839	0.0084	0.70515	**L** ← **H**
2189.4	1.754	0.0076	0.70334	**L** ← **H**
2667.6	1.726	0.0387	0.70004	**L** ← **H**
4489	1.894	0.0550	0.69878	**L** ← **H**
6181.6	2.345	0.0919	-0.11117	**L** ← **H-1**
			0.69375	**L** ← **H**
6862.4	2.045	0.0504	-0.15704	**L** ← **H-1**
			0.68700	**L** ← **H**
7614	2.091	0.0188	0.70152	**L** ← **H**
8391.6	2.319	0.1130	-0.15693	**L** ← **H-1**
			0.68652	**L** ← **H**
9464	2.078	0.0987	-0.13485	**L** ← **H-1**
			0.68820	**L** ← **H**
10000.2	2.162	0.1170	0.70088	**L** ← **H**

Table 2.1. $S_1 \leftarrow S_0$ TDDFT SP calculations performed on geometries extracted from GS-AIMD according to CAM-B3LYP/6-31G(d,p) theory level. Vertical Excitation Energy (in eV), the oscillator strength (f) and the largest MOs coefficient are reported.

Time (fs)	**VEE (eV)**	***f***	**MOs coeff.**	**Electronic Transition**
607.2	1.987	0.0271	-0.11589	**L** ← **H-2**
			0.69447	**L** ← **H**
1103.8	1.845	0.0188	0.70405	**L** ← **H**
1600	2.046	0.0121	0.70465	**L** ← **H**
1820.2	1.821	0.0088	0.70508	**L** ← **H**
2189.4	1.743	0.0079	0.70357	**L** ← **H**
2667.6	1.694	0.0391	0.70060	**L** ← **H**
4489	1.863	0.0544	0.69970	**L** ← **H**
6181.6	2.305	0.0935	0.69578	**L** ← **H**
6862.4	2.011	0.0503	-0.14264	**L** ← **H-1**
			0.68994	**L** ← **H**
7614	2.053	0.0189	0.70162	**L** ← **H**
8391.6	2.274	0.1121	-0.14709	**L** ← **H-1**
			0.68862	**L** ← **H**
9464	2.041	0.0959	0.11791	**L** ← **H-1**
			0.69073	**L** ← **H**
10000.2	2.125	0.1156	0.70117	**L** ← **H**

Table 2.2. $S_1 \leftarrow S_0$ TDDFT SP calculations performed on geometries extracted from GS-AIMD according to CAM-B3LYP/6-31+G(d,p) theory level. Vertical Excitation Energy (eV), the oscillator strength (f) and the largest MOs coefficient are reported.

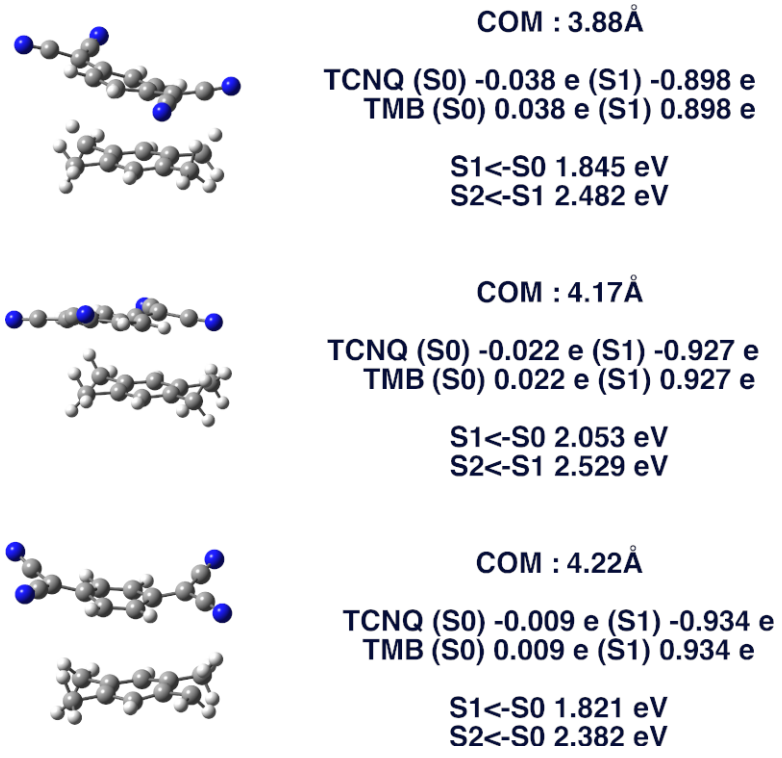

Figure 2.2. Initial geometries to run excited state BOMD simulations, extracted from ground state AIMD simulations for which the center of mass distances, TD-DFT vertical excitation energies and total ground and excited state NBO charges for each monomer are given according to CAM-B3LYP/6-31+G(d,p)/GD3 potential.

2.3 Results and discussion

2.3.1 Structural characterization by static and dynamical approaches

Molecular systems ruled by weak interactions can explore a large conformational space visiting numerous stationary points, overcoming low energy barriers or even barrierless ones. The PES of a non covalent molecular complex is then very complex and we expect to contain a large number of energy minima almost degenerate for which the definition of an equilibrium structure becomes completely meaningless. Locating and characterizing each structure can be a very long, if not impossible, work. Some efficient methods are now widely used for determining geometries and other properties which, in some way, widen the vision of true energy minimum by calculating energy gradients. Those that rely on classical or *ab-initio* molecular dynamics or random sampling (Monte Carlo) provide a wealth of information that can be pulled out by subtly analyzing the trajectories.

Our work began by looking for some minimum energy structures on the fundamental state PES, we limited our discussion to two most representative ones. Two minimum energy structures 2.3 have been obtained for the fundamental electronic state starting from different guesses in vacuum with negligible energy difference (ΔE= 1.03 Kcal/mol). The most stable TMB:TCNQ complex is a π-stacked structure in which the two rings are not exactly coplanar, named MS0$_A$. Other ground state minima and energy differences are reported in A.1 and A.2 in the Appendix A along with initial guess structures. The same considerations were reached when the implicit solvent (DCM) was taken into account, in that case the relative energy of the two monomers was equal to 0.99 Kcal/mol (data not shown).

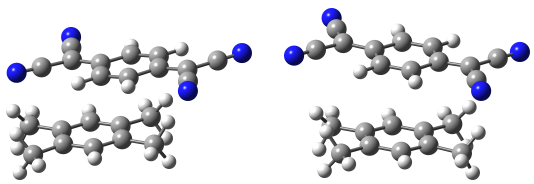

Figure 2.3. Ground state energy minima, from left to right, computed in gas phase at B3LYP/6-31+G(d,p)/GD3 named $MS0_{A,B}$, respectively.

Both isolated ground state minima have been further optimized in the first

singlet excited state (2.4). The energy difference is now quite low with respect the GS case and the $MS1_b$ turn out to be more stable (ΔE= 0.96 Kcal/mol). Moreover, for this latter, the acceptor monomer adopts a visible distorted boat shape, bended towards the TMB molecule.

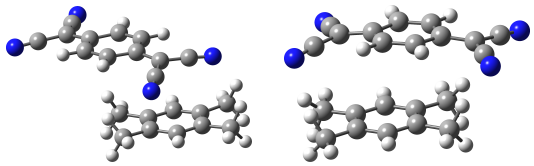

Figure 2.4. First singlet excited state energy minima, from left to right, computed in gas phase at CAM-B3LYP/6-31+G(d,p)/GD3 named $MS1_{a,b}$, respectively.

Following the photoexcitation, the electron density of the excited state is usually quite or strictly different from the ground state, whereby the equilibrium structure will tend to relax changing its geometry towards a bonding pattern compatible with the new electron density. We have observed this new arrangement of the nuclei by comparing the S_0 and S_1 equilibrium structures and reporting the difference of the bond lengths calculated in both electronic states for the two minima considered. In this way we can easily appreciated which direction they take following photoexcitation.

Considering the TCNQ acceptor monomer structural changes in both minima (2.5, top), the C=C's double bonds undergo to an elongation especially for those outside the ring (C3-C10 and C6-C7, > 0.025 Å , see 2.1 for labels) and even if to a lesser extent, those inside the ring, C1-C2 and C4-C5. On the contrary CC single bond shortens when in excited state, in particular the effect is more evident among the ring atoms, C2-C3, C3-C4, C5-C6 and C6-C1, with respect to the four CC single bond preceding the cyano groups. Finally, a negligible shortening of $\simeq$ -0.02 Å of the four cyan groups is observed in S_1. It can be summarized that the acceptor monomer passes from a typically *quinoid* structure to a *benzenoid-like* one. [198, 196] The TMB donor monomer (2.5, bottom), yielding electronic density due to excitation, undergoes mainly structural changes involving the bonds of the aromatic ring that stretch significantly, in particular C1-C2 and C4-C5 bonds (> 0.04 Å). The C-C single bonds with the methyl groups (C1-C7, C2-C8, C4-C9 and C5-C10) due to the electron-donor effect typical of the -R groups tend to approach the aromatic ring. When in excited state the six membered ring becomes less aromatic but *quinoidal* overall. Despite the high symmetry of

TCNQ and TMB molecules, the different height of the bars in 2.5 corresponding to the two minimum energy structures arises from the asymmetry of the molecular complex, from the relative orientation of the two monomers.

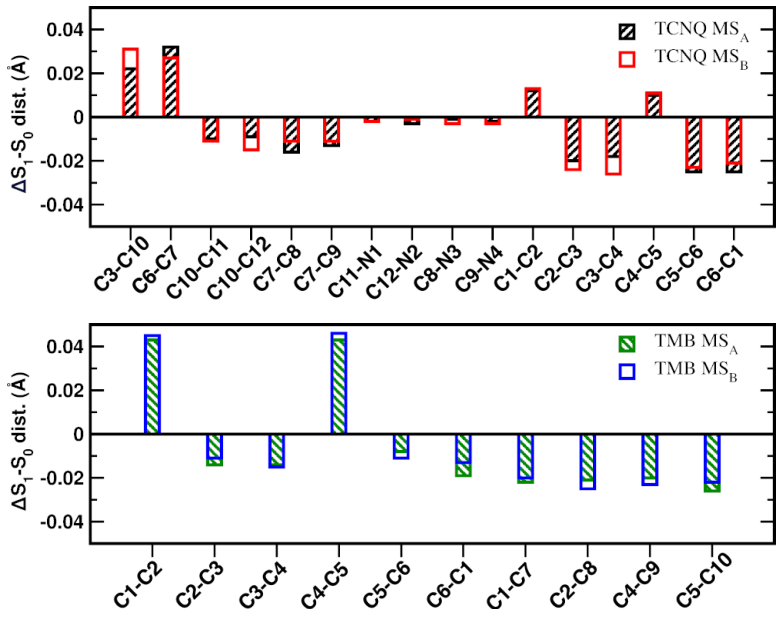

Figure 2.5. Bar chart presenting the difference of the bond lengths calculated for the S_0 and S_1 electronic states for both the minimum energy structures, reporting, at the top, the values of the TCNQ molecule and at the bottom those related to the TMB donor monomer, respectively.

We analyzed the nature of electronic transitions in terms of molecular orbitals compositions by performing time-dependent DFT calculations simulating the optical absorption spectrum of the TCNQ:TMB isolated CT complex. TDDFT calculation predicts that the $S_1 \leftarrow S_0$ transition is purely a HOMO-LUMO transition at 542.25 nm (2.29 eV, f=0.1843) for the most stable conformer ($MS0_A$) and 573.16 nm (2.16 eV, f=0.0473) for the second one, in agreement with the experimental UV-Vis spectrum recorded in DCM solution. Frontier molecular orbitals, HOMO and LUMO, reported in 2.6 are located on donor and acceptor monomer, respectively, so the first singlet excited state exhibits a strong *charge transfer* character. Although MOs isosurfaces are very informative, we performed a natural bond order population analysis to have quantitative insights on the electronic rearrangement of the TMB:TCNQ complex upon photo excitation. In the ground state we find a discrete charge separation for both molecular complexes: $\pm$ 0.128 e for $MS0_A$ and $\pm$ 0.095 e for $MS0_B$ (the minus sign it refers to the TCNQ molecule) that

rules the weak interactions between the two monomers and allows the formation of π-stacked dimers. In ES the charge distribution changes radically and we find, for both minima, a charge separation close to 1 e ($MS1_A$ $\pm$ 0.948 e and $MS1_B$ $\pm$ 0.949 e) suggesting the formation of a biradical species in which the TCNQ received and electron ($TCNQ^{\dot{-}}$) from the donor monomer ($TMB \rightarrow TMB^{+} + 1e^{-}$). These trends are in agreement with the experimental hypothesis. [93] The results shown here exemplify the main role of the photoexcitation on this non-covalent intermolecular CT dimer.

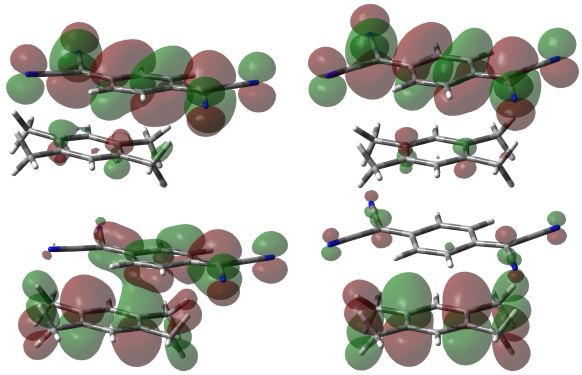

Figure 2.6. HOMO and LUMO molecular frontier orbitals (isovalue= 0.02) involved in the $S_1 \leftarrow S_0$, electronic transition computed in gas phase at CAM-B3LYP/6-31+G(d,p)/GD3 for the two minima $MS0_{A,B}$, from left to right respectively.

The vibrational analysis, in the harmonic approximation, was mainly focused towards the identification of the two normal modes: the in plane CCN bending and the CC rocking mode associated to the TCNQ monomer, which are supposed to be the driving force of the excited state reactivity due to the anharmonic coupling between them. The composition of normal modes computed in the ground and first singlet excited state is depicted in 2.7 for the $MS0_B$, as an example. The whole vibrational spectra of the TCNQ:TMB EDA complex computed in gas phase on the S_0 and S_1 electronic states are showed in A.3 in the Appendix A.

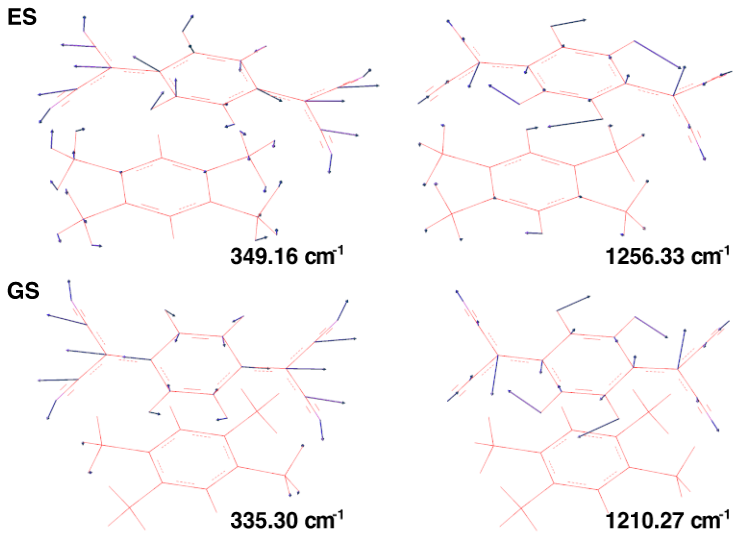

Figure 2.7. $MS0_B$ composition of vibrational modes of interest, calculated for the S_0 (bottom) and S_1 (top) electronic states. The in plane CCN bending mode (left) and the CC rocking mode both undergo a blue shift of frequency when in ES of about 15 and 45 cm^{-1}, respectively.

Now we provide a comprehensive and quantitative analysis of various structural parameters of the CT complex performed by ground and excited state AIMD trajectories taking into account bond lengths, bond angles and dihedrals. The normal distributions of selected bond lengths of the single TCNQ (2.8 2.9) and TMB (2.10) molecules have highlighted the greatest structural differences passing from the ground to the excited state PESs. The main structural changes found mostly concern the double bonds inside the acceptor ring (C1=C2, C4=C5) and similarly for C6=C7 and C3=C10 that undergo a considerable lengthening following the photoexcitation. In particular the ring's double bonds increase of 0.011 Å on average and 0.03 Å for those outside the ring which undergo the maximum elongation. Single CC bonds go in the opposite direction, this is particularly evident for the CC bonds of the ring that change more (0.02 Å) due to the new electronic distribution. The triple bond of the cyano groups is shortened in a negligible way (0.001 Å)

The effects due to the photon absorption are summarized here for the donor monomer. The double bonds of the ring adjacent to the methyl group undergo the maximum elongation (0.05 Åon average) while the methyl groups approach to the aromatic ring (0.025 Å) as the remaining CC bonds (0.02 Å). It can therefore be guessed that the electronic density is spread over the all double bonds of the acceptor, the entire molecules is stretched in the C7-C10 direction. The six-membered ring of the donor, on the contrary is now stretched along the C3-C6 axes.

The same considerations are reached through the study of the frontier molecular orbitals most involved in the electronic transition (reported in 2.6). Bond lengths, bond angles and dihedrals angles are tabulated and reported in A.2 and A.3 in the Appendix A.

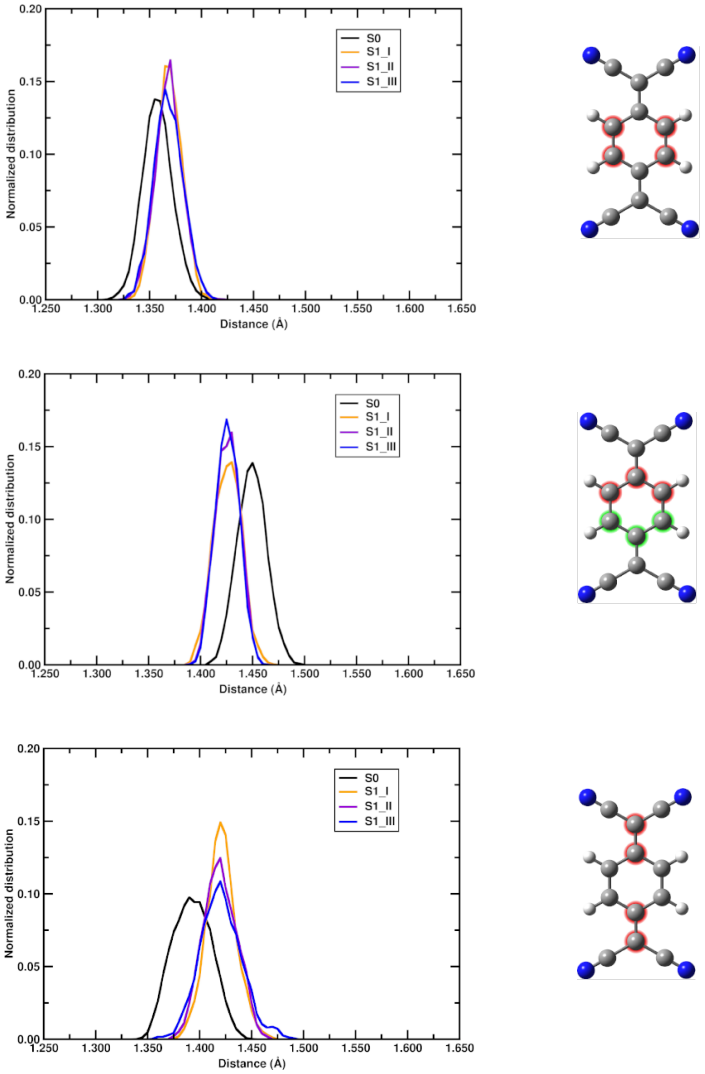

Figure 2.8. TCNQ acceptor monomer normal distributions of the average bond lengths, from ground (**S0**) and excited state (**S1 I**, **S1 II**, **S1 III**) trajectories, of C=C's ring double bonds (top), C-C's ring single bonds (center), C=C double bond outside the ring (bottom). Coloured labels are shown to the right of each distribution.

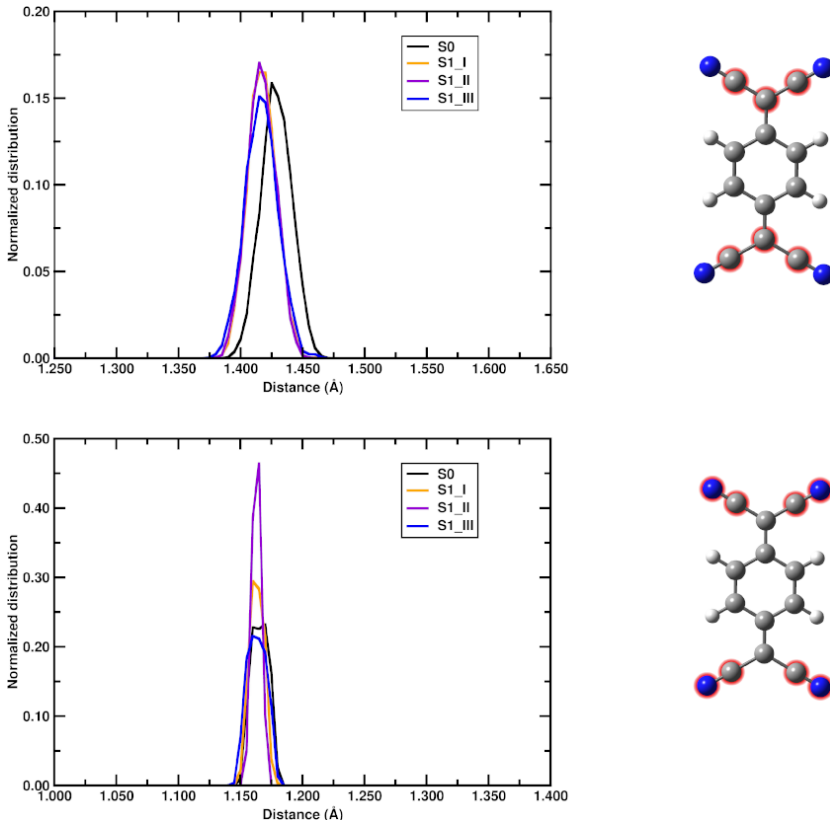

Figure 2.9. TCNQ acceptor monomer normal distributions of the average bond lengths, from ground (**S0**) and excited state (**S1 I**, **S1 II**, **S1 III**) trajectories, of C-C's single bonds outside the ring (top), C≡N triple bond of the cyano groups (bottom). Coloured labels are shown to the right of each distribution.

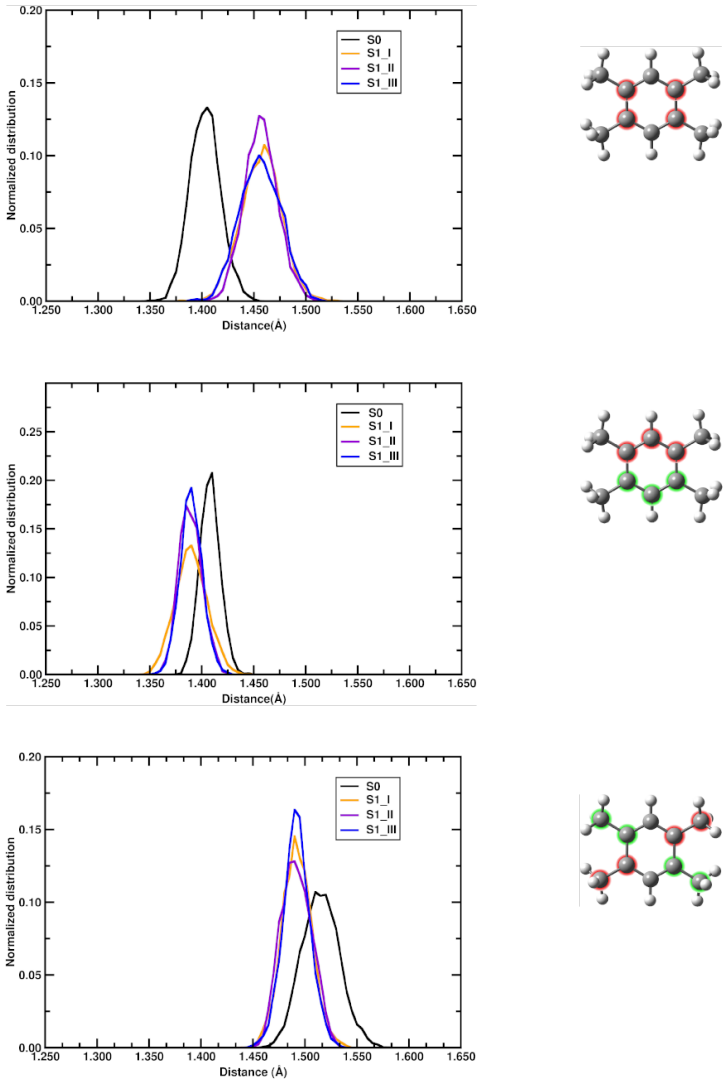

Figure 2.10. TMB donor monomer normal distributions of the average bond lengths, from ground (**S0**) and excited state (**S1 I**, **S1 II**, **S1 III**) trajectories, of C=C's ring double bonds (top), C-C's ring single bonds (center), C-CH_3 bond outside the ring (bottom). Coloured labels are shown to the right of each distribution.

2.3.2 Spectroscopic analysis from *ab-initio* molecular dynamics simulations

By a visual inspection of the equilibrium and excited state sampling, a π-π stacked arrangement is always observed for the two monomers as predicted from minimum energy search while other topologies such as T-shaped, parallel displaced and edge to face have never been founded. We computed the distance between the two centers of mass to verify that following photoexcitation, the occurred charge separation allowed the two monomers to come closer together then calculated for the ground state. This latter is discussed and shown in the A.4 in the Appendix A. In this section we discuss the vibrational analysis of two *generalized normal modes* of interest extracted from ground and the average excited state AIMD trajectories. The time-independent spectrum has been computed through the Fourier Transform of velocity-velocity autocorrelation functions for the ground state case, the equilibrium time-resolved vibrational analysis has been carried out computing the Wavelet Transform of the autocorrelation function. On the other hand, the excited state one has been computed starting from the average of the mode velocities projected along the directions of the ground state *generalized normal modes*. From the same signal the transient time-resolved vibrational spectrum was obtained through the continuous Wavelet Transform and plotted as a map for a better reading. The in plane CCN bending mode localized on the TCNQ acceptor (2.11, center), have been extracted from ground state AIMD trajectory taking into account only the coordinates and momenta of the acceptor monomer, thus obtaining a less crowded and more resolved spectrum. The time-independent vibrational spectrum is showed on top of 2.11, two features are present in the spectrum the main one is peaked at 334 cm^{-1} and is the frequency of interest, the less intense is at 380 cm^{-1} and can be ascribed to another TCNQ bending mode. The Wavelet spectrum shows a well resolved band centred below 500 cm^{-1} and exactly at 330 cm^{-1} in agreement with Hessian-based harmonic calculation, whose magnitude is exhausted starting from about 6,5 ps. In the same way we extracted the CC rocking mode which is depicted in 2.12, similar in composition to that obtained from the calculation of vibrational modes on the ground state minimum. The Fourier spectrum shows a signal peaked at an anharmonic frequency of 1287 cm^{-1}, the associated magnitude in the time-resolved power spectrum starting rise from 6,5 ps and persists for the rest of the sampled time. Available spectroscopic data in literature, at best of our knowledge, do not report about frequency values for

this specific system in the ground electronic state hence, a direct comparison between our time-resolved vibrational dynamics with experimental findings is not possible.

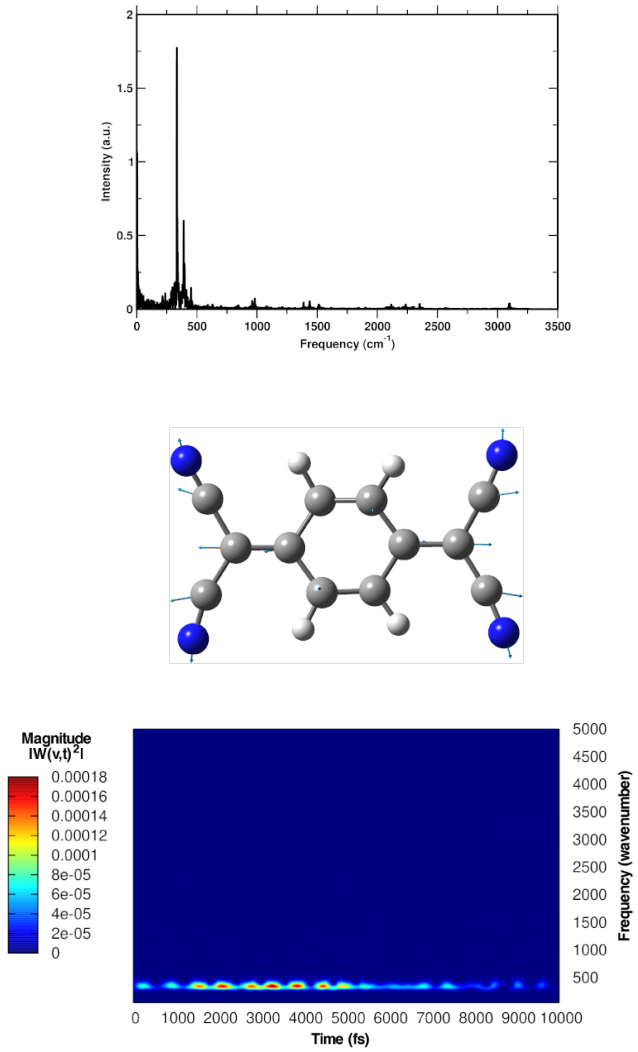

Figure 2.11. In plane CCN bending generalized normal-mode (center) localized on the TCNQ acceptor subunit along with the time-independent Fourier Transform spectrum (top) and time-resolved Wavelet spectrum (bottom) showed in perspective view.

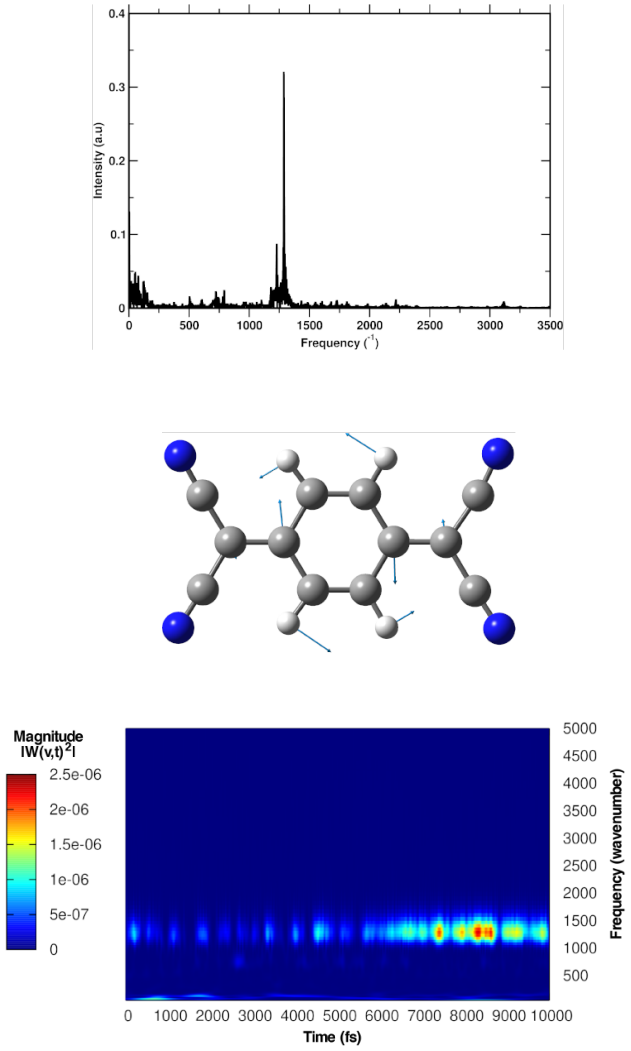

Figure 2.12. CC rocking generalized normal-mode (center) localized on the TCNQ acceptor subunit along with the time-independent Fourier Transform spectrum (top) and time-resolved Wavelet spectrum (bottom) showed in perspective view.

The photoinduced vibrational dynamics of the TCNQ:TMB CT complex has been investigated in the first singlet excited state in which the CT dimeric system can be considered biradical in nature. Inspecting the static vibrational spectrum reported at top in 2.13 several vibrational features are present namely due to the contribution of vibrational modes of the TMB donor monomer around 1000, 1500 and above 3000 cm^{-1}, in addition to the most important one peaked at 352 cm^{-1}. It is also observed that the vibrational mode in the center of 2.13 is recognizable although is inherently complex. The Wavelet spectrum in 2.13 shows that the band around 350 cm^{-1} is the main feature and that other signals in the FT spectrum do not contribute significantly. Another important observation regards the time evolution of the magnitude of the signal: in the FSRS experiments the TCNQ's CCN bending mode persists for $\simeq$ 5 ps upon the electronic excitation and our time-resolved vibrational spectrum, shows that the magnitude of the CCN mode actually decreases gradually up to 5 ps. This interesting trend in agreement with experimental counterparts, was always observed for all three sampled trajectories. The magnitude of the signal in question is plotted against time in A.5 and reported for clarity in the Appendix A.

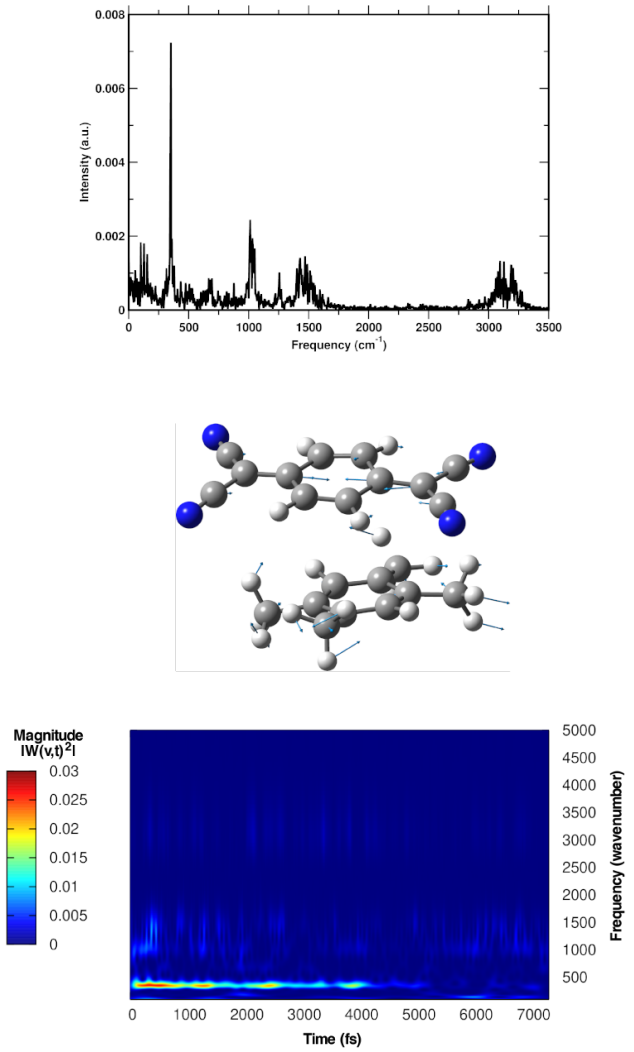

Figure 2.13. In plane CCN bending generalized normal-mode (center) extracted from the average of three excited state trajectories along with the time-independent Fourier Transform spectrum (top) and time-resolved Wavelet spectrum (bottom) showed in perspective view.

The vibrational mode corresponding to the TCNQ ring CC rocking motion has been reported in the center of 2.14, the FT spectrum shows several features in addition to the frequency of the vibrational mode centred at 1260 cm^{-1}. One of the advantages of the Wavelet transform is that it returns the temporal evolution of a vibrational band and therefore allows subsequent analysis aimed at, e.g., the quantification of the anharmonic couplings. Inspecting the time-resolved Wavelet spectrum 2.14, the vibrational dynamics showed a clear oscillatory behaviour. From an experimental point of view the 1271 cm^{-1} rocking mode is the only visible fundamental that displays significant couplings to the 323 and 355 cm^{-1} modes and have detectable coupling to the 105 or 151 cm^{-1} modes, both of which involve deformations of the CCN angle. Interestingly, Fourier transforming the frequency's magnitude fluctuations of the CC rocking mode, a clear feature at 360 cm^{-1}, attributable to the coupling with TCNQ's CCN bending (2.15), can be observed along with several other frequencies of collective modes and ring deformations ($<$ 300 cm^{-1}).

We provide here 2.16 further analysis that allowed us to identify the *tuning* vibrational mode for the CI that governs and controls charge recombination internal conversion. The vibrational analysis has been carried out on the time evolution of the S_0-S_1 energy gap, as average of the three sampled trajectories. From the Fourier Transform spectrum a main peak at 351 cm^{-1} can be recognized; in the time resolved vibrational spectrum a signal is present again within the first 5 ps. This result confirms that actually the CCN bending acts as the *tuning* mode modulating the energy gap between the involved electronic states.

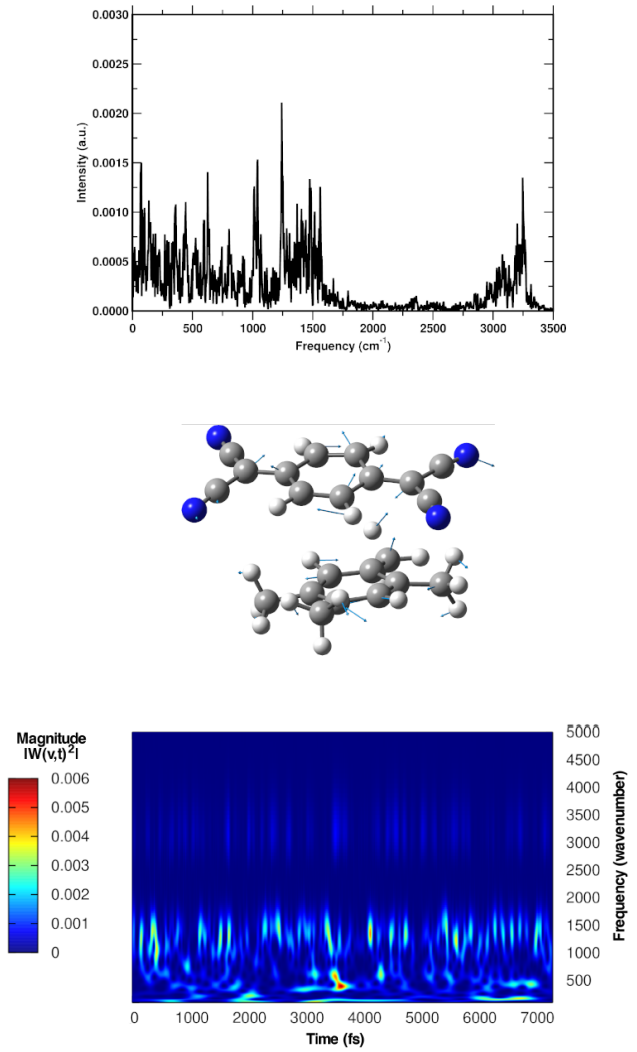

Figure 2.14. CC rocking generalized normal-mode (center) extracted from the average of three excited state trajectories along with the time-independent Fourier Transform spectrum (top) and time-resolved Wavelet spectrum (bottom) showed in perspective view.

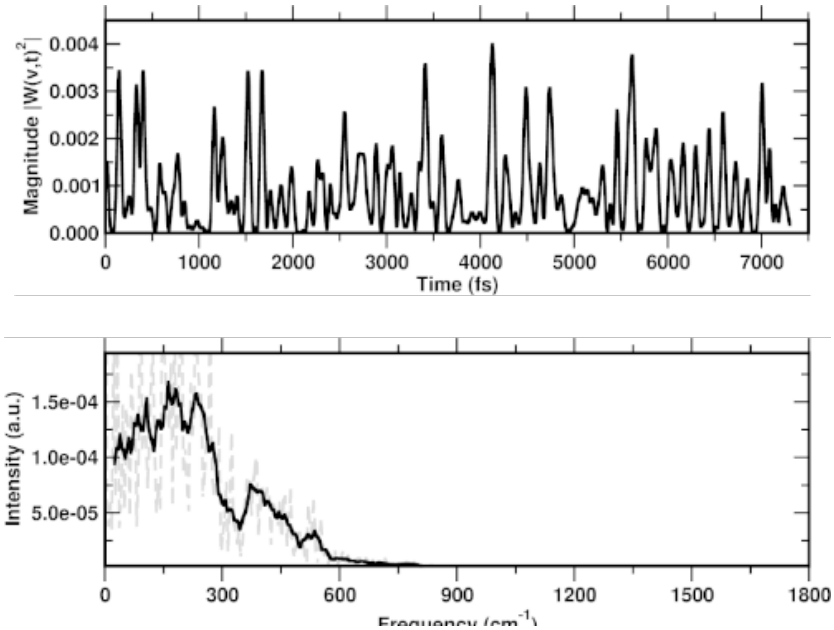

Figure 2.15. Excited state time-resolved CC frequency's magnitude fluctuations (top) Fourier Transformed (bottom) to quantify the anharmonic coupling with other vibrational modes. The feature close to 350 cm^{-1} can be related to the CCN bending mode.

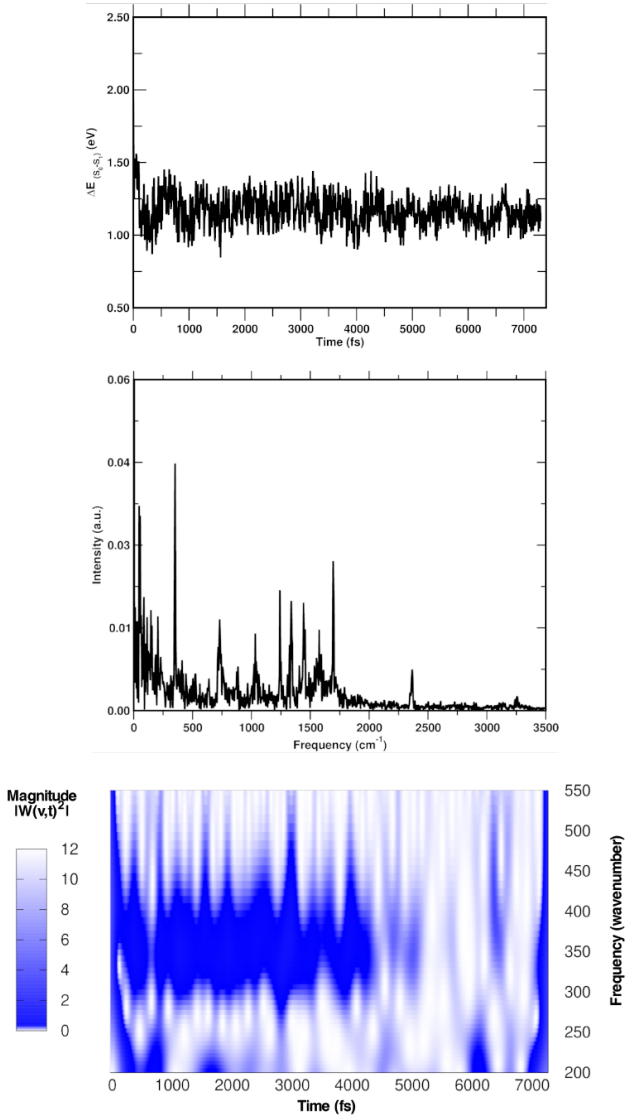

Figure 2.16. Time evolution of the S_0-S_1 electronic energy separation (eV, top) as an average of three excited state trajectories and the time-independent vibrational spectrum that shows a main peak at 351 cm^{-1} (center). The time-resolved vibrational spectrum highlights a signal around 350 cm^{-1} which lasts for 5 ps.

2.4 Conclusion remarks

In this chapter, we showed results made to understand the vibrational relaxation and the mechanism of the photoinduced charge transfer that occurs in a non-covalent molecular complex through a robust computational protocol that combines the adiabatic *ab-initio* molecular dynamics in ground and excited state and a time-resolved vibrational analysis based on the Wavelet Transform. We carried out a preliminary investigation through a static quantum-mechanical approach in the DFT and TDDFT framework, in order to verify the accuracy of the methods employed and the modeling strategy. Two vibrational modes play a fundamental role in the photophysics of the TCNQ:TMB molecular complex, both have also been characterized in time and frequency domains through the study of *generalized normal modes* extracted from molecular dynamics simulations. Our results are in agreement with the experimental evidence in a satisfactory way, we were able to quantify the anharmonic coupling between the CC rocking mode and the CCN bending mode located on the TCNQ acceptor monomer confirming the experimental hypothesis. Furthermore, the excited state vibrational dynamics is also in agreement with FSRS data. Taking into account the challenging nature of the system under study, this computational strategy proves to be reliable and accurate even for non covalent systems such as the one just discussed.

3 Probing Relaxation Mechanisms of Photoinduced Intermolecular Charge Transfer Dimer

3.1 Background and motivation

The purpose of this work is to examine in detail a non-covalent intermolecular charge transfer complex in which the 1-Chloronaphtalene (1ClN) acts as electron donor species towards the well known Tetracyanoethylene (TCNE) [236, 237, 238] molecule (acceptor). Both ground state properties and mostly important, the low-lying CT electronic transition have been investigated here given also the the availability of experimental spectroscopic data. [239, 94] The main interactions ruling this complex (reported in 3.1), responsible of the observed π-π stacked arrangement [240] when in polar aprotic solvents, i.e. in dichloromethane (DCM) solution, are of a non covalent nature. The pursued approach relies on a theoretical protocol based on AIMD simulations in ground and first singlet excited state at DFT level along with the multiresolution wavelet protocol to get time-resolved vibrational spectra. This work is intended to provide useful insights on the internal vibrational energy flow following the electronic excitation, translating the anharmonic nuclear motion in terms of relaxation processes unveiling the anharmonic vibrational couplings in the time domain.

This work is organized as follows: in the next section (3.2) we discuss about

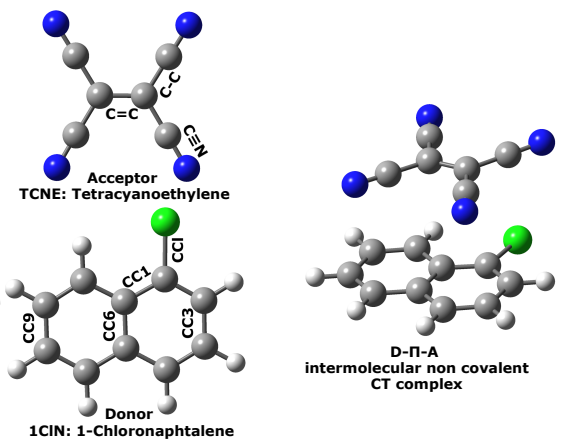

Figure 3.1. Subunits forming the CT complex (left) with bond label scheme, and side view of the TCNE:π:1ClN complex. Carbons are reported in gray, hydrogens in white, blue is for nitrogens and green for chlorine atom.

our methods and related computational details for static and *ab-initio* molecular dynamics calculations in both ground and first singlet excited state, as well as the transient vibrational analysis based on the Wavelet Transform. In section 3.3 results about full quantum mechanical and dynamical approaches will be discussed and insights about the activation of relaxation pathways by excited state nuclear dynamics are given too. In the last section (3.4) Conclusions and perspectives are given.

3.2 Methodology

3.2.1 Computational details

All presented calculations were performed by using the GAUSSIAN electronic structure software package [227]. Ground state energies, gradients and higher order energy derivatives were obtained using the hybrid Becke, 3-parameter, Lee-Yang-Parr (B3LYP) density functional [202, 203, 204] with a 6-31+G(d,p) basis set. Weak dispersion forces between the two subunits were accounted correcting potentials with Grimme's dispersion (GD3) [225, 154, 226, 155, 156, 157]. Time-Dependent Density Functional Theory (TD-DFT), within the linear response formalism, using the range-separated version of the hybrid B3LYP density functional with the Coulomb-attenuating approach (CAM-B3LYP)[205] also this time using 6-31+G(d,p) and GD3

was instead employed to describe accurately excited states. The long-range corrected Coulomb attenuated hybrid functionals class [205, 206, 207, 208, 209] have been shown to predict charge transfer and Rydberg-like excitations energies more accurately with respect to the hybrid density functionals [210, 211, 212, 213, 214, 215, 216, 217, 218] (i.e. B3LYP, Perdew-Burke-Ernzerhof-0 [223, 224]). Additionally, we accounted for Dichloromethane (ε = 8.93, DCM) solvation effects via Polarizable Continuum Model in its Conductor like version (C-PCM) [241, 242, 243, 244, 245, 246] to mimic the solvent environment around the CT complex. The amount of charge transferred between the two TCNE and 1ClN fragments in both ground and first singlet excited states was quantified by employing the Natural Bond Orbitals (NBO) charge partitioning scheme, [230, 231, 232, 233, 234, 235] along with calculating the value of the density based CT index (*Dct*), introduced by Ciofini and coworkers. [247, 248, 249, 250, 251] Ground state coordination geometries of TCNE doublet radical anion in the presence of a counter ion (Na^+ or K^+, see 3.16) were also investigated through structural optimization and vibrational frequency evaluations using C-PCM to account for implicit solvation effect of Acetonitrile solvent (ε = 38.8, ACN). To better analyze relaxation pathways upon excitation, first order Cartesian nonadiabatic coupling matrix elements (NACs) were computed analytically in the framework of linear response TD-DFT [252, 253] on several selected structures displaced along selected *generalized normal modes*, **Q**, extracted from ground state *ab-initio* molecular dynamics trajectory. The computational affordability of this approach relies on the fact that the explicit calculation of the excited state wave function is avoided since all information can be recovered in the evolution of the reference (i.e., ground) electronic state:

$$d^a_{kj} = \left\langle \Phi_k | \frac{\partial}{\partial Q_a} \Phi_j \right\rangle \tag{3.1}$$

in which Q_a is a Cartesian nuclear coordinate expressed in atomic units ($Bohr^{-1}$), $|\Phi_k\rangle$ and $|\Phi_j\rangle$ are the initial and final electronic states, respectively, taken into account. From the 3.1, the derivative couplings d^a_{kj} will be large near surfaces crossing regions and will tend to infinity when approaching to a conical intersection. In what follows we will report and discuss the Frobenius norm of the NACs matrix and the TD-DFT energy scan for each generalized normal mode, **Q**, individuated.

3.2.2 Ground and excited state *ab-initio* molecular dynamics sampling

Ground state *ab-initio* molecular dynamics (AIMD) simulation, according to Atom-centered Density Matrix Propagation (ADMP) formalism [49, 50, 51, 45, 52] was collected for 10 ps, after 1 ps of equilibration, using a time step of 0.2 fs. B3LYP/6-31G(d,p)/DCM(C-PCM)/GD3 theory level was used and a temperature corresponding to 300K was enforced by scaling regularly nuclear velocities. Three distinct excited state AIMD simulations (Born-Oppenheimer Molecular Dynamics, BOMD [228, 229]) were sampled for about 6 ps each, with a time step of 0.7 fs according to TD-CAM-B3LYP/6-31G(d,p)/DCM(C-PCM)/GD3 potential. Harmonic frequencies calculations performed on the same excited state minimum energy structure ensure that the presence or the absence of diffuse *s* and *p* functions in the basis sets leads to practically overlapping results and that the maximum deviation was about 10 cm^{-1} on a high frequency mode as shown in 3.2.

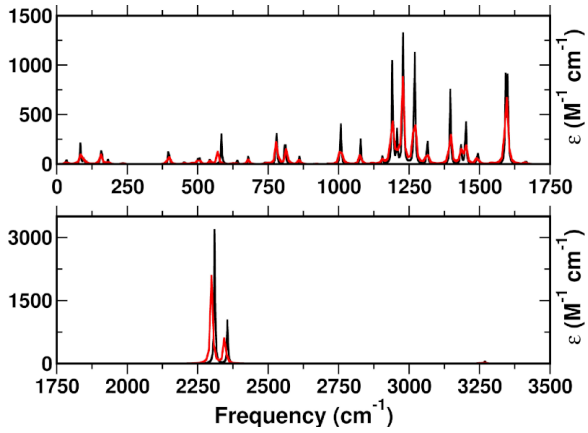

Figure 3.2. Harmonic vibrational frequencies (in wavenumbers, cm^{-1}) computed for the optimized geometry ($MinS1_a$) at TD-CAM-B3LYP/6-31+G(d,p) (black trace) compared with TD-CAM-B3LYP/6-31G(d,p) (red trace) theory level in implicit DCM solvent. The maximum difference observed is $\approx 10cm^{-1}$ in the stretching region of the CN groups, 2300-2350 cm^{-1}

Initial geometries sketched in 3.3 were chosen from the ground state trajectory checking several properties such as: the accuracy in the prediction of S_0-S_1 excitation with respect to the experimental value, the amount of CT (by inspecting the NBO charges), and the distances of the center of mass of the two units.

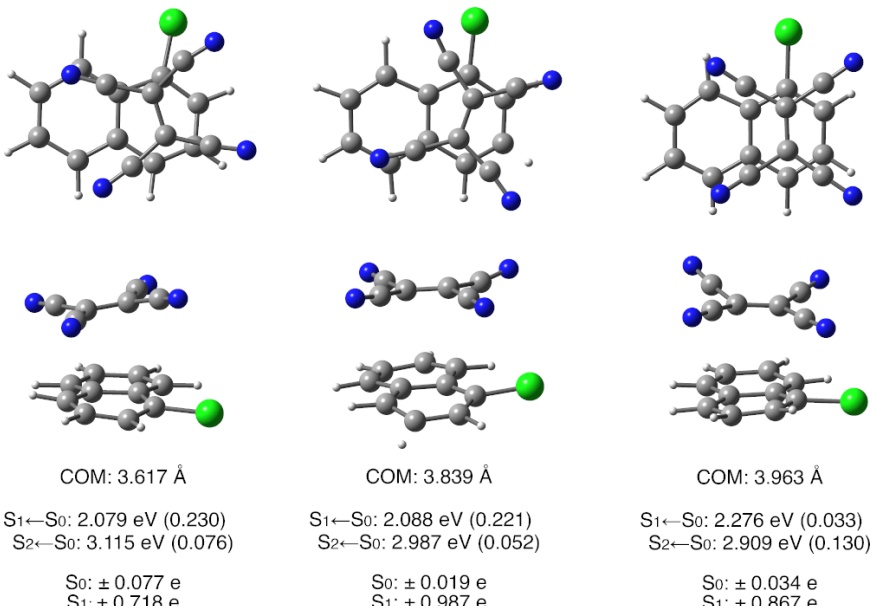

Figure 3.3. Initial geometries to run excited state BOMD simulations, extracted from ground state AIMD simulations for which the center of mass distances, TD-DFT vertical excitation energies (absolute errors are given in parenthesis) and total ground and excited state NBO charges are given.

The experimental UV-Vis absorption spectrum of the TCNE:1ClN complex in DCM solution [94] shows two charge transfer absorption bands corresponding to transitions from the ground to the first two singlets excited states. The less energetic transition, with maxima at 2.31 eV, it is observed at 0.73 eV far from the most energetic one covering a broad spectral range overall (from 1.82 to 3.44 eV). Vertical excitation energies computed for 20 CT structures regularly extracted (each 500 fs) from GS AIMD ensure that the conformations sampled during the dynamics always led to CT character transitions with energetic separation between S_1 and S_2 electronic states of $\approx$0.880 eV, on average. Furthermore, upon the excitation to first singlet excited state a clear increase of net NBO charges occurs for all the frames investigated, ranging from $\pm$ 0.73 e to $\pm$ 1.10 e for 1ClN and TCNE subunits, respectively. The results are shown below in the respective 3.4 and 3.5. In this way, both a consistent charge transfer of the low lying transition and a significant energy separation between the two excited states were checked on average along ground state dynamics.

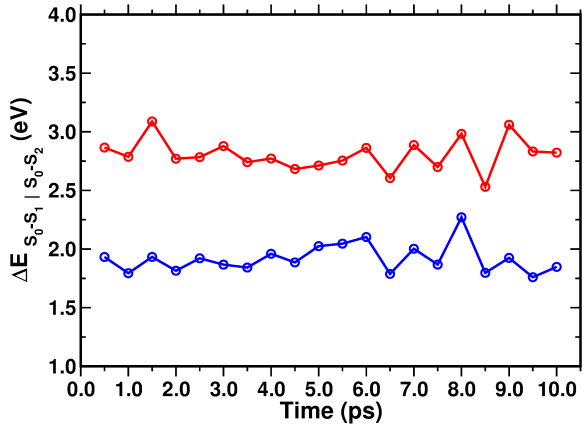

Figure 3.4. Vertical Excitation Energies $S_1 \leftarrow S_0$ (solid line and blue circles) and $S_2 \leftarrow S_0$ (solid line and red circles) computed on conformers extracted each 500 fs from ground state *AIMD*.

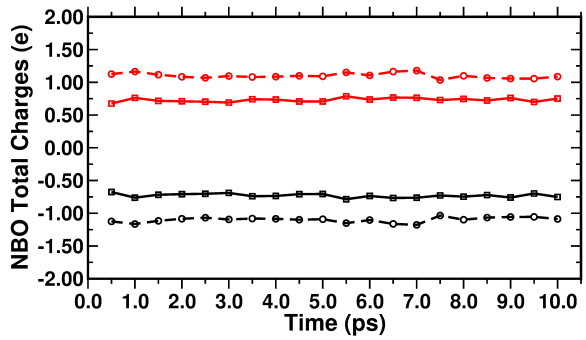

Figure 3.5. Net charges (e) according to Natural Bond Orbitals analysis performed on 20 conformers on ground (solid) and first singlet excited state (dashed) for the TCNE (black traces) and 1ClN (red traces) monomers.

3.3 Results and discussion

3.3.1 TCNE:1ClN CT complex first principles spectroscopic and structural characterization

Given the non covalent nature of the complex, different ground and excited state conformations for the non covalent complex, are expected. In this work different cofacial starting configurations of the TCNE:1ClN CT complex, were chosen to model relative orientations assumed by the two units, leading to at least three different stable energy minima (referred as $MinS0_{a-c}$, reported in 3.6). They were fully planar retaining the π-π stacked arrangement: for the $MinS0_a$, in 3.6, the two monomers were in a distorted orthogonal conformation in which the TCNE were above the two bridgehead carbons (CC6, please refer for the following discussion to labels in 3.1) at a greater distance from 1ClN ($\approx$ 0.25 Å) compared to those observed for the other two conformers. Since they differ from each other for less than 1 Kcal/mol, it is reasonable to state that they can be all reasonably representative of the equilibrium relative orientation at room temperature. They are very similar from a structural point of view indeed, therefore in the following discussion the main structural parameters for only one (named $MinS0_a$) of the obtained ground state conformations are discussed in the first column of 3.2

In the ground state, computed C=C distances were, on average, 0.03 Å and 0.04 Å longer than the corresponding crystallographic value in neutral TCNE and with respect to neutral TCNE-donor complexes, respectively. [254, 255] The low polarity of DCM solvent and the non covalent dispersive interaction forces with 1ClN did not significantly affect the acceptor monomer structure in the ground state, indeed for the TCNE monomer the C=C bond length and its bond order, computed at the same theory level in implicit DCM solvent, were found to be 1.371 Å and 1.750, respectively. On the other hand, for the 1-chloronaphtalene monomer the two structural parameters considered (C-Cl and C-C1 distances) were, on average, strictly similar to the values found for the three energy minima complexes in the same electronic state, precisely 1.767 and 1.437 Å.

Computed vertical excitation energies relative to the previously mentioned ground state minima are reported in 3.1 for the first two excited electronic

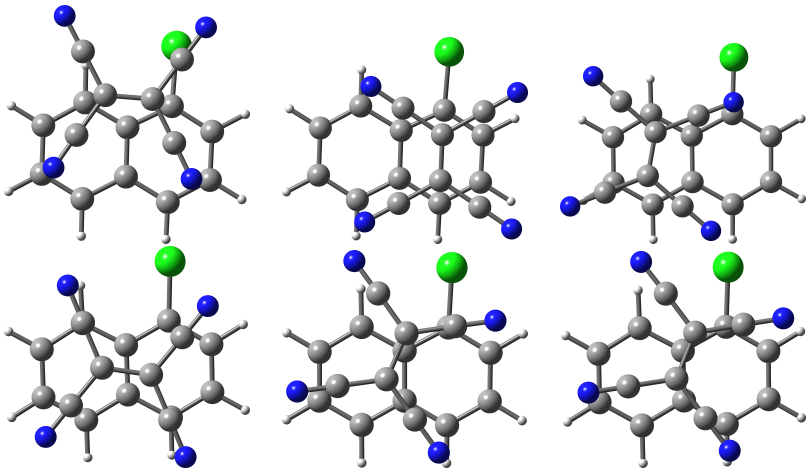

Figure 3.6. Ground (up) and first singlet excited state (bottom) energy minima, from left to right, computed in DCM solvent named $MinS0_{a,b,c}$ and $MinS1_{a,b,c}$, respectively.

	Exp. Abs.	$MinS0_a$	$MinS0_b$	$MinS0_c$
HOMO-1-LUMO	408 nm	431.30 nm	420.19 nm	420.46 nm
	3.04 eV	2.88 eV (0.16 eV)	2.95 eV (0.09 eV)	2.95 eV (0.09 eV)
HOMO-LUMO	530 nm	581.29 nm	564.85 nm	567.67 nm
	2.31 eV	2.13 eV (0.21 eV)	2.20 eV (0.14 eV)	2.18 eV (0.16 eV)

Table 3.1. Vertical excitation energy (in nm and eV) for the three TCNE:1ClN CT complexes in DCM solvent, absolute errors are given in parenthesis along with experimental values observed in the same conditions.

states ($S_1 \leftarrow S_0$, $S_2 \leftarrow S_0$), responsible for the experimentally observed two distinct charge-transfer bands with absorption maxima at 2.31 and 3.04 eV, respectively in the UV-Vis electronic spectrum of TCNE:1ClN CT complex [94]. The accuracy in the electronic transition energy prediction for the first excited state transition is within 0.21 eV, in accordance with well performances of CAM-B3LYP in describing charge transfer like transitions.[214, 215, 220]

The $S_1 \leftarrow S_0$ and $S_2 \leftarrow S_0$ transitions among electronic states are mainly described by HOMO to LUMO and HOMO-1 to LUMO excitations, which MOs isosurfaces are reported in 3.7, respectively. The charge transfer nature of this transitions is clearly observable from 3.7: the electron density is transferred from the condensed rings of substitute naphtalene to the TCNE molecule when in excited state. Both HOMO and HOMO-1 are completely localized on the 1-chloronaphtalene donor molecule, while LUMO is entirely spatially confined on the TCNE acceptor unit. Considering the antibonding

character of the LUMO orbital, an elongation of the double bond C=C and a concomitant lowering of the bond order is expected in the excited electronic state. Investigating the LUMO contour plot, the electron-withdrawing effects of the four electronegative cyano groups placed around the ethylene moiety contribute to enhance the charge transfer process attracting electronic density to themself.

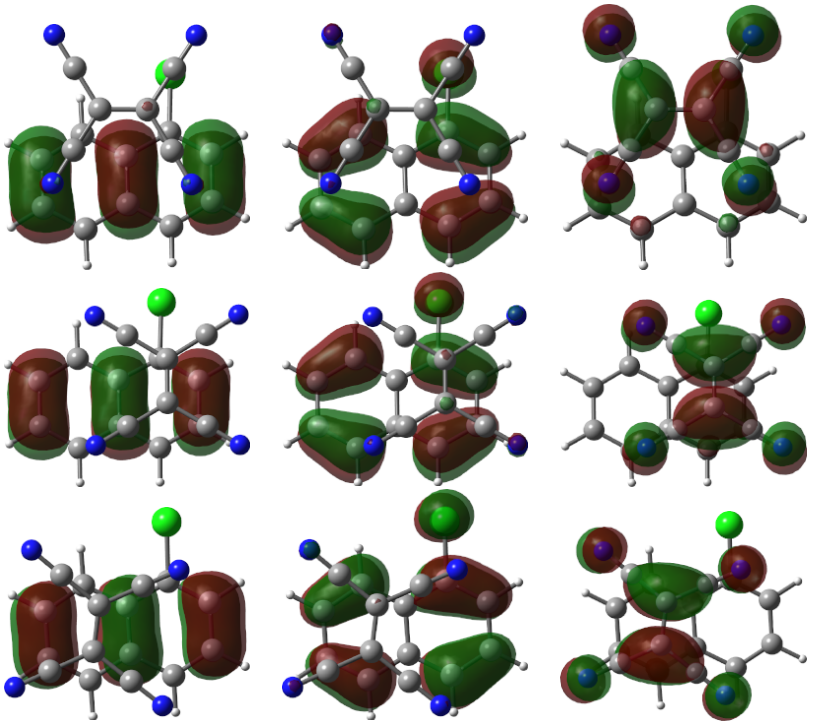

Figure 3.7. From left to right, HOMO-1, HOMO and LUMO frontier orbitals contour plots (isovalue 0.03) computed for $MinS0_{a,b,c}$ geometries in DCM solvent.

The three ground state energy minima conformers have been optimized again on the S_1 potential energy surface and energy minima have been isolated. Regarding the excited state S_1 minima, the relative position of the two subunits was, for two minima ($MinS1_{b,c}$, 3.6), very similar in the spatial arrangement and in terms of relative energy content. In the $MinS1_a$ complex (see 3.6 and 3.2, second column) the TCNE and 1ClN monomers were superimposed on each other in their centers, perpendicularly. The central C=C bond length (and related bond order) are important probes with respect to the charge transfer

	$MinS0_a$	$MinS0_b$	$MinS0_c$
Ground State (S_0)			
Relative Energy (Kcal/mol)	0.94	//	0.43
C=C $_{(TCNE)}$ (Å)	1.377	1.378	1.376
C=C Bond Order	1.75	1.75	1.75
C-C1 $_{(1ClN)}$ (Å)	1.426	1.428	1.425
C-Cl $_{(1ClN)}$ (Å)	1.762	1.759	1.762
Center Of Mass $_{(TCNE:1ClN)}$ (Å)	3.801	3.534	3.576
NBO total charge $_{(TCNE)}$ (e)	-0.066	-0.083	-0.073
NBO total charge $_{(1ClN)}$ (e)	0.066	0.083	0.073
	$MinS1_a$	$MinS1_b$	$MinS1_c$
Excited State (S_1)			
Relative Energy (Kcal/mol)	0.05	0.01	//
C=C $_{(TCNE)}$ (Å)	1.430	1.430	1.429
C=C Bond Order	1.52	1.53	1.52
C-C1 $_{(1ClN)}$ (Å)	1.420	1.421	1.421
C-Cl $_{(1ClN)}$ (Å)	1.710	1.710	1.710
Center Of Mass $_{(TCNE:1ClN)}$ (Å)	3.344	3.469	3.469
NBO total charge $_{(TCNE)}$ (e)	-0.854	-0.840	-0.870
NBO total charge $_{(1ClN)}$ (e)	0.854	0.840	0.870
Dct $_{(TCNE:1ClN)}$ (Å)	2.489	2.506	2.580

Table 3.2. Diagnostical structural parameters (Å), relative energy (Kcal/mol), NBO total charges (e) and dCT index (Å) calculated in implicit DCM solvent for three CT complexes computed for ground ($MinS0_{a-c}$) and first excited state ($MinS1_{a-c}$) at B3LYP/6-31+G(d,p)/DCM(C-PCM)/GD3 and CAM-B3LYP/6-31+G(d,p)/DCM(C-PCM)/GD3 theory levels, respectively.

extent toward the TCNE monomer. Moreover following the excitation, the average distances between the two monomers' center of mass (COM) decreased significantly, -0.2 Å, with respect to the one measured between the two subunits on the ground electronic state (3.427 Å and 3.637 Å, respectively), due to the photoinduced charge reorganization, confirming the hypothesis of a biradical species formation upon photoexcitation. According to the partial NBO charges analysis (3.2), the greater extent of charge separation due to the photoexcitation event, increased the attractive electrostatic interaction of TCNE and 1ClN molecules.

In the ground electronic state, harmonic and anharmonic frequency calculations were straightforwardly performed for all the conformers from Hessian matrix diagonalization and second-order perturbation theory, respectively, in

	S_0			S_1	**Others**
	Harmonic	Anharmonic	Δ	Harmonic	
out-of-plane bending	161.65	165.21	-3.56	159.14	168[a], 165[b]
sym. in plane CCN bending	540.82	530.09	10.73	550.77	542[b]
C=C stretching	1551.41	1520.66	30.75	1486.85	1570, 1565[c], 1551[d], 1421[e]

Table 3.3. Harmonic and anharmonic frequencies in wavenumbers (cm^{-1}) calculated in ground state ($MinS0_a$), harmonic frequencies computed in first excited state ($MinS1_a$) for the CT complexes in implicit DCM solution in comparison with experimental values found in literature. [a] TCNE:HMB resonance Raman excitation in DCM, Ref.[256] [b] TCNE:HMB resonance Raman excitation in CCl_4, Ref.[257] [c] Ground state neutral and complexed TCNE Ref.[258], [d] TCNE:HMB resonance Raman excitation in CCl_4 Ref.[259], [e] TCNE radical ion, Ref.[260]

order to recognise the frequency range of interest, the vibrational modes composition and, actually, to have a direct and accurate comparison of the results obtained from the static analysis with respect to the vibrational modes extracted from *ab-initio* molecular dynamics simulations. For all stationary points no imaginary frequency were identified (for example, see for vibrational modes of $MinS0_a$ and $MinS1_a$ geometries). In 3.3 we report a resume of harmonic and anharmonic frequencies computed in ground state, the harmonic frequencies calculated for the first singlet excited state along with other theoretical and experimental counterparts.

The low frequency mode investigated, the out-of-plane bending (represented in 3.8, **a**, **a'**), seems to be unaffected by photoexcitation, since frequency variations, and even the composition of the mode, in both S_0 and S_1 electronic states are almost identical. The symmetric bending involving the four cyano groups (represented in 3.8, **b**, **b'**) undergoes a very small (≈ 10 cm^{-1}) blue shift in its frequency when in excited state and the donor molecule no longer participates in the mode composition (becoming completely localized on the TCNE unit). The C=C stretching (represented in 3.8, **c**, **c'**), shows a redshift in its resonance frequency of several wavenumbers after the photoexcitation and, as in the previous case, is then completely localized only on the acceptor monomer.

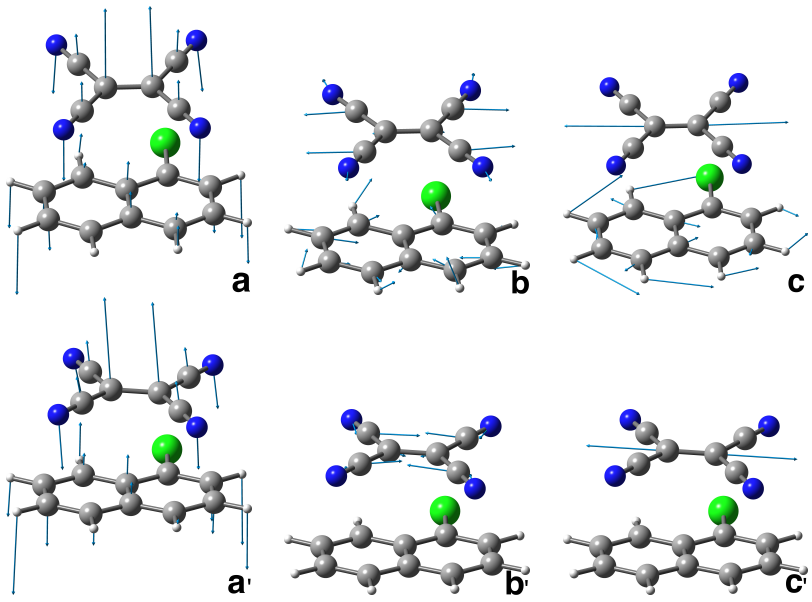

Figure 3.8. Vibrational modes of TCNE:1ClN CT complexes computed in ground (unprimed) and first excited state (primed). **a**,**a'** out of plane bending mode, **b**,**b'** symmetric in plane CCN bending, **c**,**c'** central C=C stretching

	Monomer		Dimer		AIMD$_{<10ps>}$ S_0	AIMD$_{<6ps>}$ S_1
	S_0	S_1	S_0	S_1		
			Tetracyanoethylene			
C=C	1.371	1.484	1.377	1.430	1.374 ($\pm$ 0.01)	1.433 ($\pm$ 0.02)
C-C	1.431	1.396	1.428	1.408	1.432 ($\pm$ 0.02)	1.413 ($\pm$ 0.02)
C$\equiv$N	1.162	1.168	1.162	1.163	1.163 ($\pm$ 0.01)	1.164 ($\pm$ 0.01)
			1-Chloronaphtalene			
C-Cl	1.768	1.729	1.762	1.701	1.774 ($\pm$ 0.04)	1.717 ($\pm$ 0.03)
C-C1	1.427	1.415	1.426	1.420	1.430 ($\pm$ 0.03)	1.424 ($\pm$ 0.02)
C-C3	1.416	1.365	1.412	1.381	1.417 ($\pm$ 0.02)	1.384 ($\pm$ 0.02)
C-C6	1.439	1.446	1.438	1.428	1.441 ($\pm$ 0.02)	1.430 ($\pm$ 0.02)
C-C9	1.413	1.369	1.413	1.388	1.419 ($\pm$ 0.03)	1.390 ($\pm$ 0.02)

Table 3.4. Structural parameters computed for monomeric and dimeric (mean values) species in ground and first singlet excited state minima compared with corresponding averaged values, standard deviations are given in parenthesis, extracted from S_0 and S_1 *AIMD* of TCNE:1ClN CT complex. Labels are referred to 3.1 and bond lengths are reported in Angstrom (Å).

3.3.2 TCNE:1ClN CT complex AIMD

During the 10 ps of B3LYP/6-31G(d,p)/DCM(C-PCM)/GD3 S_0 trajectory the CT complex retain the π-π stacked conformation in which the two monomers always interact with the same initial molecular side, although TCNE slides back and forth between the two aromatic rings of 1-chloronaphtalene. Despite of this, along the ground state simulation the two monomers assume large mutual displacements around an average value of the center of mass distance of 3.765 Å $\pm$ 0.2. On the other hand, in the excited state trajectories the two units tend to be closer (-0.092 Å) due to the increased partial charge on the two subunits which enhanced the coulombic attraction between them. The photoinduced CT leads to structural reorganization involving both subunits which can be summarized as follows: concerning the 1ClN donor monomer the C-Cl distance undergoes to a shortening (-0.057 Å) when in excited state and an alternation of the C-C bonds lengths also occurs in accordance to the HOMO-1 and LUMO spacial extents, depicted in 3.7. For the TCNE acceptor the central C=C bond is stretched out (about 0.062 Å), with a concomitant and symmetric stiffening (-0.019 Å) of the four (=C-)C-C($\equiv$N) distances. On the contrary, the bond lengths of the four cyan groups actually do not change when passing from ground to the excited electronic state.

The presented vibrational analysis is mainly focused on three significant vibrational modes, localized on the TCNE acceptor subunit, since their time evolution has been recently characterized with high time and frequency resolution by Femtosecond Stimulated Raman Spectroscopy (FSRS) by Mathies

and co-workers. [94] In details, these modes (reported in 3.8) are the central C=C stretching, the out-of-plane bending in which the cyano C≡N groups approaches toward the 1ClN and the symmetric in-plane deformation of the four CCN angles. The C=C stretching mode, being fully spacially localized, is strictly related to the C-C distance and its bond order which are both highly sensitive to the electron density rearrangement upon excitation, (i.e. charge transfer and coulombic interactions). In 3.9, 3.11 and 3.13 the three vibrational modes of interest extracted from AIMD simulations, reporting both their Fourier time-independent and time-resolved Wavelet associated spectra, are shown simultaneously for both ground and excited states. The spectrum in 3.9 presents a main contribution centered in the S_0 at 160 cm^{-1} with no significant changes upon excitation (157 cm^{-1}) showing a perfect agreement with the experimental value (153 cm^{-1}) [94]. This mode can be described in both electronic states as an out-of-plane bending involving both units moving synchronously towards each other in the same direction. During the S_0 trajectory, it emerges that this mode highly couples with another collective low frequency motion of the two monomers approaching closer to each other ($\sim$ 90 cm^{-1}). Several other small contributions to this mode seem to be present on average along the trajectory by inspecting the FT analysis such as the C-H stretchings of 1ClN ($\sim$2220 cm^{1}), the C-C stretching of the TCNE ($\sim$1300 cm^{-1}), the 1ClN C-H groups in plane bendings ($\sim$1130 cm^{-1}), and the symmetric NCNs scissoring of the TCNE unit (116 cm^{-1}). On the other hand, their magnitudes in the WT spectrum are $\sim$ 10% of the main features peaks, thus appearing to be less relevant. These low frequency coupled motions can be very important in modulating the charge recombination event in the excited state dynamics since their ability of narrowing the intermolecular distance, thus promoting a better overlap of the frontier orbitals 3.7. Upon excitation, the main vibrational feature of TCNE out-of-plane bending is still coupled with other low frequency motions (54 and 62 cm^{-1}, reported in 3.10), representing also this time collective motions promoting the rigid approaching of the two molecular planes to one another. Interestingly these vibrational modes, leading to charge recombination and therefore non-radiative decay, arise not immediately but after few initial ps from excitation. This is in accordance with the relative long experimentally observed life time of about 6 ps of the excited state [94].

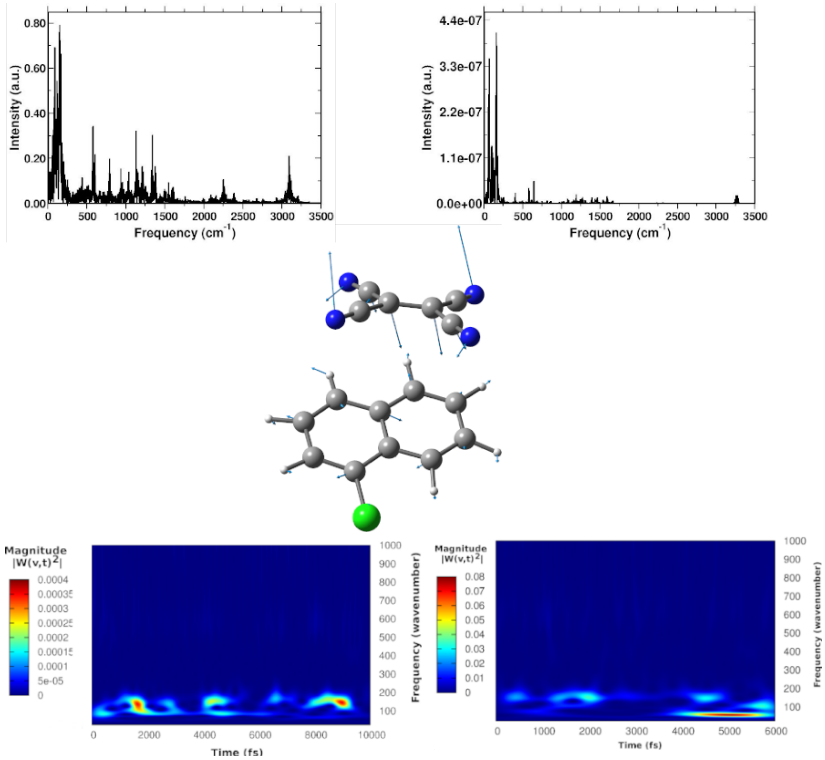

Figure 3.9. Time-independent spectra (top), normal-like mode composition (center) and Wavelet spectra (bottom) of the out of plane bending extracted from ground (left) and excited state (right) trajectory.

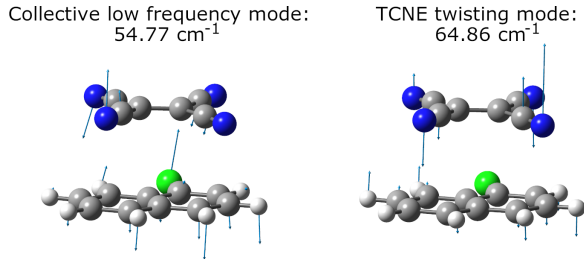

Figure 3.10. Low frequencies vibrational normal mode displacements (from $MinS1_a$ complex) observed in the excited state time-resolved Wavelet spectrum of the out of plane bending mode in 3.9, bottom right.

In 3.11, the time-resolved vibrational analysis in both electronic states of the vibrational mode involving the in phase symmetric CCN bending of the four groups on the TCNE molecule is discussed next. In the ground state it is observed a main peak at 538 cm^{-1}, in accordance with corresponding frequency value computed on ground state minima. As the previous mode, this feature shows strong couplings with other low frequency vibrations: the in phase bending of the two NC-C-CN angles (117 cm^{-1}) and the in plane bending around the central C-C moiety of the 1ClN molecule (222 cm^{-1}). On the other hand, a constant underlining coupling with a higher frequency mode (1173 cm^{-1}), representing the four (C=)C-C(N) stretchings localized on the acceptor monomer, is also observed. Upon excitation this second analyzed mode is present at slightly blue-shifted value with respect to the ground state (545 cm^{-1}, -7 cm^{-1}) and also this time is in a nice agreement with FSRS experimental findings (534 cm^{-1}) [94]. Since an oscillatory behaviour in time of the magnitude of the main signal is observed in both ground and excited state time-resolved spectra, we reported its FT, where a clear modulation is present by several anharmonically coupled low frequency modes (24, 47, 60, 150 cm^{-1}, reported in 3.12), representing collective vibrational modes that involve both monomers such as dimer breathing, mutual rotations and sliding of molecular planes. [261, 262]

In 3.13 is reported the last analyzed normal mode, representing the C=C stretching motion entirely localized on the TCNE monomer. This mode shows a well defined feature in the ground state centered at 1530 cm^{-1} that is coupled with a less intense signal at 691 cm^{-1}, this last one presumably belonging to an out of phase distortion of the of the TCNE molecule. In a previous experimental study based on spontaneous Raman spectroscopy, [94] the C=C stretching of neat TCNE in acetonitrile solution is assigned to a peak centered at 1565 cm^{-1}. Following the excitation to S_1 electronic state, the TCNE monomer receives electron density promoting an elongation of the central double bond, the vibrational mode becomes localized only on the acceptor molecule, thus the WT spectrum mainly consists of a well resolved and isolated peak at 1485 cm^{-1}. This peak is red shifted (-45 cm^{-1}), as expected, with respect to S_0 and the anharmonic coupling with the lowest frequency mode is now less important. The time-independent analysis are also reported for completeness on the top of 3.13. This trend of the frequency values can be also rationalized considering the lowering of the C=C bond force constant following the excitation, as can be observed by inspecting the mean value of

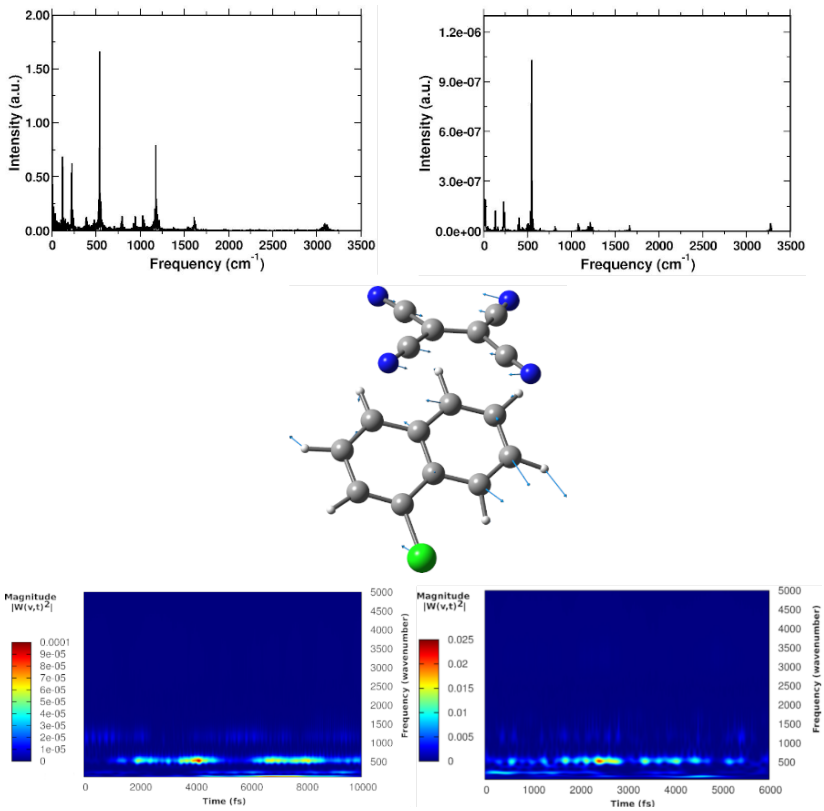

Figure 3.11. Time-independent spectra (top), normal-like mode composition (center) and Wavelet spectra (bottom) of the symmetric CCN bending extracted from ground (left column) and excited state (right column) trajectory.

the double bond distance, computed as average of AIMD trajectories in excited state, that differs of about 0.060 Å with respect to the ground state value (1.374 Å).

In 3.14, we show the temporal evolution of two important internal coordinates as averages over excited state simulations: the CC1, in the 1ClN monomer, and the C=C, in the TCNE molecule, bond distances. Computed average values (CC1: 1.432 Å , C=C: 1.424 Å) along excited states trajectories are in agreement with the previously analysed excited state minima of CT complexes, see 3.2. The Fourier Transform of these oscillating signals pulled out the vibrational frequencies associated, the CC1 distance showed a main peak centered at 1384 cm^{-1} with a weak shoulder at 1391 cm^{-1}, the C=C

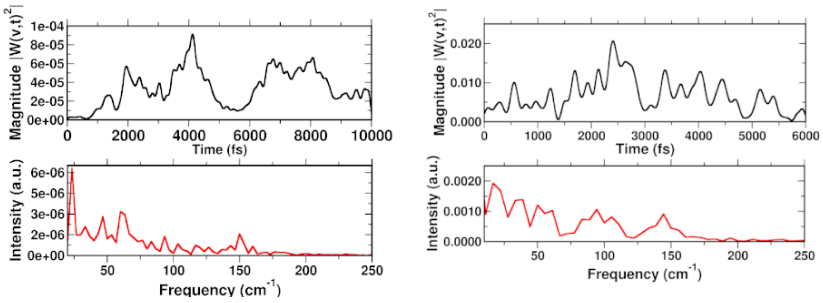

Figure 3.12. Magnitude fluctuations for the symmetric in plane CCN bending mode, from GS (left panel) and ES (right panel) Wavelet power spectra extracted in the time (top) and frequency domains (bottom).

frequencies were found about 100 cm^{-1} red shifted (1478, 1489 cm^{-1}). Furthermore in 3.14, it is clear that there are no mutual overlaps of the two main bands. In the frequency range of 1380-1480 cm^{-1} the TCNE has no active normal modes of vibration as it was verified by the TDDFT frequency calculations conducted on the fully optimized TCNE:1ClN excited state structures. This further supports the observed AIMD results showed in the previous paragraph.

To have a clearer picture of the vibrations involving mostly the 1ClN complex, it was possible to extract the *generalized normal modes* considering only the 1ClN coordinates and momenta from both ground and first singlet excited state molecular dynamics (3.15), having set to zero the momenta associated to the TCNE subunit. It is worth noticing that we were able to individuate and assign the *generalized normal mode*, localized on 1ClN molecule, that corresponds to the vibrational feature experimentally observed at 1392 cm^{-1}. Moreover, this study can support the hypothesis that under this broad spectral feature (FWHM= 55 cm^{-1}) [94] might fall many vibrational modes of 1ClN, typical of the naphtalene moiety. Upon excitation, we found two main isolated and well resolved vibrational features, in which the CC1 stretching played a major role (see 3.15 central panel) peaked at 1392 (weaker) and 1428 cm^{-1}, blue shifted of 16 and 48 cm^{-1}, respectively, compared to those computed in S_0 electronic state. This last trend of frequencies can be also rationalized in light of structural rearrangements reported in 3.4.

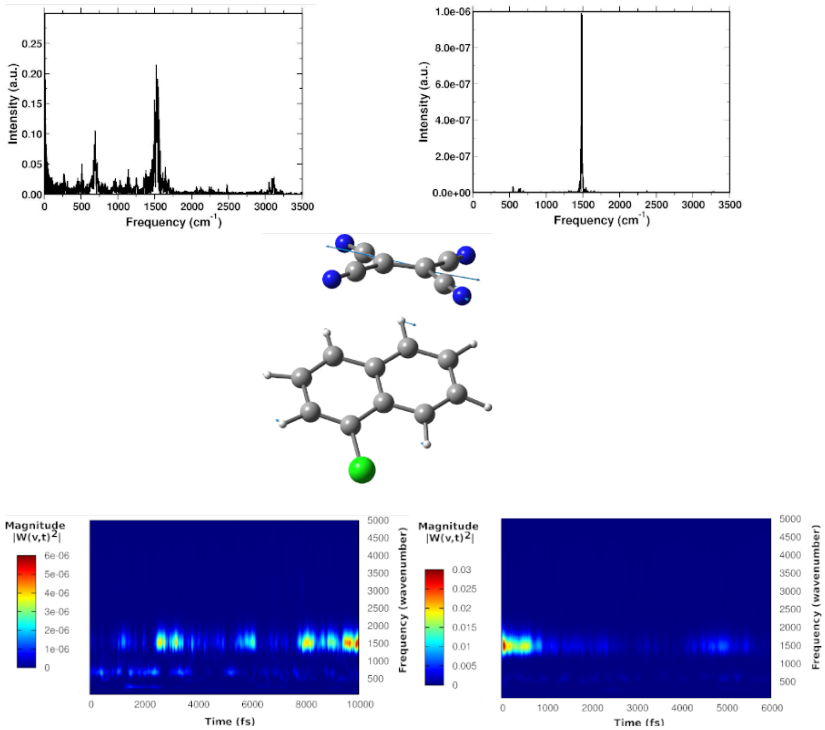

Figure 3.13. Time-independent spectra (top), normal-like mode composition (center) and Wavelet spectra (bottom) of the central C=C stretching extracted from ground (left column) and excited state (right column) trajectory.

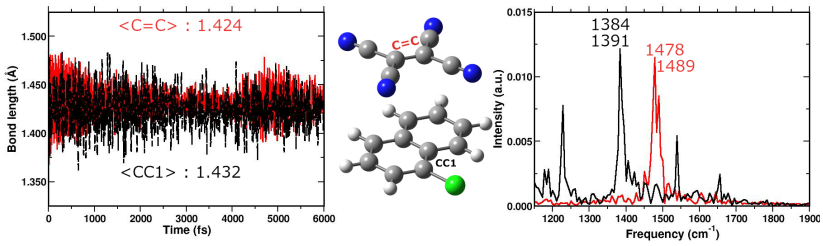

Figure 3.14. Temporal evolution of internal coordinates with the related average values (in Å). Labels and color scheme of bonds is reported in the center. Right: Fourier Transform time-independent spectrum in the 1150-1900 cm^{-1} region.

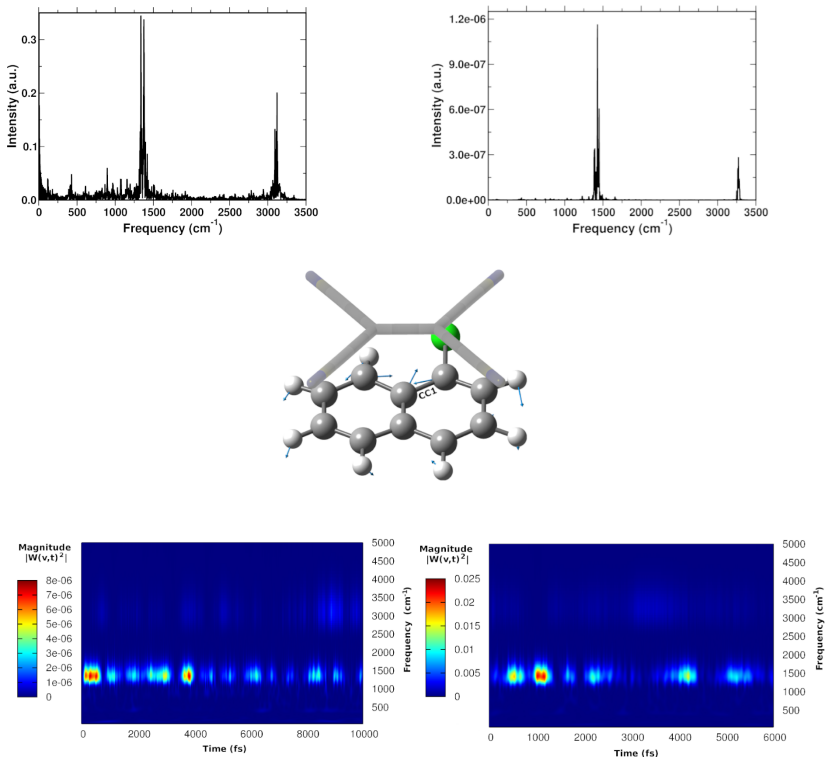

Figure 3.15. Wavelet spectra related to vibrational modes involving mainly the CC1 bond stretching (central panel) having silenced the TCNE molecule, reported in gray, extracted from ground (left) and excited state dynamics (right), the corresponding FT spectra are reported on top and are peaked at 1338, 1380 cm^{-1} and 1392, 1428 cm^{-1}, respectively.

3.3.3 Effects of TCNE:M^+ coordination sphere on vibrations

From FSRS experiments conducted on TCNE:1ClN CT complex in dichloromethane solution, Mathies and coworkers [94] assigned the excited state C=C stretching mode of TCNE to 1392 cm $^{-1}$ taking into account that the ground state vibrational spectra of chemically reduced TCNE with NaI or KI in acetonitrile solution, showed two peaks at 1390 and 1421 cm^{-1} assuming that these peaks were due to the C=C stretching of the $TCNE^{\cdot-}$ for which the countercation was *inside* or *outside* the solvation shell. We theoretically investigated also the possible coordination sites of the TCNE with respect to Na^+ or K^+ counterion, in implicit ACN solvent, (3.16) to elucidate the main structural changes and vibrational frequencies of the central C=C bond when coordinated together. We found that two stable geometries that correspond to two different coordination sites on the TCNE molecule, were present. The TCNE:M^+ pairs have been modeled considering at least three different coordination sites, the C-C=C-C *major* groove, the C-C-C *minor* groove both in the molecular plane and one on the top of the carbon double bond, that have never been isolated. The proximity of the countercation strongly polarizes the central C=C bond, which in the ground state minimum energy structure showed a distance of 1.448 (1.433) Å for the Na^+ ion and 1.446 (1.434) Å for $TCNE^{\cdot-}$:K^+ complex when the ion was in the C-C=C-C *major* (*minor*) groove, (we recall that for the optimized TCNE monomer in ground electronic state in implicit DCM solvent was equal to 1.371 Å and the anharmonic C=C stretching frequency was 1548 cm^{-1}). The two different coordination sites are found to be responsible of two distinct values for the computed Raman anharmonic stretching frequencies associated to this mode: 1367 (1376) cm^{-1} for the $TCNE^{\cdot-}$:Na^+(K^+) when in *minor* grove, 1441 (1432) cm^{-1} for the $TCNE^{\cdot-}$:Na^+(K^+) complex in the other case. Frequency red shifts in perfect agreement with experimental infrared spectra of the $TCNE^{\cdot-}$:Na^+/K^+ anion salts [263, 264], can be also rationalized in light of the difference in electron affinities of the cations accounted in the calculations, 0.046 eV greater for Na than K (0.501 eV). From our investigations we can state that the two vibrational frequencies experimentally observed are due to different coordination sites of the counterion which has been founded in the same solvation sphere of the TCNE.

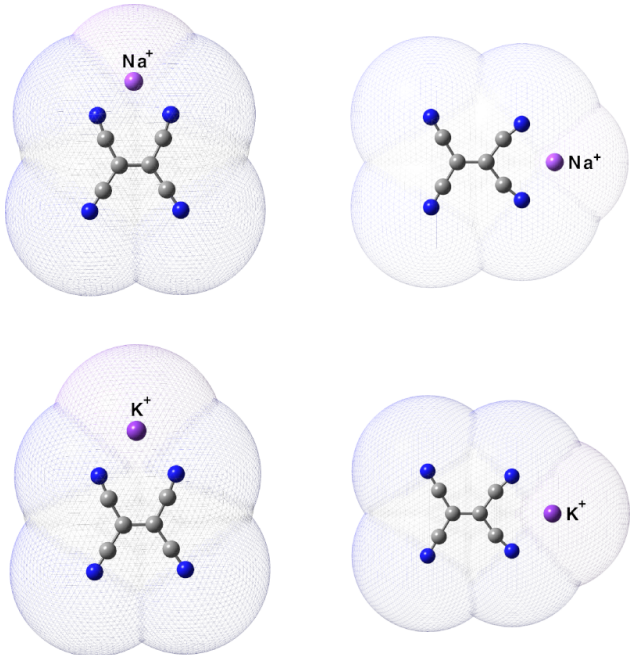

Figure 3.16. Two different coordination sites of TCNE $^{\cdot-}$ with Na^+ and K^+ countercation on the first and second row, respectively. The C-PCM acetonitrile Solvent Accessible Surface cavity is also shown. Left: the counterion is in the C-C=C-C *major* groove, right: the counterion is in the C-C-C *minor* groove.

3.3.4 Molecular determinant to non radiative relaxation paths

In this section, we discuss the possible molecular determinants that probably contribute to the activation of non radiative relaxation channels of the CT complex from the first singlet excited state to the fundamental electronic one. The temporal evolution of selected structural parameters has been extracted from the excited state AIMD simulations and primarily investigated by means of their frequency contents. The previous analysis of vibrational frequencies allowed us to identify the main candidate vibrational modes most likely involved in the non radiative decay: the out-of-plane bending presumably responsible for the back electron transfer event (3.18), the central C=C stretching mode (3.20) and a low frequency collective mode (3.24) which rigidly approaches the two subunits one another. To check our hypothesis both TD-DFT energy scans and first-order NAC elements matrix evaluation were computed for each identified vibrational mode according to the procedure presented in the computational details. In 3.17 NC=CN dihedral angles FT are reported, showing a clear feature at about 160 cm^{-1}, easily assignable to the out of plane bending mode of the TCNE monomer. The corresponding NAC evaluation by displacing along the out of plane-bending mode coordinate (3.18) showed that at the highest value of NAC (0.365 $Bohr^{-1}$), reached when the four cyano groups bend toward the 1ClN unit during the nuclear motion, the TD-DFT energy is 0.150 eV lower with respect to the initial geometry. These are both signs of the high involvement of this motion in the non radiative pathway.

In 3.19 the FT of the C=C bond length temporal evolution shows a clear peak centered at 1478 and 1489 cm^{-1}. TD-DFT energy scans and NAC norms evaluation along the C=C normal coordinate are thus evaluated and reported in 3.20, respectively. When the two carbon atoms approach one another till the closest scanned distance, the TD-DFT energy values reaches its maximum value (+ 1.192 eV with respect to the starting geometry, 1.932 eV) and the NAC trend goes in the opposite direction (up to 0.209 $Bohr^{-1}$). At the largest C=C distance, the TD-DFT values drops off (-0.827 eV) while NACs reaches its maximum value with a high positive slope (up to 0.411 $Bohr^{-1}$). These data suggest that the C=C double bond may be a very sensitive probe of the photoinduced charge transfer extent as well as being a molecular determinant of non radiative relaxation more important than others.

In these regards, we analyzed the normalized distribution between the TCNE's

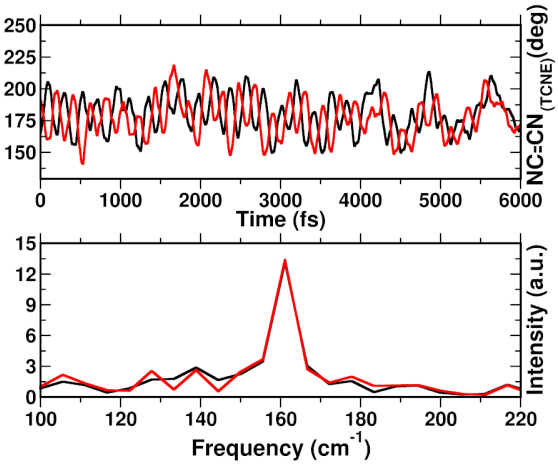

Figure 3.17. Top: temporal evolution of the NC=CN dihedral angles from excited state AIMD trajectory and its Fourier Transform spectrum (bottom).

C=C bond length and S_0-S_1 energy gap values obtained by averaging the three excited state trajectories in 3.21. When the bond length increases, reaching its maximum value, the energy gap of the two PESs moves towards its lowest value. According to this, presumably the C=C distance in the excited state mainly affect the adiabaticity of the two involved potential energy surfaces providing a channel to non-radiative molecular relaxation of the entire TCNE:1ClN CT complex in the ground state. Our results are in agreement with previous X-Ray crystallographic structure determination and vibrational Raman spectra of the $TCNE^n$ [n=0,-1,-2] CT salts. [265] High-precision coupled cluster calculations performed on TCNE molecule in gas phase and acetonitrile solution [236], have also shown that in the excited state the central ethylene bond undergoes an elongation which, besides stabilizing the excited electronic state, also favours a rotation around the internuclear axis.

The electron density redistribution following the photoexcitation has led to a fairly strong change in net charge on both monomers, this has increased the non-covalent interactions by reducing the intermolecular separation between the two subunits ($\sim$ -0.064 Å with respect to GS trajectory). To investigate the role of molecular plane distances in relaxation phenomena at the ground electronic state we report in 3.22 the center of mass distances, computed as averaged value of the three excited state trajectories, and its Fourier spectrum which highlighted the presence of low-frequency vibrational modes mainly

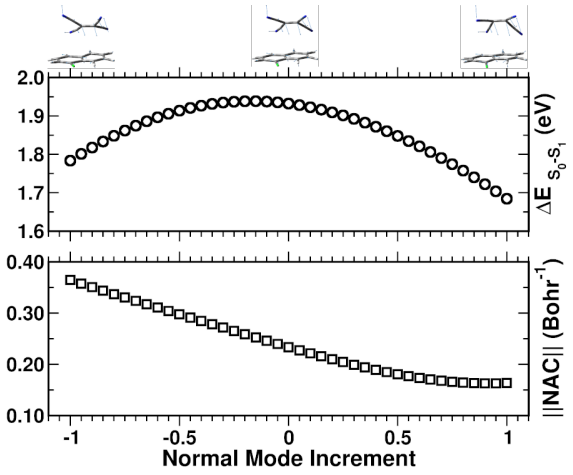

Figure 3.18. Top: TD-DFT energy scan (eV) computed for each δ increment for the $S_1 \leftarrow S_0$ electronic transition. Bottom: Frobenius norm of nonadiabatic coupling matrix computed along with the out-of-plane TCNE bending mode, increased of δ=$\pm$0.05 equal to a deformation of the N-C=C-N dihedral angle of $\sim 0.65°$.

in the 25-90 cm^{-1} spectral range. In 3.24, the TD-DFT energy scan and NAC values computed for each displacement along a low frequency vibrational of rigid approach of the two subunits mode computed for the $MinS0_a$ geometry, showed that the closeness of the two monomers mainly affects the energy separation between the two electronic states reaching a minimum excitation energy of 1.988 eV. The distribution on the contrary, did not highlight a correlation between the average of COM distance and the S_0-S_1 energetic gap, please see 3.23.

In summary, some nuclear motions are expected to participate in non-radiative relaxation phenomena and the investigated vibrational modes here showed to affect in some extent the energy gap between the two PESs. The deformations conducted along the normal mode that mostly contribute to the excited state relaxations are reflected in high values of the non adiabatic coupling elements and low energy gaps. The characteristic trends observed for C=C stretching mode suggest that it may be, predominantly, a key vibrational mode in the return to the ground electronic state.

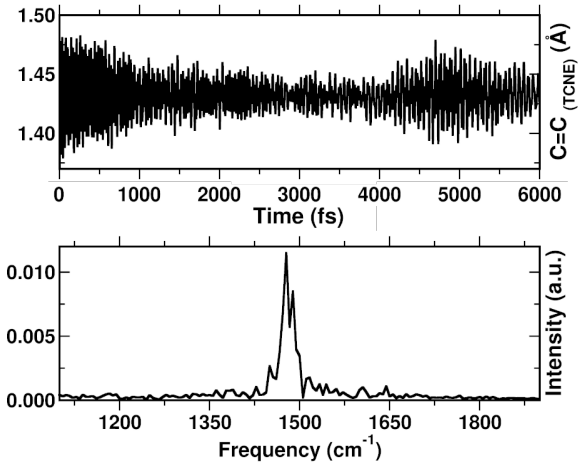

Figure 3.19. Top: temporal evolution of the C=C bond length averaged on three excited state AIMD trajectories and its Fourier transform spectrum (bottom).

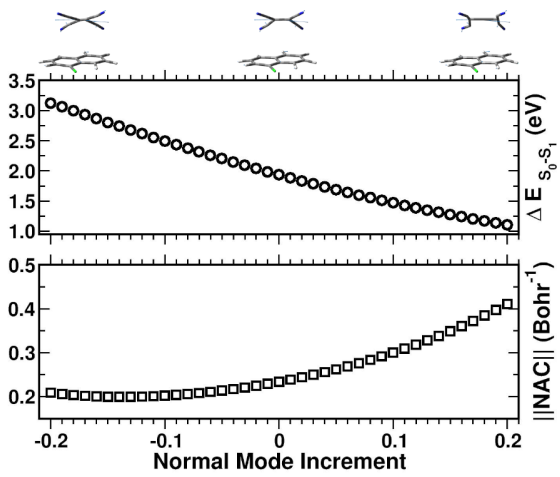

Figure 3.20. Top: TD-DFT energy scan (eV) computed for each δ increment for the $S_1 \leftarrow S_0$ electronic transition. Bottom: Frobenius norm of nonadiabatic coupling matrix computed along with the C=C stretching mode, increased of δ=$\pm$0.01 equal to a deformation of the C=C bond length of $\sim$0.01 Å.

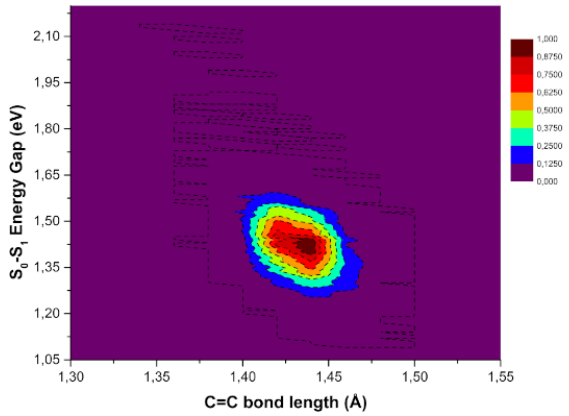

Figure 3.21. Normalized distribution of the C=C bond of the TCNE unit (x-axis) and the energy gap (y-axis) values between ground and first singlet excited state.

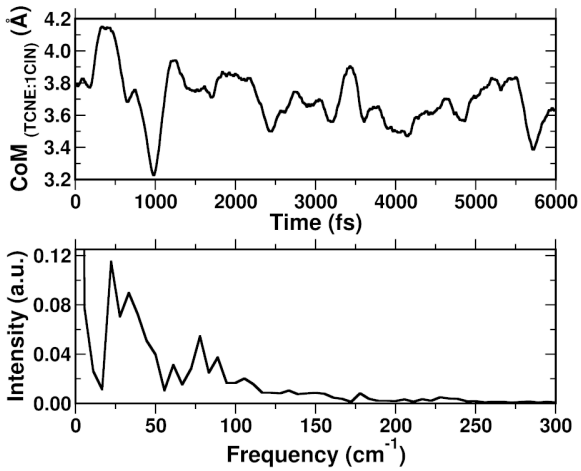

Figure 3.22. Top: TCNE:1ClN center of mass distances computed averaging over the three 6ps long excited state trajectories and its Fourier spectrum (bottom)

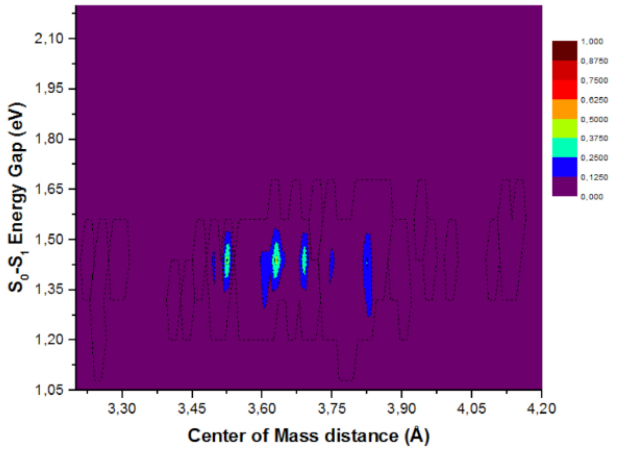

Figure 3.23. Normalized distribution of the center of mass distance between the TCNE:1ClN CT complex (x-axis) and the energy gap (y-axis) values between ground and first singlet excited state.

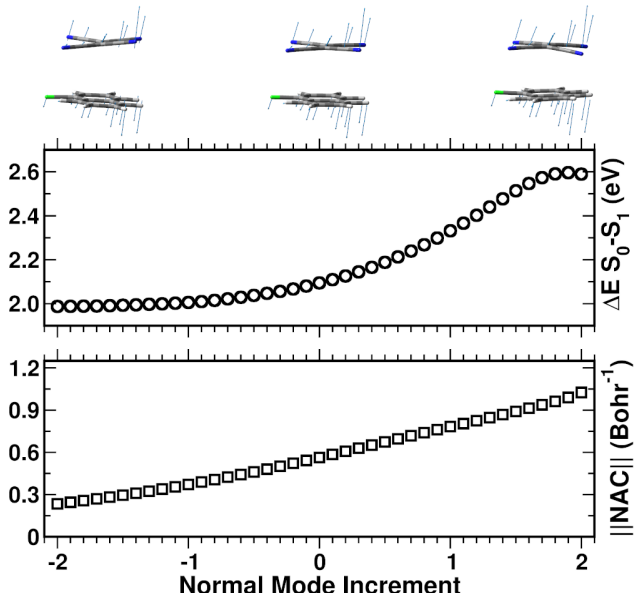

Figure 3.24. Top: TD-DFT energy scan (eV) computed for each δ increment for the $S_1 \leftarrow S_0$ electronic transition. Bottom: Frobenius norm of nonadiabatic coupling matrix computed along with the a low frequency collective mode (at 85 cm^{-1}), increased of δ=$\pm$0.1 equal to a change of COM distance of $\sim$0.033 Å.

3.4 Conclusion remarks

In the present study a prototypical spatially separated molecular system has been investigated in terms of adiabatic molecular dynamics simulation in implicit solvent in both ground and first singlet excited state which showed a strong charge transfer character. The data processing entrusted to the multi-resolution Wavelet protocol, in addition to the precise identification of the main vibrational modes and the associated anharmonic frequencies, allowed us to observe their temporal evolution too. From the Fourier Transform analysis of oscillatory components of such features, the vibrational couplings of the in- and out-of-plane bending modes of the TCNE acceptor with collective low frequency modes, have been discovered. The possible coordination sites of the anionic TCNE with respect to Na^+ or K^+ counterion, have been investigated in implicit acetonitrile solution in terms of geometries and vibrational frequencies of the double bond ethylene moiety. We observed that in the same solvation sphere, there are two non-equivalent coordination sites that distort the initial symmetry and also that the nature of the counterion affects the electron density distribution. Finally, TD-DFT energy scans and first-order NAC elements matrix evaluation were computed on selected nuclear motion to unveil the possible molecular determinants that probably contribute to the activation of non radiative relaxation channels of the CT complex, actually the central C=C stretching mode suggest that it may be, more than others, a key vibrational mode in the return to the ground electronic state. The subtle knowledge of photophysics and photoreactivities in excited electronic states can be monitored and handled to guide and modulate photoinduced process and may useful in the future rational design of photosensitive materials and sensors.

4 First Experimental Evidence of Singlet Fission through Femtosecond Stimulated Raman Spectroscopy

4.1 Background and motivation

In order to stem the catastrophic effects of global warming due to the imposing CO_2 emissions into the atmosphere, many research areas are concerned with exploiting chemical-physical processes to improve the conversion of solar energy. It is important that these new generation materials are able to convert solar energy into electrical potential energy with the highest possible yield by limiting dissipation in the best way. The Shockley-Quessier limit imposes a maximum conversion threshold (photon - exciton, $1 \rightarrow 1$) equal to 33%, this due to heat dissipations which decrease the potential of the photovoltaic cells. A valid strategy to overcome such theoretical limit is to exploit photophysical processes, known as multiple exciton generation, that are able to give a $1 \rightarrow 2$ conversion, boosting the overall efficiency up to $\sim 100\%$, and Singlet Fission falls into this category. Recently new systems have been proposed to be used in organic photovoltaic materials to improve their performance, among the various alternatives some new and promising electron acceptors have been proposed. This indene-fused aromatic class of compounds [266, 182, 183] showed strong light absorption and easy tunability of the frontier orbitals, depending on the functionalization of the indene scaffold

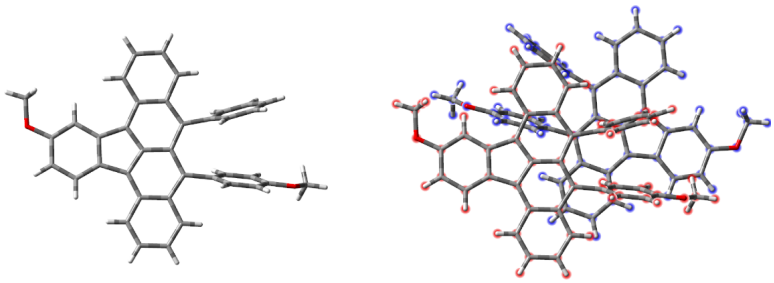

2-Methoxy-9-(4-methoxyphenil)-10-phenylindeno[1,2,3-fg]-tetracene

Figure 4.1. Top view of DimethoxyASI monomer and dimer structures. Carbons are reported in grey, hydrogens in white, red is for oxygens.

and the six peripheral member rings, and they are photostable. The molecular compound that we are going to study here (IUPAC name: *2-Methoxy-9-(4-methoxyphenil)-10-phenylindeno[1,2,3-fg]-tetracene*, shown 4.1) belongs to the asymetrically substituted diarylindenotetracenes compounds, which are recently synthetized and characterized.

These compounds are promising as substitutes for fullerene and fullerene-based compounds in organic electronics and organic photovoltaic devices, given also their relationship to rubrene, a benchmark organic semiconductor. [267, 268, 269] The intrinsic electron deficiency of the molecules containing the indene moiety originates from the 4n-π anti-aromatic system. The driving force towards aromaticity (4n + 2) makes these materials containing indene good electron acceptors. From the X-ray diffraction experiments [183], the crystal structure belongs to the monoclinic $P2_1/c$ space group and the distance between the molecular planes was calculated to be 3.76 Å. The cyclic voltammogram showed that the *DimethoxyASI* compound can undergo two-electron reductions.[183] Finally the UV-Vis spectrum recorded in DCM solution showed strong absorbance in the visible region (λ_{max}= 553 nm, optical bandgap= 1.96 eV). [183] Recently the structural dynamics associated to singlet fission has been succesfully investigated by means of Femtosecond Stimulated Raman Spectroscopy in polyacenes molecules such as pentacene, tetracene [270], rubrene and its derivaties. [271] This organic molecular system is currently under experimental and theoretical examination. The experimental work presented in this thesis has been carried in the Chemistry Department of the University of Minnesota in the laboratories of prof. R.R. Frontiera.

4.2 Methodology

4.2.1 Toward a tailored theoretical-computational protocol to Singlet Fission

We began this computational study by performing preliminary TDDFT benchmark calculations, being available the UV-Vis spectrum of the *DimethoxyASI* system in recorded in dichloromethane (DCM) solution (see 4.1), on the neutral isolated monomer optimized in the ground state at B3LYP/6-31G(d,p) theory level as reported in A.6. We evaluated the basis sets size effects (inclusion of diffusion functions on non-hydrogen and hydrogen atoms), the implicit solvation contribution (DCM) via Polarizable Continuum Model in its Conductor like version (C-PCM) [241, 242, 243, 244, 245, 246] through two different cavities (van der Waals and Solvent Accessible Surface, see A.7) and also the effect of range-separated XC-functional (CAM-B3LYP) on the excited states energies. See tables A.4 to A.7 in the Appendix A. This last part of the work is still in progress and we present some preliminary results. Within the same theory level, B3LYP/6-31G(d,p), both VDW and SAS surfaces induce a redshift of excitation energies (the maximum observed difference was equal to -0.11 and -0.04 eV, respectively). Diffuse functions on heavy atoms also reduce the transitions energy of 0.11 eV with respect B3LYP/6-31G(d,p) case and the solvation effect is consistent as in the previous case (-0.10 and -0.05 eV). Diffuse functions on hydrogen atoms have a similar effect to the previous theory level on the excitation energies: -0.11 eV with respect to B3LYP/6-31G(d,p) and -0.10 (-0.05 eV) when the VDW (SAS) surface is included within the same potential. The absolute errors (AE) computed with respect to the maximum absorbance and the optical band gap (2.24 and 1.96 eV in DCM solution, respectively) is satisfactory for the first and second singlet excited states for the different theory levels considered. The B3LYP/6-31+G(d,p)/C-PCM(DCM) theory level stands out as a good compromise between accuracy and computational cost, the AE respect to the maximum absorbance and band gap is 0.23 and 0.06 eV for the first excited state and 0.00 and 0.28 eV for the second excited state, respectively. At this point the isolated monomer has been optimized again at B3LYP/6-31+G(d,p) level in gas phase starting form the crystallographic structure and the vertical excitation energies have been computed. The AE with respect to the maximum absorbance and the optical band gap turned to be for the first singlet excited state 0.21 eV and 0.08 eV and for the second singlet excited state

0.01 eV and 0.27 eV, respectively. Taking into account the role of the implicit DCM solvent as cavity constructed from van der Waals spheres of the constituting atoms of the molecular systems, the AE is pretty well overlapped to the gas phase: 0.28 and 0.01 eV for the $S_1 \leftarrow S_0$ transition, 0.02 and 0.26 eV for the $S_2 \leftarrow S_0$ transition. The effect of range-separated hybrid functional CAM-B3LYP on the vertical excitation energy has been evaluated on the B3LYP/6-31G(d,p) optimized structure. As discussed above, we took into account both the effect of implicit solvation effect of DCM and the effect of the diffuse functions on heavy and then on hydrogen atoms. At first glance, the CAM-B3LYP XC functional induce a severe blue shift on electronic transitions energy with respect to values predicted at corresponding B3LYP theory level, which for the gas phase cases is close to 1 eV. Again, the inclusion of implicit solvent decreased the excitation energy, the VDW surface acts to a greater extent than SAS (maximum differences -0.15 eV and -0.05 eV, respectively). Diffuse functions on heavy and hydrogen atoms predicted the same values and consequently the same effects on electronic excitation energies (-0.09 eV with respect to the CAM-B3LYP/6-31G(d,p) gas phase, -0.13 and -0.05 eV when the implicit solvent is accounted as VDW and SAS, respectively). The absolute errors computed with respect to the maximum absorbance ranging from 0.07 to 0.17 eV, and from 0.35 to 0.45 eV respect to the optical band gap for the ES_1. The absolute error for the ES_2 electronic transition is greater than the previous case a range that covers 0.40 to 0.44 eV respect to λ_{max} and 0.68 to 0.73 eV respect to the optical band gap. Is known that the Singlet Fission occurs when the $E(S_1 \geq 2E(T_1)$ energy requirement is fulfilled. The unrestricted TD-DFT calculations which are reported in tables A.7 and A.8 in Appendix A, gave us access to the energies of the electronic triplet states. In the cases considered it is found that the first triplet excited state on average lies below the first singlet excited state. For the B3LYP/6-31+G(d,p) case the S_1 state is 0.16 eV more energetic than the T_1 electronic state in the gas phase and when the implicit DCM solvent is accounted as Solvent Accessible Surface (2.04 eV). Instead the T_1 - S_1 energy difference is -0.11 eV for the B3LYP/6-31+G(d,p)/C-PCM(DCM) theory level.

The nature of the first singlet excited state it is mainly HOMO-LUMO with a lower $HOMO_{-1}$-LUMO contribution, while it is completely reversed for the second singlet excited state. The $HOMO_{-1}$, HOMO and LUMO molecular orbitals contour plots which are involved in the first two singlet excited states, are reported in 4.2.

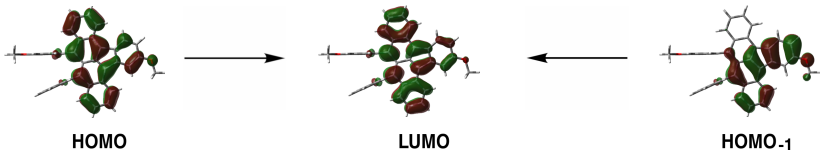

Figure 4.2. Ground state frontier molecular orbitals HOMO, LUMO and HOMO$_{-1}$ (isovalue= 0.02) involved in the first and second singlet excited state, computed at B3LYP/6-31+G(d,p) theory level.

In the first excited state, considering the HOMO-LUMO contribution, the rearrangement of electron density following the photoexcitation, suggested an alternating bond that mainly affects the indenotetracene core with a partial charge-transfer that involved the oxygen of one of the methoxy groups. The electron density rearrangement depicted by the HOMO$_{-1}$-LUMO orbitals shown a greater charge-transfer character from one region of the molecular core to the entire backbone in which the methoxy group has played a main role. For both cases examined here, peripheral phenyl groups did not appear to be particularly involved. In instances like this, in which an electronic state can be described by more than one pair of transition orbitals, natural transition orbitals (NTOs) reported in 4.3 turn out to be particularly useful transforming the canonical orbital representation into a more condensed view in which each excited state is expressed, when possible, as a single pair of orbitals. [272]

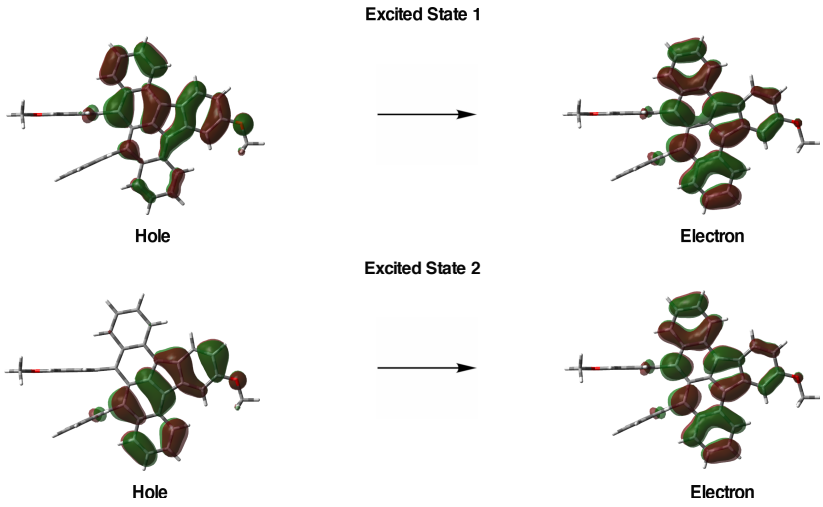

Figure 4.3. Ground state Natural Transition Orbitals labeled as Hole and Electron (isovalue= 0.02), for the first and second excited state, computed at B3LYP/6-31+G(d,p) theory level.

By carefully studying the crystallographic structure of *dimethoxyASI* reported in [183] we have noticed that at least two different dimeric structures can be identified: a first dimer (reported in 4.4, top) in which there is a partial overlap between the peripheral rings of one monomer and the backbone of the other in which the π-π distance is 4.76 Å and a second dimeric structure (see 4.4, bottom) in which the two constituent monomers are more displaced with respect to each other and whose molecular planes are closer together, about 1 Å less.

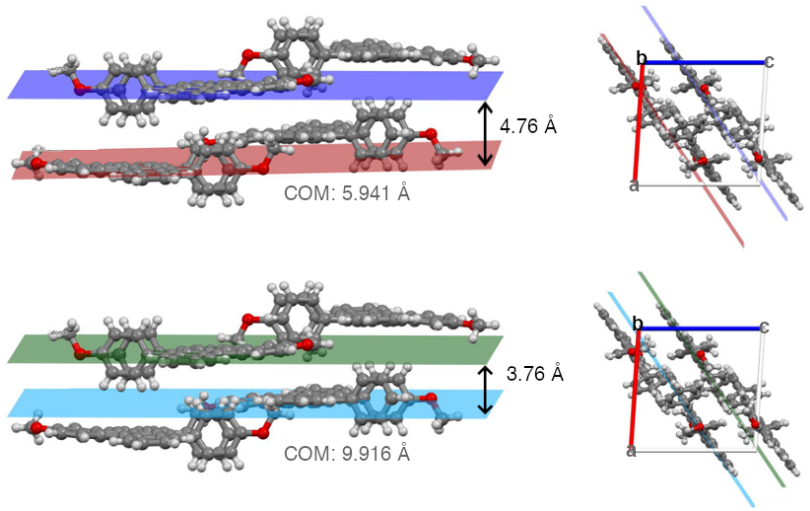

Figure 4.4. Two different dimers identified in the crystallographic structure. Top left: structure called $Dimer_1$ in custom view to enhance the molecular planes and along the *b*-axis (top right) Bottom lef: structure called $Dimer_2$ in custom view to enhance the molecular planes and along the *b*-axis (bottom right). The center of mass distance (COM) between the two subunits that identify the molecular planes is reported in gray for each adduct.

In order to perfect the crystallographic structures without changing the relative orientations and the distance between the molecular planes constrained geometric optimizations were carried out by fixing the coordinates of all the atoms except for the hydrogens. In this way all the C-H bonds have assumed the correct bond length going from 0.9 to 1.08 Å on average. The partially optimized structures of each dimer in gas phase are shown in A.8 in Appendix A.

To investigate the energetics of the Singlet Fission process, TD-DFT preliminary calculations have been performed starting from the crystallographic structures of each dimer. Looking at the molecular orbitals that define the

greatest contribution to the lowest singlet excited state in the $Dimer_1$ we found that the $S_1 \leftarrow S_0$ electronic transition has a charge-transfer character while the remaining electronic transitions are Locally-Excited with a partial intramolecular charge transfer. On the contrary, the nature of all the electronic transitions computed for $Dimer_2$ are Locally-Excited type and no intermolecular charge transfer has been observed but higher energy intramolecular charge-transfer. In 4.5 we report the frontier molecular orbitals of the first singlet excited state computed at TD-B3LYP/6-31+G(d,p) in gas phase and a scheme of the energies of the electronic levels potentially involved in the SF process, that is S_1 and T_1. The energy difference between states S_1 and T_1 suggests that the prerequisite for Singlet Fission for both systems under study is satisfied and that the photophysical process can therefore proceed endothermically. [273]

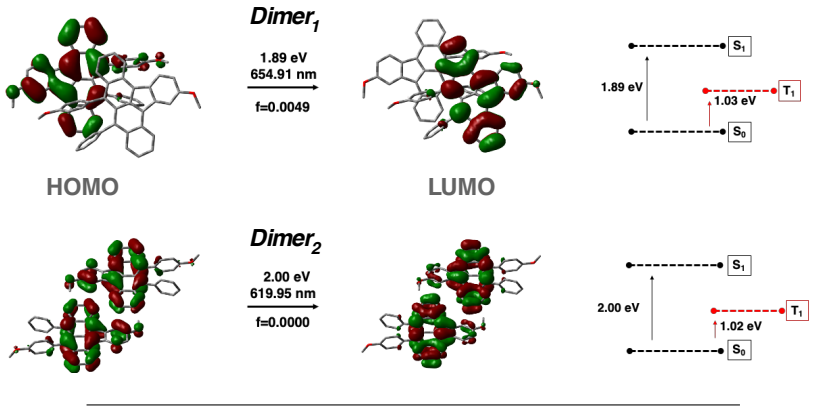

Figure 4.5. Frontier molecular orbitals and vertical excitation energy (in eV and nm) from the ground to the first singlet excited state computed at TD-B3LYP/6-31+G(d,p) on the isolated dimeric structures *Dimer*$_1$ and *Dimer*$_2$. Pictorial energy scheme of the electronic states involved in the SF process.

The amount of charge transferred between the two subunits in both ground and first singlet excited states have been quantified for each dimeric structure by employing the Natural Bond Orbitals (NBO) charge partitioning scheme [230, 231, 232, 233, 234, 235] reported in A.9 in Appendix A. In the *Dimer*$_1$ case, following the excitation there is a redistribution of the charge between the two monomers which involves mainly the tetracene backbones and the indene moiety, overall there is the transfer of a quantity of charge close to the unit ($\pm$ 0.963 e). A local redistribution of the charge in each monomer which involves mainly the tetracene backbone and the indene moiety has been observed upon excitation for the *Dimer*$_2$.

The preliminary results just described revealed that we are facing an appealing system that can serve as a model for the Singlet Fission process. Through an integrated and synergic approach between theory and experiment it will be possible to give new insights regarding the mechanistic aspects of this photophysical phenomenon which are still debated. In this specific case, the detailed knowledge of electronic and nuclear properties, such as the directions of transition electric dipole moments and the phonon modes compositon of the two dimeric systems will trace the way forward in the near future for the setup of new experiments aimed at studying the structural dynamics and to the photophysical characterization of each pair.

4.2.2 Experimental methods

Since the experimental conditions of crystallization are not yet known and it is also the first time that this new compound is being studied, the first step of this work concerned the optimization of experimental conditions to grow crystals. The sample, stored in the freezer, looks like an intense purple powder and we had $\sim$ 4.3 mg. At the beginning we tried to get crystals using the Physical Vapor Transport (PVT) method setting different temperature gradients - based on what is known about similar compounds - at an Argon flow rate of 50 cc/min, but without success. Then we tried, as second test, to obtain crystals from sample solutions and this led to the growth of crystals. We prepared 3 solutions of our sample, which have been visually monitored for several days:

1. chloroform ($CHCl_3$), kept at room temperature under the hood;
2. chloroform + methanol ($CHCl_3$ 1:2 CH_3OH), kept in the fridge;
3. methylene chloride + methanol (CH_2Cl_2 1:2 CH_3OH), kept in the fridge.

The crystals obtained from the first solution were transferred onto a laboratory slide 4.6 and fixed with an epoxy glue, for further measurements: microscope observation, UV-Vis absorption, CW Raman, Transient Absorption, Femtosecond Stimulated Raman Spectroscopy.

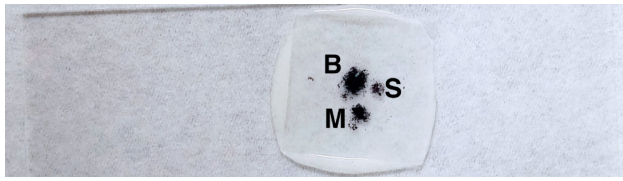

Figure 4.6. Laboratory slide on which the crystals have been fixed. The label **B** states for Big, **M** states for Medium and **S** for Small spots.

The images of the crystals, reported in the next section, were obtained at the Olympus microscope IX73P2F with a 10x/0.25 achromatic objective lens.

The absorption spectrum of crystals, in the UV-Visible range, has been recorded from 185 nm to 1400 nm by using UV2600 UV-Vis spectrophotometer by Shimadzu in transmission mode.

The spontaneous Raman spectra of *DimethoxyASI* crystals has been obtained on a in-house built optical table using a 785 nm laser (laser power at the sample, 80 mW) focused onto a 10x Olympus objective in Transmission setup

and a CCD array as detector (Princeton Instruments PIXIS 400BX). Spectra were collected in a single window between 620 and 1720 cm^{-1}. Raman shifts calibration has been performed by recording the spontaneous Raman spectrum of cyclohexane at RT and preceded the measurements performed on the sample, see A.14 in Appendix A.

Femtosecond Stimulated Raman spectrum and Transient Absorption have been collected on a home-built setup that employed a Coherent model Libra-F-1K-HE-110 fs amplifier.

For detailed technical specifications, see Appendix A.

All data analysis is performed in IGOR Pro [274] using custom-developed procedures.

4.3 Results and discussion

The observation under the microscope allowed us to define the shape and type of the crystals, some collected images are shown in 4.7. The crystals are needle-like and intensely dark purple colored.

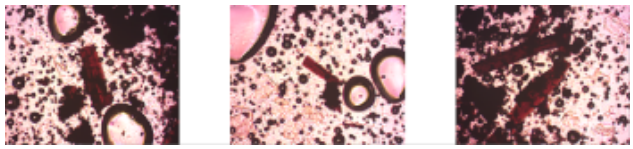

Figure 4.7. *DimethoxyASI* dark purple needle-like crystals under 10x microscope observation. (Circular objects are air bubbles trapped in epoxy glue.) The scale bar is X mm.

Crystals have been firstly characterized by means of UV-Vis spectroscopy. The UV-Vis spectrum has been recorded by scanning the available wavelengths from 185 to 1400 nm as first exploratory step and then recorded in the 200 - 870 nm region, in 4.8 the 350 - 750 nm range is reported. In A.10 in the Appendix A the UV-Vis spectra recorded on the Big and Small spot, cf. labels in 4.6, is reported along with the exploratory spectrum. At first glance we noticed that the steady-state absorption spectrum of the crystals covers the entire solar spectrum and also we can recognize distinct macroregions of interest: from $\sim$ 340 to $\sim$ 480 nm, between $\sim$ 500-600 nm and 650-700 nm. The gaussian fitting performed on the UV-Vis spectrum (solid red trace, see A.11 and A.12 in Appendix A) helped us to assign features with a higher degree of confidence. The present spectrum can be resolved into, at least, five absorbance bands located at: 377, 421, 529, 570, 624 nm.

UV-Vis Experimental results

DCM solution [183]	Crystal [this work]
390 (3.18 eV)	421 (2.94 eV)
420 (2.95 eV)	529 (2.34 eV)
550 (2.25 eV)	570 (2.19 eV)
	624 (1.99 eV)

Table 4.1. UV-Vis absorptions in nm (eV) observed in DCM solution (left column) and in *DimethoxyASI* crystalline form. The absorption band at 377 nm is not well resolved and is doubtful.

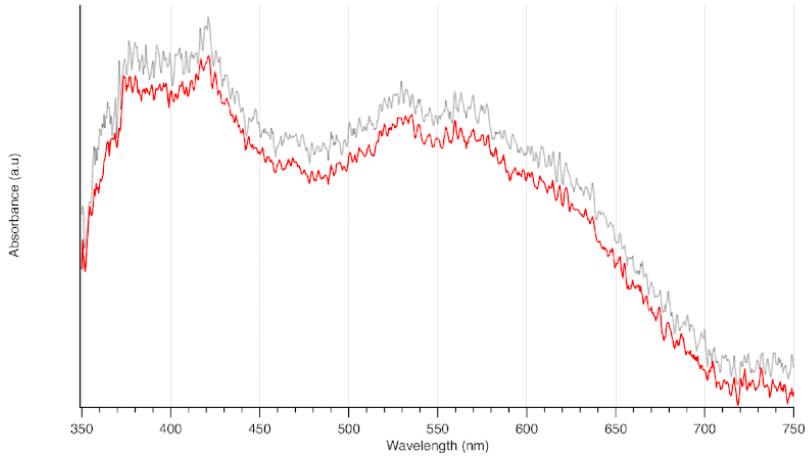

Figure 4.8. Big spot UV-Vis absorption spectrum recorded in the 350-750 nm range. The gray dot trace is for *medium* speed acquisiton velocity, red solid trace is for *very slow* acquisition velocity. Vertical dashed lines are shown for the main ticks for better reading.

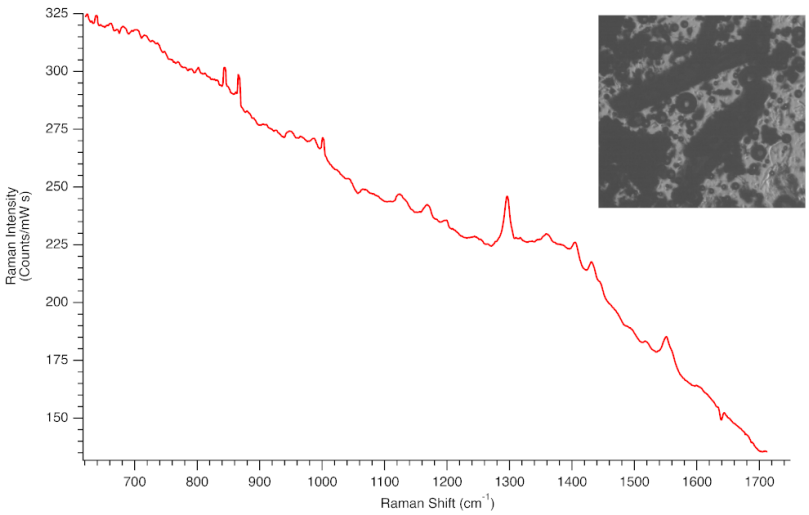

Figure 4.9. Ground state spontaneous Raman spectrum of the *DimethoxyASI* crystal recorded in the 620 - 1720 cm^{-1} spectral region. The inset shows a microscope image of crystal.

The ground state Raman spectrum of the crystals, recorded for the first time with 785 nm excitation, is shown in 4.9, the sloped baseline could be due to fluorescence phenomena by the slide or due to the small size of the crystals. Through the data analysis performed throughout the spectral range by gaussian fitting, reported in Appendix A in A.15, A.16, A.17, A.18, A.19, we found several Raman features that can be assigned with the aid of DFT Raman frequency calculation on the isolated monomer. Corresponding normal modes, computed on the ground state for the isolated monomer optimized at B3LYP/6-31+GDP theory level, are reported in 4.10.

N.	**Exp. (cm^{-1})**	**Isolated monomer (cm^{-1})***	**Assign.**
1	844	832	Peripheral CH wagging
2	867	877	Rings breath.
3	987	992	Ring deformation
4	1001	1008	Ring breath. + HCCH rocking
5	1127	1128	HCCH rocking
6	1169	1165	CH_3bending + HCCH in plane bending
7	1197	1211	HCCH scissoring
8	1296	1290	HCCH rocking + CC stretching
9	1360	1366	HCCH rocking + CC stretching
10	1405	1409	HCCH rocking + CH_3 umbrella + CC stretching
11	1434	1435	HCCH rocking + CH_3 umbrella + CC stretching
12	1521	1527	Tetracene core CC stretching
13	1554	1555	Ring CC stretching
14	1607	1606	Tetracene core CC stretching

Table 4.2. Relevant experimental Raman peaks and scaled Raman frequencies for selected vibrational modes. *Scaling factor: 0.964.

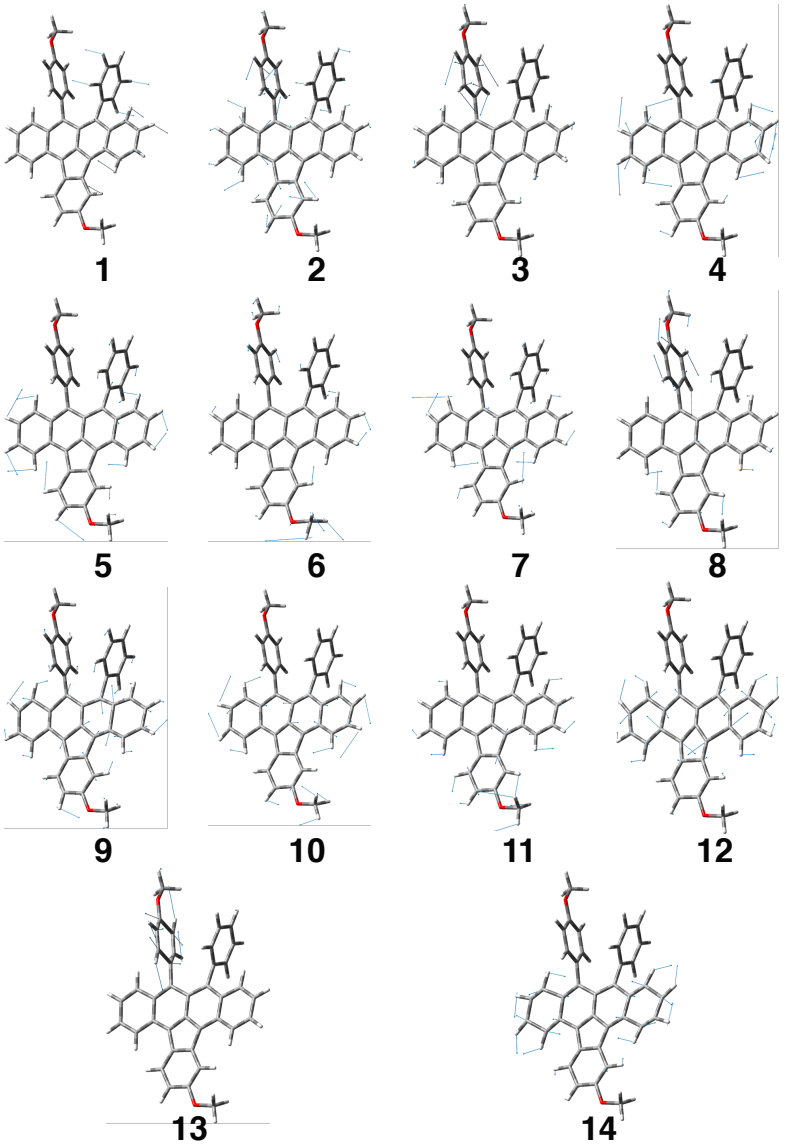

Figure 4.10. Normal modes displacement vectors computed at B3LYP/6-31+G(d,p) associated to the 14 Raman peaks observed in 4.9. Scaled frequency values and description is reported in 4.2.

The TA spectrum shows the temporal evolution associated to the fraction of molecules promoted to electronically excited state by means of actinic pulse. In the TA spectrum 4.11 is observed that the excitation is very fast (starting from the time origin of the experiment, 1 fs) and the three very long-lived bands at 1.433, 1.382 and 1.333 eV, do not decrease in intensity in the time interval considered - up to 50 ps. These preliminary evidences could be due to the presence of long lived electronic states and therefore attributable to triplet states, trapped excitons or charge transfer state. For a full understanding and interpretation of the features present in the TA spectrum a theoretical-experimental synergic approach is indispensable.

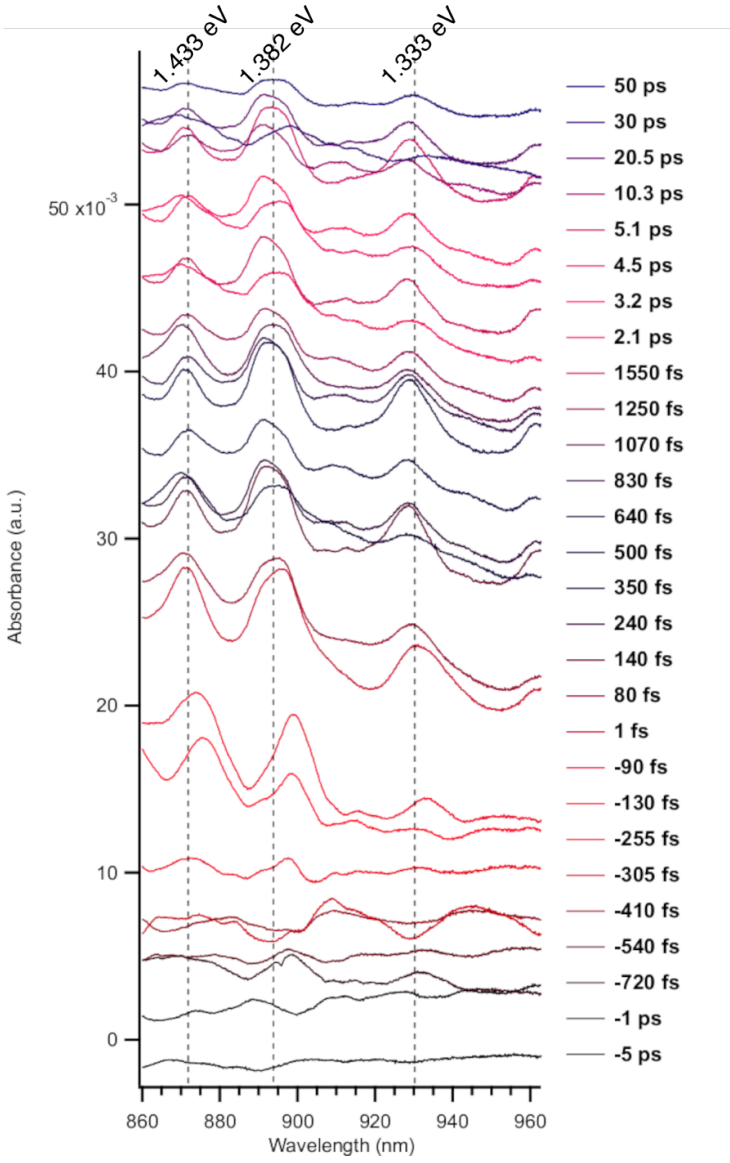

Figure 4.11. Femtosecond Transient Absorption spectrum of the *DimethoxyASI* recorded on single crystal at various time delay relative to photoexcitation, in the 860 - 960 cm^{-1} spectral region.

Raw FSR data plot in the 800 - 2000 cm^{-1} spectral region of *DimethoxyASI* single crystal following the subtraction of excited state spectra from the ground state spectrum (1:1) is shown in 4.12. The ground state spectrum (thick red trace in 4.12 scaled by 1/5) shows three peaks at 1286, 1425 and 1544 cm^{-1} according to the DFT harmonic frequency calculations they can be assigned to C-H in plane bending motions and CC stretching of tetracene core and anisole-like ring (see the table 4.2 and 4.10). All three show depletion in amplitude upon photoexcitation and there are no hidden excited state features after re-add the ground state. Furthermore, we observed two satellite features close to 1000 and below 1800 cm^{-1}. To examine the excited state dynamics it will be necessary to add the ground state spectrum for a more accurate analysis. We are currently analyzing additional data sets that we have collected, only one data set is shown here. Each ground state peak amplitude has been fitted with a gaussian function, which was then used for fitting the corresponding amplitudes in the excited state. Figures 4.13, 4.14 and 4.15 show the Raman depletion of the 1286, 1425 and 1544 cm^{-1} modes, respectively. The oscillating behavior over time, particularly evident within the first 4 ps could be a symptom of a vibrational coupling with some other vibrational modes. In principle it is possible to apply the Fourier Transform to obtain the frequencies associated with these oscillations. Since for this preliminary data series, the fitting did not return equal spaced points, we think the Fourier Transform can lead to misleading results. We are currently collecting additional data to unambiguously quantify the vibrational couplings and the kinetic associated to such vibrational modes.

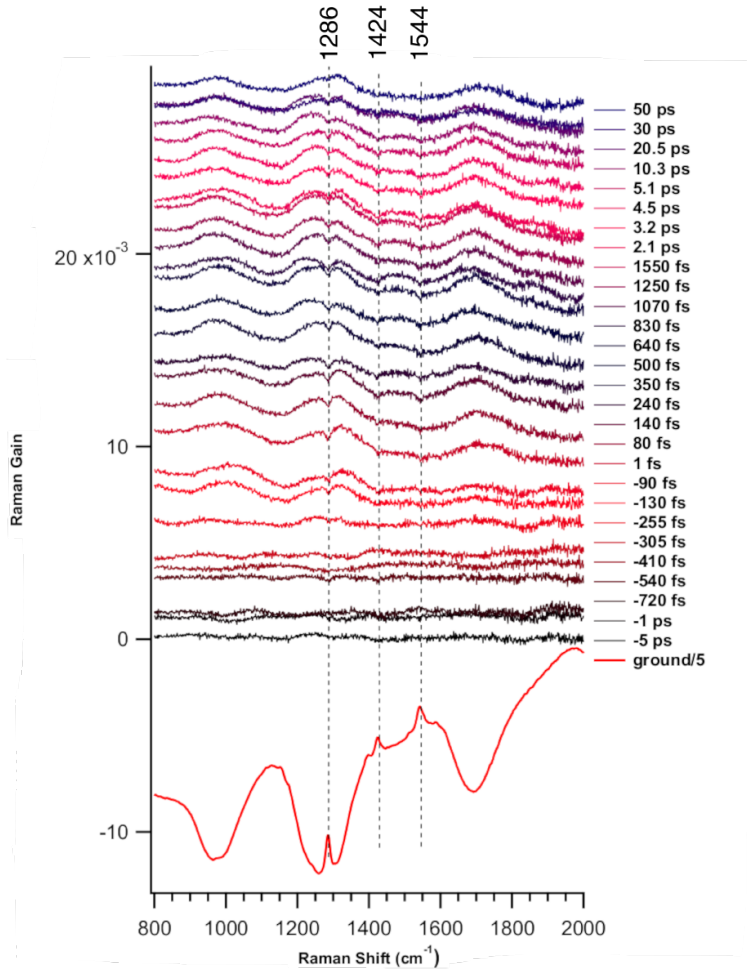

Figure 4.12. Femtosecond Stimulated Raman spectrum of the *DimethoxyASI* recorded on single crystal at various time delay relative to photoexcitation, in the 800 - 2000 cm^{-1} spectral region.

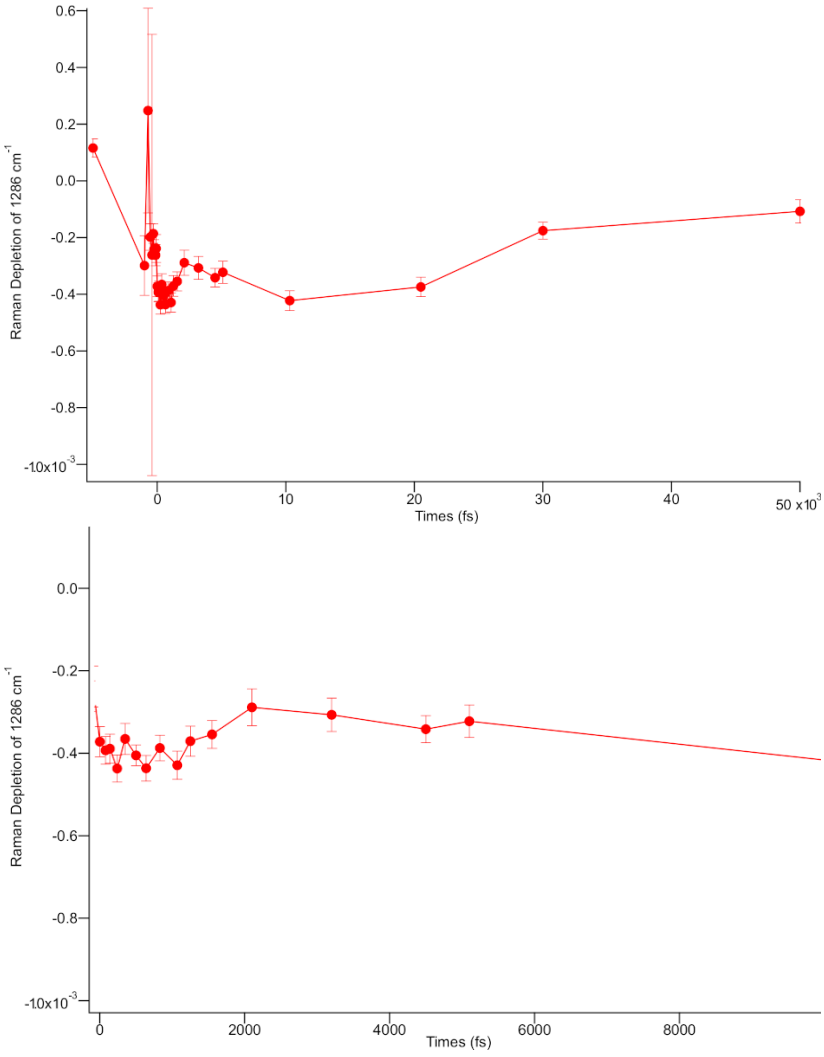

Figure 4.13. Upper panel, Raman depletion profile of 1286 cm^{-1}, mode n.8, during the time (fs). Bottom panel, enlarged region around 0 - 10 ps to better show the oscillating behavior.

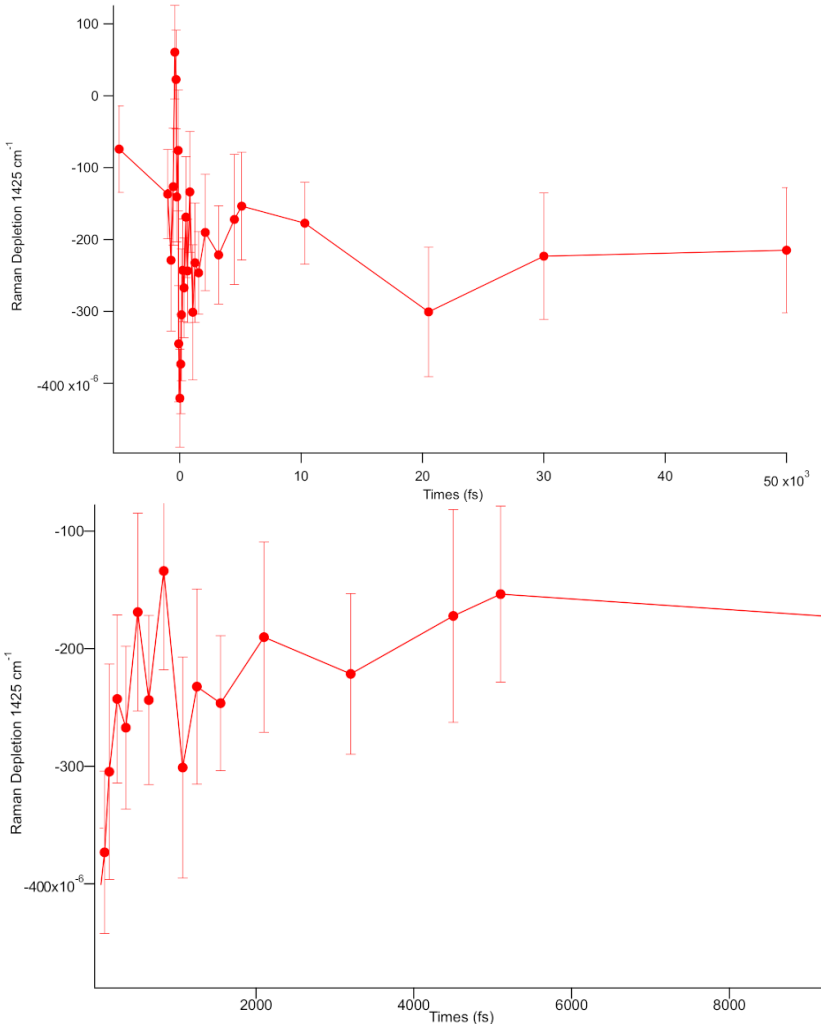

Figure 4.14. Upper panel, Raman depletion profile of 1425 cm^{-1}, mode n.11, during the time (fs). Bottom panel, enlarged region around 0 - 10 ps to better show the oscillating behavior.

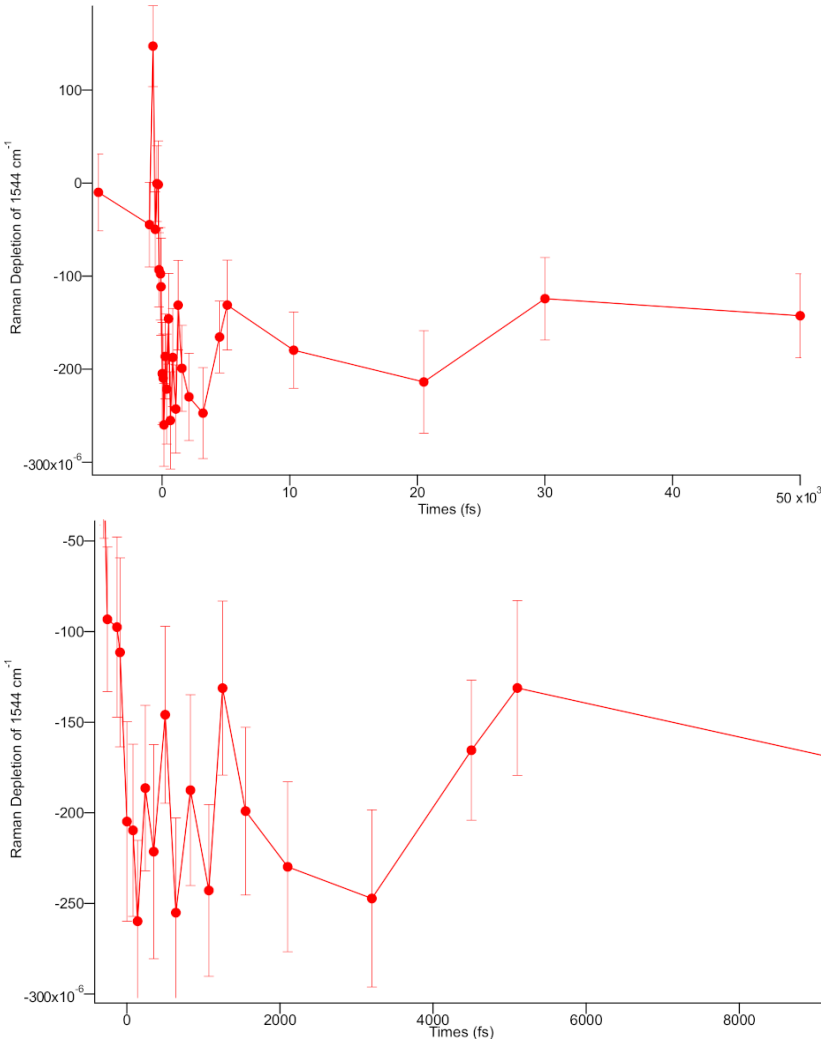

Figure 4.15. Upper panel, Raman depletion profile of 1544 cm^{-1}, mode n.13, during the time (fs). Bottom panel, enlarged region around 0 - 10 ps to better show the oscillating behavior.

4.4 Conclusion remarks

In this study which is still progressing, we have faced the study of a new system recently synthesized. The first step concerned the optimization of the experimental conditions for obtaining the crystals. We proceeded with the spectroscopic characterization of the crystals through UV-Vis spectroscopy and Raman spectroscopy for the ground state. The experimental results were also interpreted with the help of preliminary DFT and TDDFT calculations. Thanks to time-resolved spectra, we got some first insights about the Singlet Fission event in this new molecule. The presence of features in the Transient Absorption spectrum could indicate that following photoexcitation triplet excitons or trapped excitons are generated. A preliminary analysis of the FSRS spectrum suggests that there is no charge transfer intermediate during the process, unlike as observed in previous cases. [270] We would need to deepen the study and acquire spectra with a greater number of data points to study the dynamics and possibly the vibrational couplings. We are currently collecting new data to improve interpretation and reveal the structural dynamics associated with singlet fission and triplet separation. Next to this we will proceed with the study in solution to start the development of a computational protocol tailored from the monomer case first, up to higher structures. Given the size of the models being studied, DFT and TD-DFT are the only feasible electronic structure theories. We are proceeding to the fine and careful calibration of the potential for the monomer and the dimer system for the accurate study of the excited states. The goal is to know the fate of the excited states through the vibrational relaxation - in the singlet and then in the triplet state - and to describe the experimental results at atomistic and molecular level giving useful insight for the rational design of new molecules in the field of organic electronics. We will use *ab-initio* molecular dynamics simulations on a single Born-Oppenheimer surface extending the existing protocols developed in this research group by introducing the effects of the crystalline environment (e.g. QM / MM simulations or vibrational bath).

5 Conclusions and Future Perspectives

The aim of this PhD project has been the development of theoretical - computational methods for the study of photophysics and photoreactive events that occur on ultrafast time scales following the photoexcitation and far from Franck-Condon region. We have exploited the capabilities of ab-initio molecular dynamics integrated with an analysis protocol based on the multiresolution Wavelet analysis that gave us the opportunity to have a vis-à-vis comparison with modern time-resolved vibrational spectroscopic techniques. Indeed, the connection of the spectroscopic data with the structural and the dynamical features is far to be an easy task. Plenty of information is provided by interpreting trends in the time of vibrational frequencies, frequency fluctuations and/or frequency shifts, anharmonicity and couplings of the vibrational motion, which are subtle probes of structural motifs and reaction mechanisms. We have faced with the theoretical study of two non covalent charge transfer (CT) systems with complex and intriguing photophysics for which we have been able to prove that the protocol we have adopted proves to be very versatile and robust despite their challenging excited state chemistry. The accurate description provided by the ab-initio molecular dynamics made possible the interpretation of nuclear relaxation and allowed us to suggest a better assignment of vibrational frequencies. From the time-resolved vibrational spectra we were able to quantify the anharmonic vibrational couplings between high and low frequency modes. Finally we were able to correlate vibrational fingerprints to electronic properties, determining which vibrational modes associated with structural parameters influenced the adiabaticity of the electronic states involved. Indeed, regarding the first CT complex (TCNQ:π:TMB) discussed in Chapter 2, the time-resolved vibrational analysis of the temporal evolution of the electronic energy gap $S_0 \leftarrow S1$ revealed the presence of a vibrational mode localized on the acceptor monomer, TCNQ, that modulates

the energy gap between the ground and first singlet excited state potential energy surfaces, in full agreement with the experimental hypotheses. The nonadiabatic coupling matrix elements computed on several selected structures displaced along selected generalized normal modes of the TCNE:π:1ClN CT complex - Chapter 3, extracted from ground state *ab-initio* molecular dynamics trajectory suggest that the C=C stretching and the out of plane bending mode of the TCNE monomer are key vibrational modes in non radiative relaxation mechanism of the entire CT complex to the ground electronic state. The work is proceeding with an experimental study concerning the spectroscopic characterization through time-resolved vibrational spectroscopies of a promising electron acceptor system which could be used in the organic electronic and photovoltaic fields. Femtosecond Stimulated Raman Spectroscopy and Transient Absorption can elucidate the excited state structural dynamics associated to very fast photophysical and photochemical events such as the Singlet exciton Fission. Now we are optimizing the experimental conditions to obtain crystals more easily through Physical Vapor Transport and we are collecting new spectroscopic data to study the structural dynamics associated with Singlet Fission and any intermediates in order to have details on the mechanism which is still debated. A detailed spectroscopic study in solution will allow us to develop a tailored computational protocol on the monomeric system and then we will consider multicromophoric systems.

A Appendix

A.1 TCNQ:π:TMB, ground state minimum energy structures

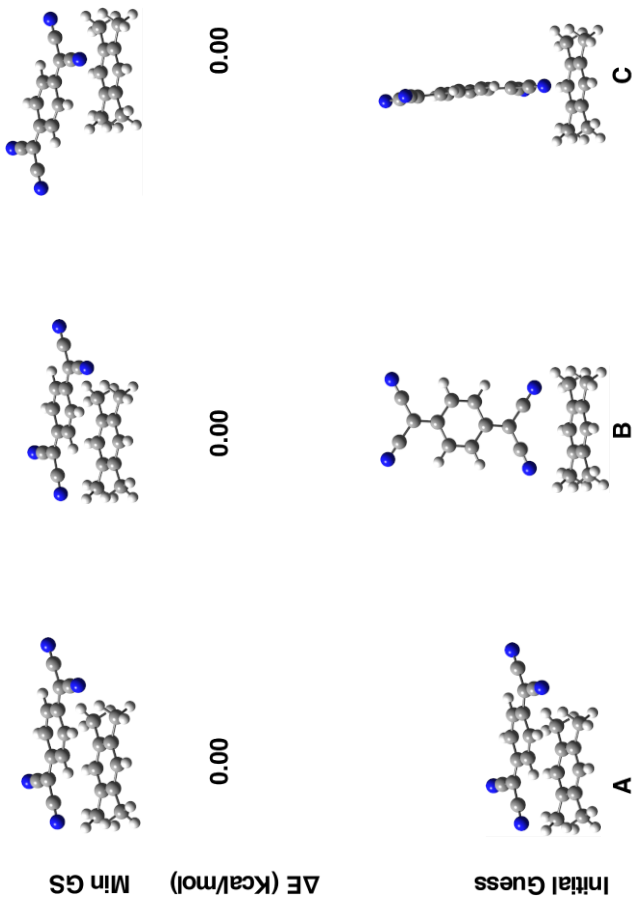

Figure A.1. Starting molecular guess (bottom) and optimized structures (top) in ground state (S_0) ordered according to the relative energy (in Kcal/mol)

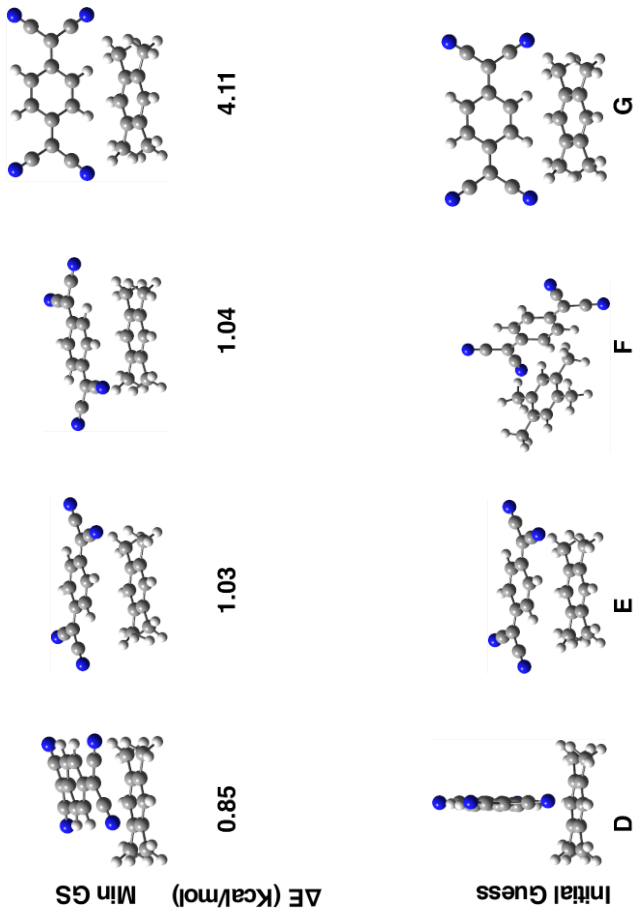

Figure A.2. Starting molecular guess (bottom) and optimized structures (top) in ground state (S_0) ordered according to the relative energy (in Kcal/mol)

A.1.1 TCNQ:π:TMB, TD-DFT single point calculations

Table A.1. $S_1 \leftarrow S_0$ TDDFT SP calculations at CAM-B3LYP/6-31+G(d,p)/GD3, performed on ground stare minum energy structure at B3LYP/6-31+g(d,p)/GD3 theory level.Vertical Excitation Energy (in eV), the oscillator strength (f) and the largest MOs coefficient are reported.

	VEE (eV)	***f***	**MOs coeff.**	**Electronic Transition**
A	2.286	0.1843	-0.23087	**L** $\leftarrow$ **H-1**
			0.66543	**L** $\leftarrow$ **H**
B	2.157	0.1166	-0.16256	**L** $\leftarrow$ **H-1**
			0.68435	**L** $\leftarrow$ **H**
C	2.158	0.1165	-0.16245	**L** $\leftarrow$ **H-1**
			0.68438	**L** $\leftarrow$ **H**
D	1.979	0.0034	0.70033	**L** $\leftarrow$ **H**
E	2.163	0.1165	0.69856	**L** $\leftarrow$ **H**
F	2.072	0.0313	0.70273	**L** $\leftarrow$ **H**
G	1.981	0.000	0.70524	**L** $\leftarrow$ **H**

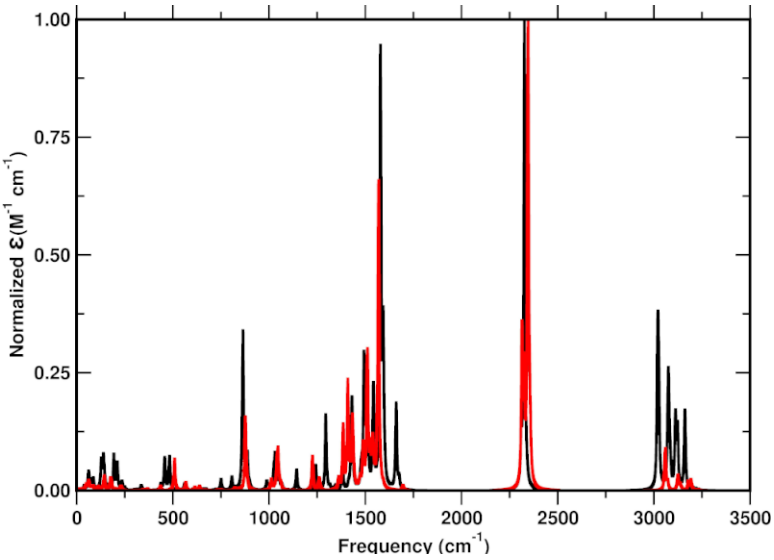

Figure A.3. Normalized ground (black) and first singlet excited state (red) Infrared spectra computed in gas phase at B3LYP/6-31+G(d,p) and CAM-B3LYP/6-31+G(d,p) level of theory, respectively.

A.2 TCNQ:π:TMB, averaged structural parameters from S_0 and S_1 AIMD trajectories

Table A.2. Comparison of the average structural parameters of the acceptor monomer TCNQ extracted from ground and excited state trajectories. Bond lengths are reported in Å(top), bond angles and dihedrals (bottom) are reported in deg. along with Standard Deviation, SD.

Bonds (Å)	I trajectory (S_0) Mean (Å) (SD)	I trajectory (S_1) Mean (Å) (SD)	Δ (S_1 - S_0)	II trajectory (S_1) Mean (Å) (SD)	Δ (S_1 - S_0)	III trajectory (S_1) Mean (Å) (SD)	Δ (S_1 - S_0)
C3 - C10	1.393 (0.02)	1.421 (0.02)	0.028	1.417 (0.02)	0.024	1.418 (0.02)	0.025
C10 - C11	1.428 (0.02)	1.417 (0.02)	-0.011	1.417 (0.01)	-0.011	1.416 (0.02)	-0.012
C10 - C12	1.428 (0.02)	1.416 (0.02)	-0.012	1.417 (0.01)	-0.011	1.416 (0.02)	-0.012
C11 - N1	1.165 (0.008)	1.163 (0.008)	-0.002	1.162 (0.005)	-0.003	1.163 (0.008)	-0.002
C12 - N2	1.165 (0.01)	1.163 (0.007)	-0.002	1.162 (0.005)	-0.003	1.163 (0.007)	-0.002
C3 - C4	1.449 (0.02)	1.425 (0.02)	-0.024	1.427 (0.02)	-0.022	1.429 (0.02)	-0.02
C4 - C5	1.357 (0.01)	1.368 (0.01)	0.011	1.360 (0.01)	0.003	1.368 (0.01)	0.011
C2 - C3	1.449 (0.02)	1.425 (0.02)	-0.024	1.426 (0.02)	-0.023	1.425 (0.02)	-0.024
C6 - C7	1.391 (0.02)	1.420 (0.02)	0.029	1.421 (0.02)	0.03	1.420 (0.02)	0.029
C7 - C8	1.429 (0.02)	1.417 (0.02)	-0.012	1.416 (0.02)	-0.013	1.417 (0.02)	-0.012
C7 - C9	1.428 (0.02)	1.417 (0.02)	-0.011	1.415 (0.02)	-0.013	1.417 (0.02)	-0.011
C8 - N3	1.165 (0.01)	1.163 (0.009)	-0.002	1.163 (0.008)	-0.002	1.163 (0.01)	-0.002
C9 - N4	1.165 (0.01)	1.163 (0.008)	-0.002	1.163 (0.007)	-0.002	1.163 (0.01)	-0.002
C5 - C6	1.449 (0.02)	1.425 (0.01)	-0.024	1.425 (0.02)	-0.024	1.426 (0.02)	-0.023
C6 - C1	1.449 (0.02)	1.425 (0.01)	-0,024	1.424 (0.02)	-0.024	1.426 (0.02)	-0.023
C1 - C2	1.357 (0.01)	1.368 (0.01)	0.011	1.360 (0.01)	0.003	1.368 (0.01)	0.011
Bond Angles (deg.)							
C2 - C3 - C4	117.6 (2.1)	116.6 (2.3)	-0.9	116.7 (2.1)	-0.9	116.8 (2.6)	-0.8
C3 - C4 - C5	120.8 (2.4)	121.3 (2.2)	0.5	121.2 (2.1)	0.4	121.3 (2.1)	0.5
C4 - C5 - C6	120.9 (21.)	121.2 (2.2)	0.3	121.2 (2.1)	0.3	121.3 (2.1)	0.4
C5 - C6 - C1	117.6 (2.1)	116.6 (2.3)	-1	116.7 (2.1)	-0.95	116.8 (2.6)	-0.8
C6 - C1 - C2	120.9 (2.4)	121.3 (2.2)	0.4	121.3 (2.1)	0.4	121.3 (2.2)	0.4
C1 - C2 - C3	120.9 (2.1)	121.3 (2.1)	0.4	121.2 (2.0)	0.3	121.3 (2.2)	0.4
N1 – C10 - N2	117.2 (7.3)	119.4 (6.8)	2.9	119.6 (6.4)	2.3	117.7 (6.1)	0.5
N3 – C7 - N4	116.5 (7.5)	119.8 (6.1)	2.6	118.9 (5.7)	2.4	118.5(6.0)	2
Dihedrals (deg.)							
N1 – C10 – C7 – N4	-181.3 (10.4)	-163.8 (18.6)	17.5	-162.9 (13.7)	13.4	-167.1 (16.4)	14.2
N2 – C10 – C7 – N3	-178.9 (14.1)	-194.2 (16.4)	-15.3	-197.6 (14.1)	-18.7	-193.7 (16.8)	-14.8
N1 – C10 – C3 – C2	-178.6 (7.9)	-173.9 (13.1)	4.7	-174.8 (9.5)	3.8	-174.9 (11.03)	3.7

Table A.3. Comparison of the average structural parameters of the donor monomer TMB extracted from ground and excited state trajectories. Bond lengths are reported in Å(top), bond angles (bottom) are reported in deg. along with Standard Deviation, SD.

Bonds (Å)	I trajectory (S_0) Mean (Å) (SD)	I trajectory (S_1) Mean (Å) (SD)	Δ (S_1 - S_0)	II trajectory (S_1) Mean (Å) (SD)	Δ (S_1 - S_0)	III trajectory (S_1) Mean (Å) (SD)	Δ (S_1 - S_0)
C1 - C2	1.410 (0.02)	1.452 (0.02)	0.04	1.457 (0.02)	0.047	1.456 (0.02)	0.046
C2 - C3	1.403 (0.02)	1.390 (0.02)	-0.01	1.387 (0.02)	-0.016	1.389 (0.02)	-0.014
C3 - C4	1.401 (0.02)	1.381 (0.02)	-0.02	1.390 (0.02)	-0.011	1.389 (0.02)	-0.012
C4 - C5	1.410 (0.02)	1.452 (0.02)	0.04	1.456 (0.02)	0.04	1.455 (0.02)	0.045
C5 - C6	1.402 (0.02)	1.390 (0.02)	-0.01	1.391 (0.02)	-0.01	1.388 (0.02)	-0.014
C6 - C1	1.402 (0.02)	1.382 (0.02)	-0.02	1.387 (0.02)	-0.015	1.390 (0.02)	-0.012
C1 - C7	1.510 (0.003)	1.490 (0.02)	-0.02	1.491 (0.02)	-0.019	1.491 (0.02)	-0.019
C2 - C8	1.512 (0.003)	1.491 (0.02)	-0.021	1.492 (0.02)	-0.02	1.492 (0.02)	-0.02
C5 - C10	1.508 (0.003)	1.490 (0.02)	-0.018	1.491 (0.02)	-0.017	1.492 (0.02)	-0.016
C4 - C9	1.512 (0.003)	1.493 (0.02)	-0.019	1.491 (0.02)	-0.021	1.491 (0.02)	-0.021
Bond Angles(deg.)							
C2 - C3 - C4	118.3 (2.7)	121.9 (2.1)	3.5	122.08 (2.2)	3.8	121.9 (2.1)	3.5
C3 - C4 - C5	122.8 (2.1)	118.6 (2.1)	-4.2	118.7 (2.1)	-4.1	118.7 (2.1)	-4.1
C4 - C5 - C6	118.2 (2.7)	118.6 (2.1)	0.4	118.6 (2.1)	0.4	118.6 (2.1)	0.4
C5 - C6 - C1	118.3 (2.7)	121.9 (2.1)	3.6	122.09 (2.2)	3.8	121.9 (2.1)	3.6
C6 - C1 - C2	122.8 (2.1)	118.5 (2.1)	-4.3	118.7 (2.1)	-3.8	118.6 (2.1)	-4.2
C1 - C2 - C3	118.2 (2.7)	118.7 (2.1)	0.5	118.6 (2.1)	0.4	118.5 (2.1)	0.3

A.2.1 TCNQ:π:TMB, center of mass distance from S_0 and S_1 AIMD trajectories

We have computed the distance between the centers of mass of the two monomers for each trajectory sampled: for the 10 ps long ground state one, the two monomers are at an average distance of 3,993 Å reaching the maximum distance of 4,522 Å at $\simeq$ 3,5 ps. The closest point of contact occurs 1.5 ps (3.336 Å). Two excited state trajectories showed similar behavior (**S1 I** and **S1 II**) on average the distance between the two subunits is of 3.810 Å and 3.765 Å , respectively. Due to the new electron distribution following the photoexcitation and the formation of a biradical species, the CT complex is able to reach a minimum distance of $\simeq$ 0.4 Å below that observed for the ground state. The last excited state trajectory (**S1 III**) shows a visibly different trend with maximums just above 6.000 Å for the first 3 ps, to then decrease up to 2.980 Å (minimum distance) and then increase again around 5.00 Å . The discordant trend was verified by analyzing the S1 III trajectory frames, at distances close to 6.000 Å the TCNQ monomer arranges itself slipped parallel with respect to the TMB by superimposing only one region of the molecule (NC-CCN) on the TMB ring. For this reason the distance between the centers of mass assumes values so different from that observed for the other trajectories.

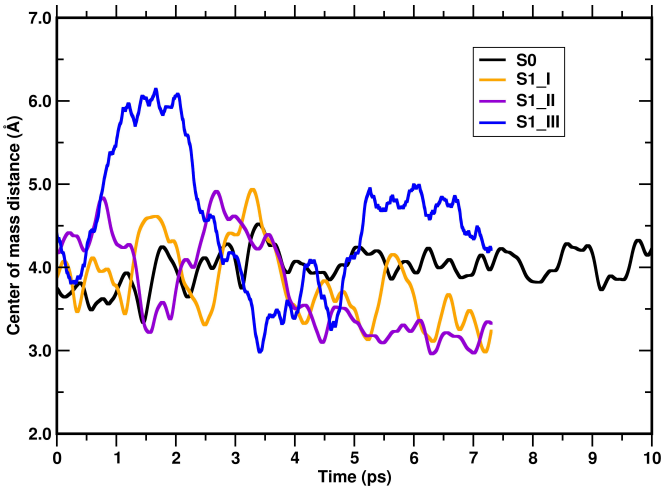

Figure A.4. Center of mass distances, in Å, computed from ground and excited state trajectories (labels and color scheme are inside the figure).

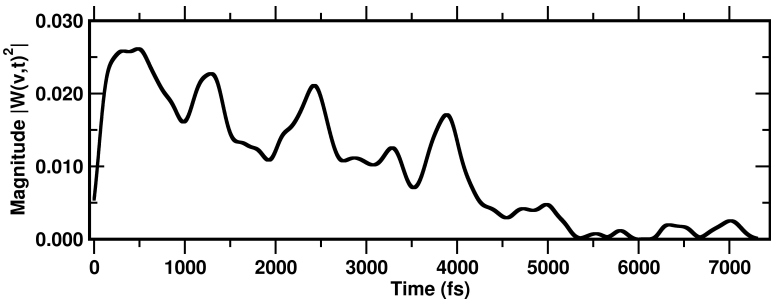

Figure A.5. Magnitude $|W(v,t)^2|$ of the CCN bending mode extracted from the excited state Wavelet spectrum reported at the bottom of 2.13.

A.3 DimethoxyASI, preliminary computational study

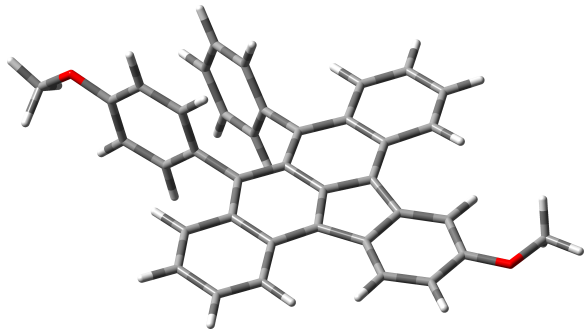

Figure A.6. Ground state optimized structure at B3LYP/6-31G(d,p) potential, of the isolated *DimethoxyASI* monomer as reference for the restricted and unrestricted TDDFT benchmark calculations.

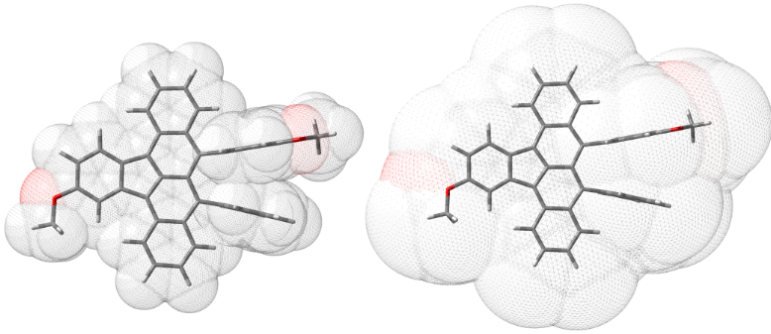

Figure A.7. Implicit solvation cavities van der Waals (VDW, α=1.1) and Solvent Accessible Surface (SAS, α=1.0) from left to right, respectively, evaluated in the restricted and unrestricted TDDFT benchmark.

The restricted TDDFT benchmark was performed on the isolated monomer optimized in ground state at B3LYP/6-31G(d,p) theory level, reported above in (A.6). We can summarize here the implicit solvation effect of DCM and the inclusion of diffuse functions on heavy and on hydrogen atoms. The differences reported in Chapter 4 are to be considered the maximum difference between the ten excited states calculated.

Table A.4. Restricted B3LYP TDDFT benchmark calculations performed on the optimized structure of *DimethoxyASI* monomer in gas phase at B3LYP/6-31G(d,p) theory level to evaluate the effect of the diffuse functions and implicit solvation models (DCM) on the vertical excitation energies (eV). The oscillator strength for each singlet excited states is reported in parenthesis.

eV (f)	**B3LYP/6-31G(d,p)**			**B3LYP/6-31+G(d,p)**			**B3LYP/6-31++G(d,p)**		
	GAS	VDW	SAS	GAS	VDW	SAS	GAS	VDW	SAS
ES1	2.0692(0.1234)	2.0429(0.2065)	2.0663(0.1511)	2.0407(0.1250)	2.0158(0.2105)	2.0377(0.1542)	2.0406(0.1249)	2.0158(0.2103)	2.0377(0.1542)
ES2	2.2625(0.0636)	2.2589(0.0529)	2.2614(0.0631)	2.2363(0.0592)	2.2384(0.0481)	2.2363(0.0587)	2.2365(0.0592)	2.2385(0.0482)	2.2364(0.0588)
ES3	2.7076(0.0004)	2.6018(0.0004)	2.6633(0.0004)	2.6855(0.0004)	2.5892(0.0005)	2.6402(0.0004)	2.6857(0.0004)	2.5896(0.0005)	2.6405(0.0004)
ES4	3.3122(0.0420)	3.3029(0.0876)	3.3096(0.0546)	3.2696(0.0335)	3.2632(0.0781)	3.2677(0.0456)	3.2696(0.0335)	3.2633(0.0780)	3.2678(0.0455)
ES5	3.4150(0.0090)	3.4015(0.0101)	3.4172(0.0099)	3.3879(0.0087)	3.3791(0.0074)	3.3905(0.0094)	3.3878(0.0087)	3.3791(0.0076)	3.3904(0.0094)
ES6	3.5443(0.0007)	3.4310(0.0036)	3.5017(0.0010)	3.5137(0.0012)	3.4095(0.0051)	3.4711(0.0015)	3.5141(0.0012)	3.4100(0.0050)	3.4716(0.0015)
ES7	3.6684(0.0003)	3.5631(0.0032)	3.6336(0.0028)	3.6099(0.0114)	3.5490(0.0061)	3.6115(0.0136)	3.6097(0.0115)	3.5498(0.0062)	3.6113(0.0162)
ES8	3.6902(0.0118)	3.6825(0.0154)	3.6841(0.0107)	3.6547(0.0126)	3.6079(0.0548)	3.6134(0.0162)	3.6550(0.0126)	3.6077(0.0545)	3.6139(0.0136)
ES9	3.7619(0.0369)	3.7263(0.0909)	3.7531(0.0543)	3.7068(0.0089)	3.6802(0.0394)	3.6974(0.0221)	3.7069(0.0088)	3.6802(0.0394)	3.6975(0.0219)
ES10	3.9717(0.0884)	3.8886(0.0018)	3.9460(0.0258)	3.8648(0.1614)	3.8630(0.1578)	3.8793(0.2544)	3.8643(0.1588)	3.8631(0.1621)	3.8791(0.2547)

Table A.5. Restricted CAM-B3LYP TDDFT benchmark calculations performed on the optimized structure of *DimethoxyASI* monomer in gas phase at B3LYP/6-31G(d,p) theory level to evaluate the effect of the diffuse functions and implicit solvation models (DCM) on the vertical excitation energies (eV). The oscillator strength for each singlet excited states is reported in parenthesis.

eV (f)	**CAM-B3LYP/6-31G(d,p)**			**CAM-B3LYP/6-31+G(d,p)**			**CAM-B3LYP/6-31++G(d,p)**		
	GAS	VDW	SAS	GAS	VDW	SAS	GAS	VDW	SAS
ES1	2.4135(0.2534)	2.3537(0.3544)	2.4007(0.2928)	2.3743(0.2506)	2.3153(0.3524)	2.3611(0.2914)	2.3742(0.2505)	2.3153(0.3523)	2.3611(0.2913)
ES2	2.6701(0.0324)	2.6860(0.0285)	2.6754(0.0312)	2.6442(0.0294)	2.6647(0.0272)	2.6505(0.0289)	2.6443(0.0294)	2.6646(0.0272)	2.6505(0.0289)
ES3	3.5304(0.0677)	3.4892(0.0764)	3.5200(0.0770)	3.4885(0.0600)	3.4547(0.0852)	3.4789(0.0718)	3.4885(0.0601)	3.4548(0.0855)	3.4789(0.0718)
ES4	3.6597(0.0066)	3.5779(0.0677)	3.6219(0.0176)	3.6259(0.0043)	3.5470(0.0493)	3.5867(0.0128)	3.6261(0.0043)	3.5472(0.0489)	3.5870(0.0127)
ES5	4.1283(0.0343)	4.0955(0.0893)	4.1279(0.0503)	4.0645(0.0495)	4.0299(0.1354)	4.0617(0.0743)	4.0643(0.0494)	4.0297(0.1351)	4.0615(0.0741)
ES6	4.3377(0.0765)	4.3203(0.2065)	4.3357(0.1065)	4.2450(0.0363)	4.2425(0.1270)	4.2450(0.0474)	4.2448(0.0364)	4.2423(0.1270)	4.2449(0.0475)
ES7	4.3673(0.0385)	4.3588(0.0495)	4.3650(0.0439)	4.2995(0.0570)	4.2858(0.1380)	4.2962(0.0820)	4.2993(0.0571)	4.2856(0.1381)	4.2960(0.0820)
ES8	4.6131(0.0066)	4.4864(0.0207)	4.5663(0.0082)	4.5567(1.0246)	4.4267(1.5978)	4.5175(1.2266)	4.5563(1.0239)	4.4265(1.6033)	4.5174(1.2769)
ES9	4.6581(0.2028)	4.5423(0.4643)	4.6178(0.1716)	4.5681(0.0437)	4.4497(0.0615)	4.5212(0.1303)	4.5685(0.0435)	4.4503(0.0549)	4.5217(0.0796)
ES10	4.7062(0.9123)	4.5614(1.2688)	4.6642(1.3047)	4.6197(0.0099)	4.5151(0.0702)	4.5877(0.1606)	4.6191(0.0122)	4.5157(0.0699)	4.5881(0.1582)

Table A.6. Unrestricted UB3LYP TDDFT benchmark calculations performed on the optimized structure of *DimethoxyASI* monomer in gas phase at B3LYP/6-31G(d,p) theory level to evaluate the effect of the diffuse functions and implicit solvation models (DCM) on the vertical excitation energies (eV). For singlet excited states the oscillator strength is reported in parenthesis.

eV (f)	**UB3LYP/6-31G(d,p)**			**UB3LYP/6-31+G(d,p)**			**UB3LYP/6-31++G(d,p)**		
	GAS	VDW	SAS	GAS	VDW	SAS	GAS	VDW	SAS
ES1	0.9372	0.9462	0.9402	0.9423	0.9526	0.9457	0.9424	0.9527	0.9458
ES2	1.6775	1.7013	1.6843	1.6707	1.6982	1.6782	1.6708	1.6982	1.6783
ES3	2.0692 (0.1233)	2.0429 (0.2063)	2.0663 (0.1510)	2.0407 (0.1248)	2.0158 (0.2103)	2.0377 (0.1541)	2.0406 (0.1248)	2.0158 (0.2102)	2.0377 (0.1540)
ES4	2.2625 (0.0635)	2.2589 (0.0528)	2.2614 (0.0630)	2.2363 (0.0591)	2.2384 (0.0481)	2.2363 (0.0586)	2.2365 (0.0591)	2.2385 (0.0482)	2.2364 (0.0586)
ES5	2.6727	2.5798	2.6367	2.6529	2.5672	2.6147	2.6530	2.5676	2.6150
ES6	2.7076 (0.0003)	2.6018 (0.0004)	2.6633 (0.0004)	2.6855 (0.0004)	2.5892 (0.0005)	2.6402 (0.0004)	2.6857 (0.0004)	2.5897 (0.0005)	2.6405 (0.0004)
ES7	2.7305	2.7285	2.7266	2.7152	2.7198	2.7128	2.7152	2.7198	2.7129
ES8	2.9209	2.9223	2.9200	2.9059	2.9082	2.9050	2.9059	2.9082	2.9050
ES9	3.1604	3.1662	3.1636	3.1407	3.1482	3.1437	3.1406	3.1482	3.1436
ES10	3.2480	3.2510	3.2485	3.1988	3.2045	3.1996	3.1987	3.2044	3.1995

Table A.7. Unrestricted UCAM-B3LYP TDDFT benchmark calculations performed on the optimized structure of *DimethoxyASI* monomer in gas phase at B3LYP/6-31G(d,p) theory level to evaluate the effect of the diffuse functions and implicit solvation models (DCM) on the vertical excitation energies (eV). For singlet excited states the oscillator strength is reported in parenthesis.

eV (f)	**UCAM-B3LYP/6-31G(d,p)**			**UCAM-B3LYP/6-31+G(d,p)**			**UCAM-B3LYP/6-31++G(d,p)**		
	GAS	VDW	SAS	GAS	VDW	SAS	GAS	VDW	SAS
ES1	0.3837	0.4254	0.3954	0.4351	0.4744	0.4463	0.4353	0.4747	0.4466
ES2	1.7110	1.7369	1.7176	1.7142	1.7425	1.7214	1.7143	1.7426	1.7215
ES3	2.4135 (0.2539)	2.3537 (0.3549)	2.4007 (0.2932)	2.3743 (0.2501)	2.3153 (0.3519)	2.3611 (0.2908)	2.3742 (0.2501)	2.3153 (0.3519)	2.3611 (0.2908)
ES4	2.6701 (0.0324)	2.6860 (0.0285)	2.6754 (0.0312)	2.6442 (0.0293)	2.6647 (0.0271)	2.6505 (0.0288)	2.6443 (0.0293)	2.6646 (0.0272)	2.6505 (0.0288)
ES5	2.8249	2.8449	2.8294	2.8155	2.8384	2.8204	2.8155	2.8384	2.8204
ES6	3.0517	3.0566	3.0517	3.0359	3.0409	3.0358	3.0359	3.0409	3.0358
ES7	3.2555	3.2640	3.2568	3.2393	3.2494	3.2407	3.2392	3.2493	3.2407
ES8	3.3592	3.3643	3.3587	3.3332	3.3398	3.3329	3.3327	3.3394	3.3324
ES9	3.4802	3.4888	3.4803	3.4688	3.4547 (0.0849)	3.4691	3.4684	3.4548 (0.0856)	3.4687
ES10	3.5304 (0.0681)	3.4892 (0.0765)	3.5200 (0.0768)	3.4886 (0.0597)	3.4787	3.4789 (0.0714)	3.4885 (0.0603)	3.4783	3.4789 (0.0720)

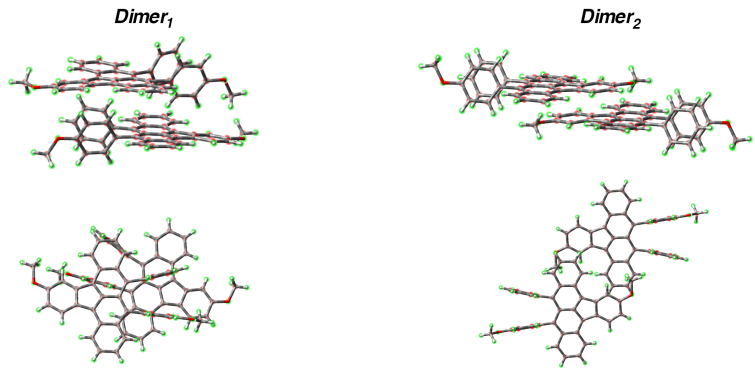

Figure A.8. Constrained optimization in gas phase performed at B3LYP/6-31+G(d,p) level. The coordinates of the atoms highlighted in red are fixed during the optimization, all the hydrogens atoms marked in green are free.

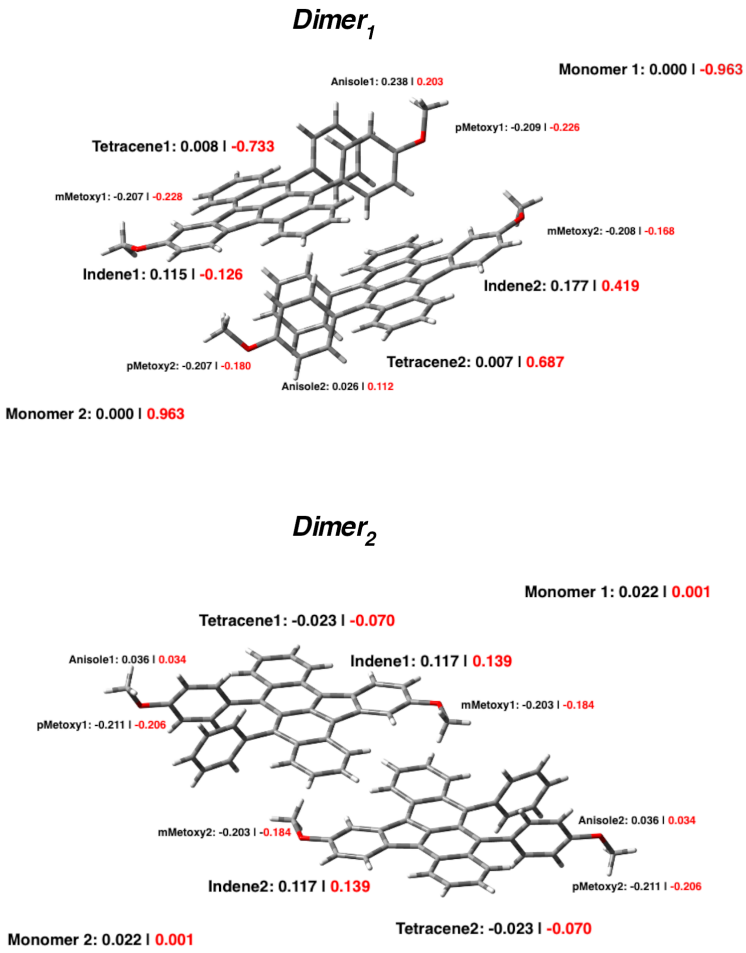

Figure A.9. NBO charge fragments analysis of $Dimer_1$ and $Dimer_2$ structures in ground (black) and first singlet excited state (red) performed at B3LYP/6-31+G(d,p) and TD-B3LYP/6-31+G(d,p) level, respectively. The convenient nomenclature shown in the figure recalls the type of fragments chosen: mMethoxy indicates the Methoxy group in meta position on the Indene, Anisole is the phenyl substitute that brings the O-CH_3 group to the para position (pMethoxy) and Tetracene states for the four ring-fused backbone.

A.4 DimethoxyASI, experimental methods and technical specifications

The absorption spectrum of *DimethoxyASI* crystals has been recorded using UV-Vis spectrophotometer by Shimadzu in transmission mode.

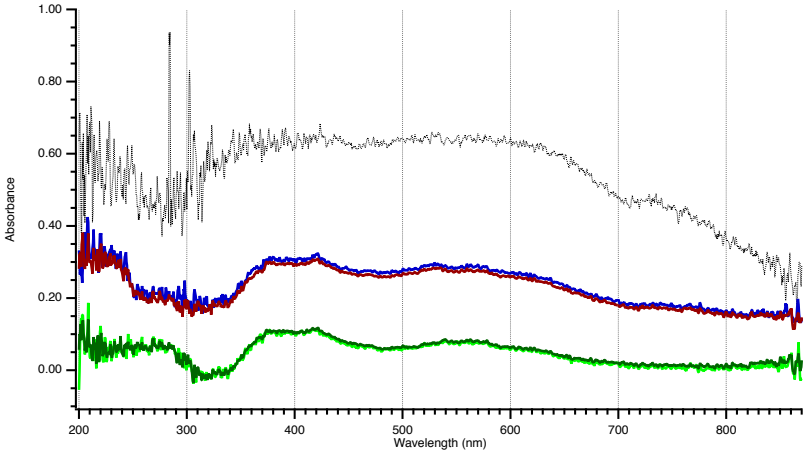

Figure A.10. UV-Vis absorption spectrum recorded in the 200:870 nm range. The black dot trace is the spectrum recorded as first exploratory step. The blue trace is for medium speed acquisiton velocity, red trace is for very slow acquisition velocity on the Big spot. The green trace is for medium speed acquisition velocity, the light green is for very slow acquisition velocity on the Small spot.

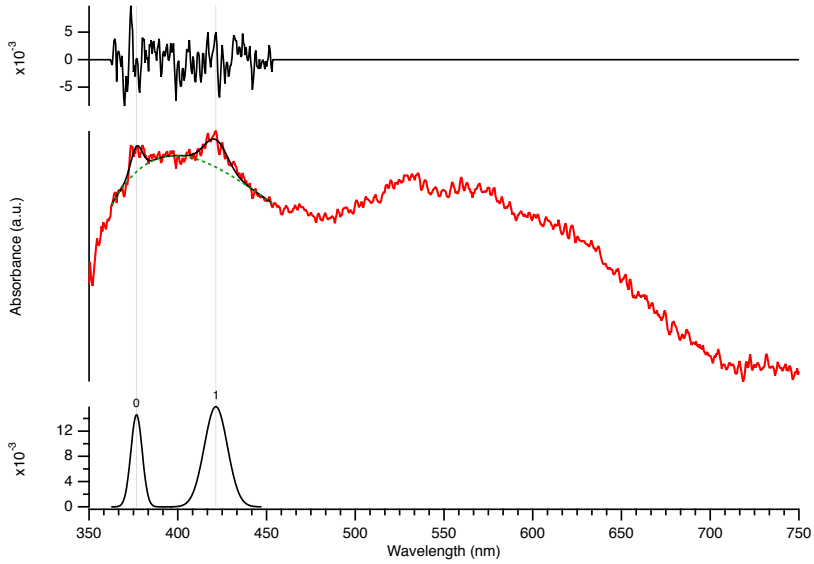

Figure A.11. Gaussian curve fitting in the 350 - 450 nm region performed on the very slow acquisition velocity on the Big spot. At the top is reported the difference between the fitting and the UV-Vis spectrum (solid black - solid red). At the bottom two main gaussian peaks are reported as difference between the fitting and baseline (solid black - dashed green).

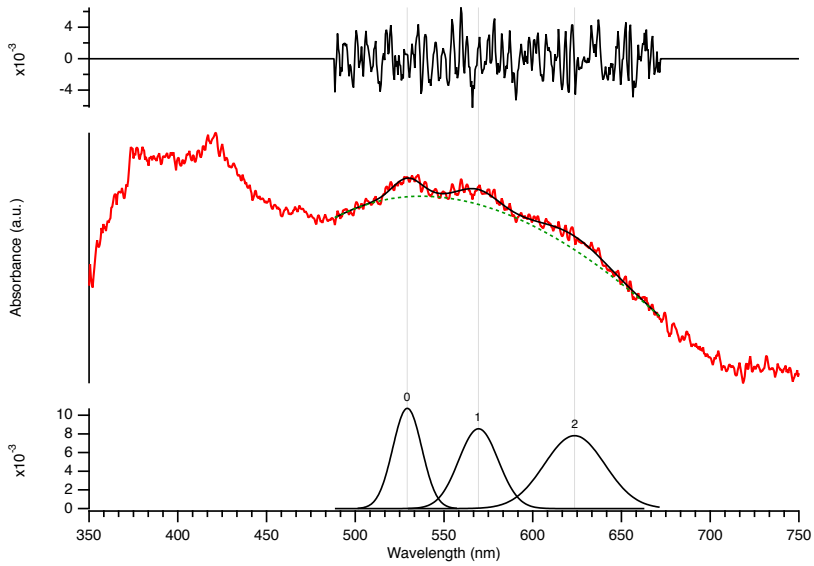

Figure A.12. Gaussian curve fitting in the 500 - 650 nm region performed on the very slow acquisition velocity on the Big spot. At the top is reported the difference between the fitting and the UV-Vis spectrum (solid black - solid red). At the bottom three main gaussian peaks are reported as difference between the fitting and baseline (solid black - dashed green).

Spontaneous Raman spectrum (Continous Wave, CW) of *DimethoxiASI* crystals has been collected using a home-built Raman spectrometer, see A.13. We passed a 785 nm laser through a 30:70 beam splitter and focused onto the sample through a 10x Olympus objective lens. The power of the laser at the sample was 80 mW. The Raman signal has been collected using a Princeton Instruments 2500i spectrograph and a Princeton Instruments PIXIS 100BX CCD array.

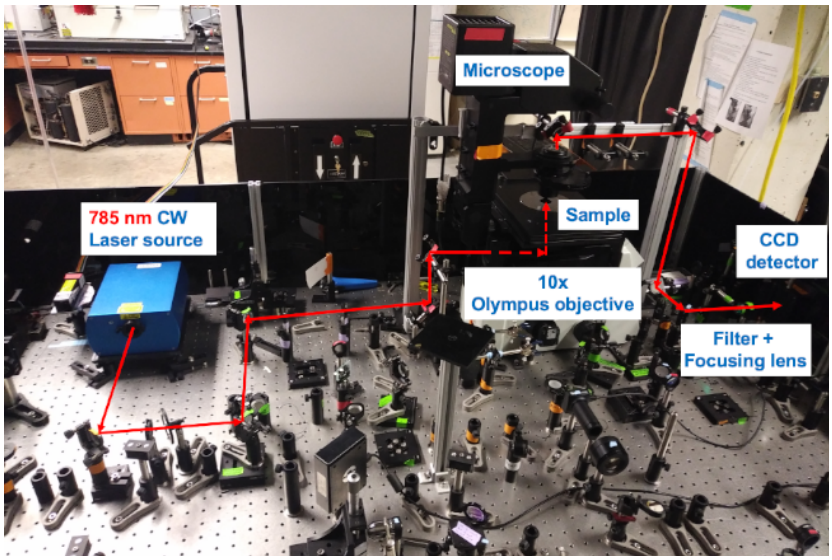

Figure A.13. Experimental apparatus. Photograph of the optics table of a CW Raman system in operation.

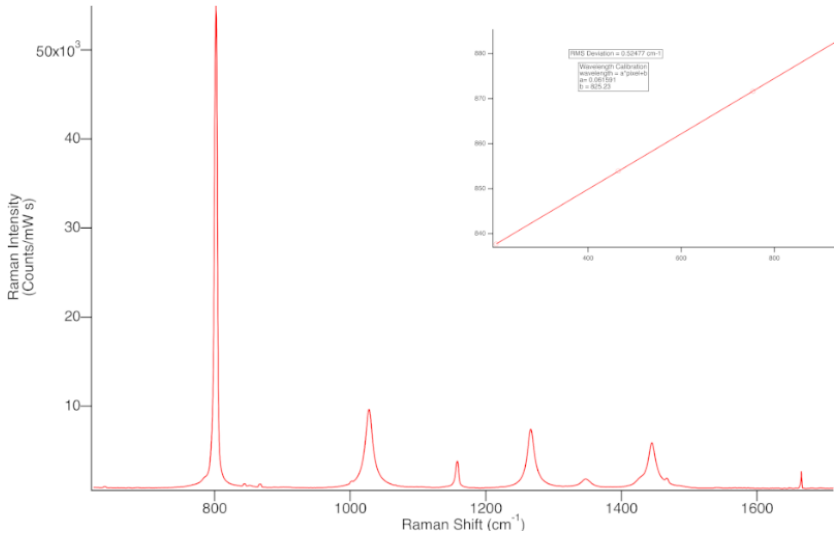

Figure A.14. Calibration of the Raman spectrometer by recording the cyclohexane spectrum at RT. Main peaks are located at 801.3 cm^{-1} - CC stretching, 1028.3 cm^{-1} - CH_2 rocking, 1266.4 cm^{-1} - CH_2 wagging and 1444.4 cm^{-1} - CH_2 scissoring.

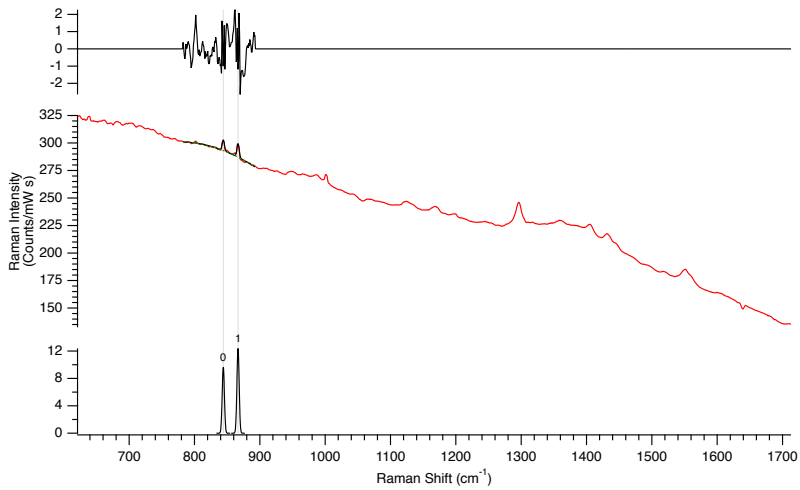

Figure A.15. Gaussian curve fitting in the 800 - 900 cm^{-1} region of the spontaneous Raman spectrum. At the top is reported the difference between the fitting and the Raman spectrum (solid black - solid red). At the bottom two main gaussian peaks (at 844.03, 866.62 cm^{-1}) are reported as difference between the fitting and baseline (solid black - dashed green).

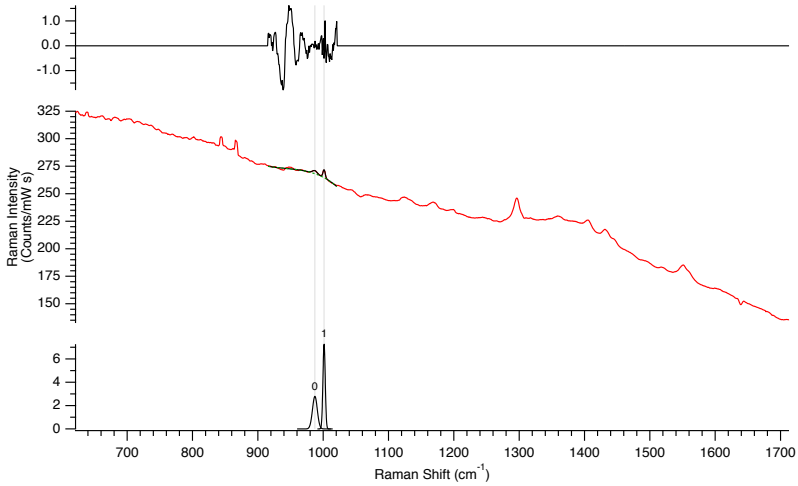

Figure A.16. Gaussian curve fitting in the 900 - 1000 cm^{-1} region of the spontaneous Raman spectrum. At the top is reported the difference between the fitting and the Raman spectrum (solid black - solid red). At the bottom two main gaussian peaks (at 987.27, 1001.4 cm^{-1}) are reported as difference between the fitting and baseline (solid black - dashed green).

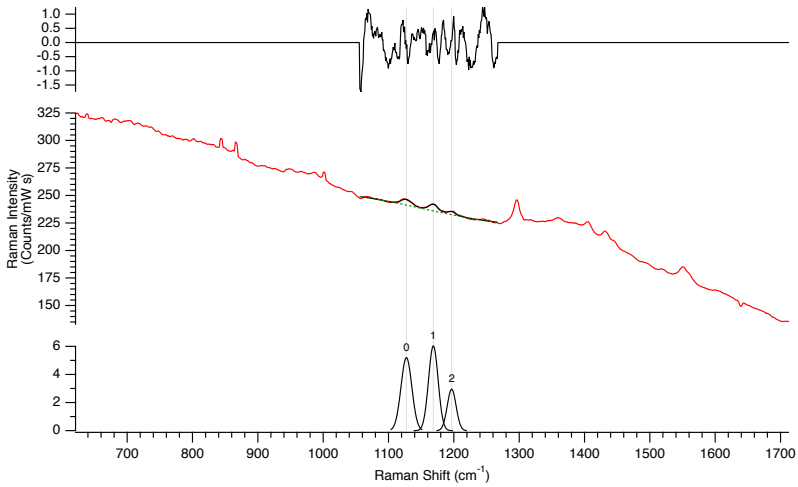

Figure A.17. Gaussian curve fitting in the 1100 - 1200 cm^{-1} region of the spontaneous Raman spectrum. At the top is reported the difference between the fitting and the Raman spectrum (solid black - solid red). At the bottom three main gaussian peaks (at 1127.4, 1168.6, 1196.6 cm^{-1}) are reported as difference between the fitting and baseline (solid black - dashed green).

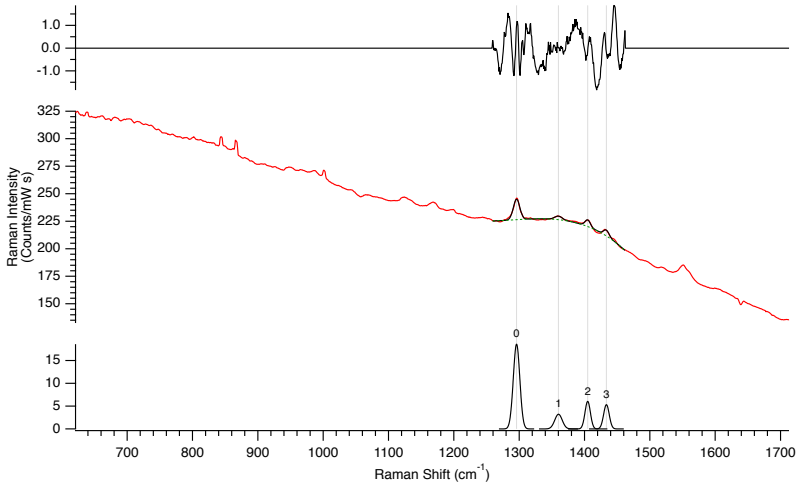

Figure A.18. Gaussian curve fitting in the 1300 - 1450 cm^{-1} region of the spontaneous Raman spectrum. At the top is reported the difference between the fitting and the Raman spectrum (solid black - solid red). At the bottom four main gaussian peaks (at 1295.9, 1360.1, 1404.8, 1433.5 cm^{-1}) are reported as difference between the fitting and baseline (solid black - dashed green).

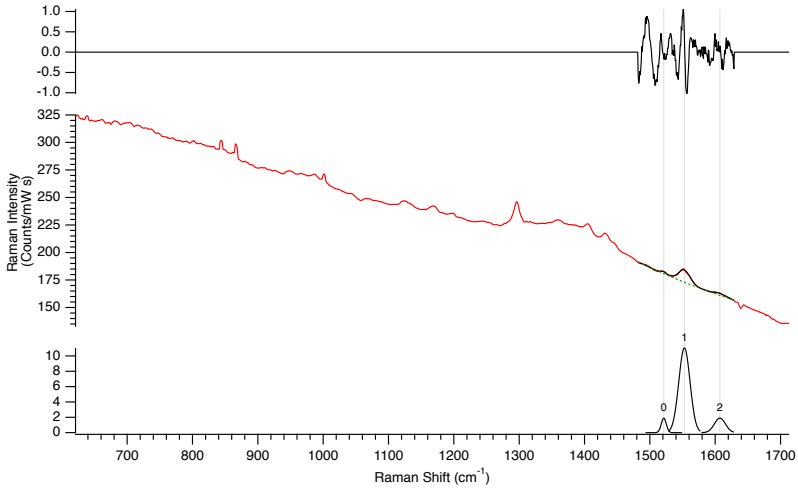

Figure A.19. Gaussian curve fitting in the 1500 - 1600 cm^{-1} region of the spontaneous Raman spectrum. At the top is reported the difference between the fitting and the Raman spectrum (solid black - solid red). At the bottom three main gaussian peaks (at 1521.3, 1552.8, 1607.2 cm^{-1}) are reported as difference between the fitting and baseline (solid black - dashed green).

We collected Femtosecond Stimulated Raman Spectra on a home-built setup which employed Coherent model Libra-F-1K-HE-110 femtosecond amplifier, showed in A.20.

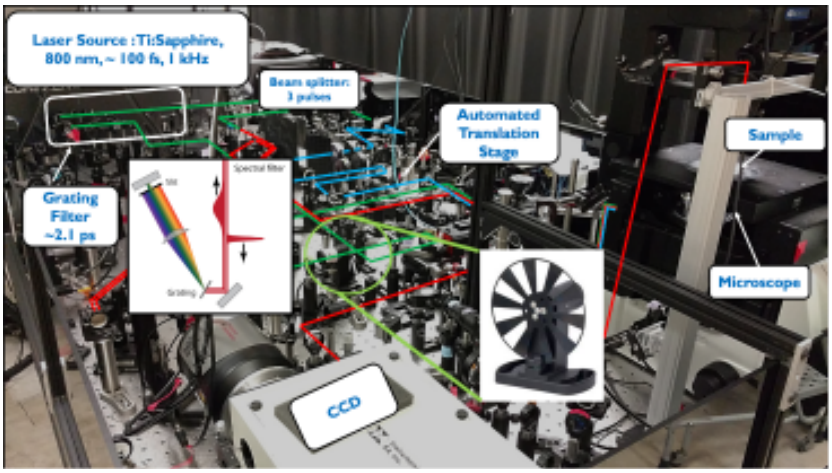

Figure A.20. Experimental apparatus. Photograph of the optics table of a FSRS system in operation.

The ultrafast Ti:Sapphire laser (4.6 W fundamental output at 800 nm) has been used to create the three laser pulses required for the experiment:

- 480 mW of the fundamental output generated a 2.1 ps narrowband Raman pump pulse through a home-built grating filter (see A.21).
- the broadband continuum fs-Raman probe has been obtained by passing a 2.5 mW of the fundamental output through a sapphire crystal (2 mm thick) and a longpass filter (RG830) to be then compressed with a fused silica prism compressor.
- the actinic pump has been generated through an in-house built non-collinear parametric amplifier (NOPA).

  The actinic pump was tuned to a central wavelength of 587 nm and a FWHM of 26 nm with a Gaussian spectral shape. A.21

The three pulses have been sent through an Olympus IX 73 microscope focused non collinearly onto the sample with a 35 mm focal length lens. A piezoelectric translation stage allowed to vary the time delay between the actinic pump and Raman pump-probe pair. The cross-correlation of actinic

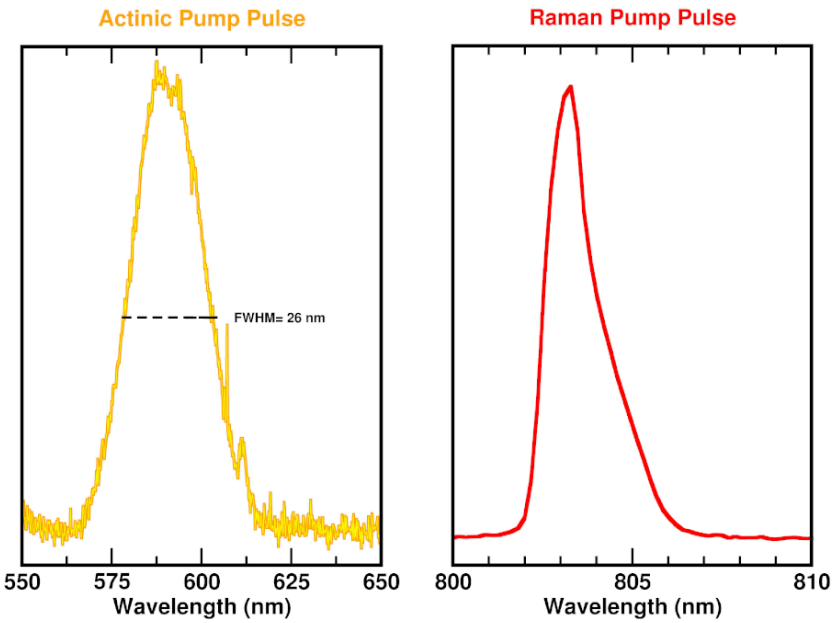

Figure A.21. Left panel: Actinic pump pulse (587 nm, FWHM: 26 nm, 264 fs time resolution). Right panel: Raman pump pulse (803 nm, 2.1 ps)

pump and Raman probe was 244 fs $\pm$ 2 as measured by the optical Kerr effect of cyclohexane (2 mm cuvette). The Princeton Instruments PIXIS 110F CCD array collected the spectra at kHz repetition rate. A modified version of Labview software has been used to visualize raw FSR data during the measurements, we collected each spectrum for 20-90 seconds and obtained the Raman gain by dividing the Raman pump-on spectrum by the Raman pump-off spectrum.

List of Figures

List of Tables

Bibliography

[1] E. Ippen and C. Shank, "Dynamic spectroscopy and subpicosecond pulse compression," *Appl. Phys. Lett.*, vol. 27, no. 9, pp. 488–490, 1975.

[2] M. J. Colles and C. Pidgeon, "Tunable lasers," *Rep. Prog. Phys.*, vol. 38, no. 3, p. 329, 1975.

[3] J. Heritage and R. Jain, "Subpicosecond pulses from a tunable CW mode-locked dye laser," *Appl. Phys. Lett.*, vol. 32, no. 2, pp. 101–103, 1978.

[4] A. H. Zewail, "Femtochemistry. past, present, and future," *Pure Appl. Chem.*, vol. 72, no. 12, pp. 2219–2231, 2000.

[5] A. H. Zewail, "Femtochemistry: atomic-scale dynamics of the chemical bond using ultrafast lasers (Nobel Lecture)," *Angew. Chem. Int. Ed.*, vol. 39, no. 15, pp. 2586–2631, 2000.

[6] A. H. Zewail, "Femtochemistry: atomic-scale dynamics of the chemical bond," *J. Phys. Chem. A*, vol. 104, no. 24, pp. 5660–5694, 2000.

[7] M. Chergui, "Femtochemistry and femtobiology: the new age," *Comp. Phys. Comm.*, vol. 3, no. 8, pp. 713–718, 2002.

[8] S. Mukamel, *Principles of nonlinear optical spectroscopy*, vol. 29. Oxford university press New York, 1995.

[9] B. I. Grimberg, V. V. Lozovoy, M. Dantus, and S. Mukamel, "Ultrafast nonlinear spectroscopic techniques in the gas phase and their density matrix representation," *J. Phys. Chem. A*, vol. 106, no. 5, pp. 697–718, 2002.

[10] P. Hamm, M. Lim, and R. M. Hochstrasser, "Structure of the amide I band of peptides measured by femtosecond nonlinear-Infrared spectroscopy," *J. Phys. Chem. B*, vol. 102, no. 31, pp. 6123–6138, 1998.

[11] S. Borman, "A new dimension in spectroscopy," *Chemical & Engineering News*, vol. 78, no. 6, pp. 41–41, 2000.

[12] M. T. Zanni and R. M. Hochstrasser, "Two-dimensional Infrared spectroscopy: a promising new method for the time resolution of structures," *Curr. Opin. Struct. Biol.*, vol. 11, no. 5, pp. 516–522, 2001.

[13] N.-H. Ge, M. T. Zanni, and R. M. Hochstrasser, "Effects of vibrational frequency correlations on two-dimensional Infrared spectra," *J. Phys. Chem. A*, vol. 106, no. 6, pp. 962–972, 2002.

[14] M. T. Zanni, N.-H. Ge, Y. S. Kim, and R. M. Hochstrasser, "Two-dimensional IR spectroscopy can be designed to eliminate the diagonal peaks and expose only the crosspeaks needed for structure determination," *Proc. Natl. Acad. Sci. U.S.A.*, vol. 98, no. 20, pp. 11265–11270, 2001.

[15] L. J. Kaufman, J. Heo, G. R. Fleming, J. Sung, and M. Cho, "Fifth-order electronically non-resonant Raman scattering: two-dimensional Fourier deconvolution," *Chem. Phys.*, vol. 266, no. 2-3, pp. 251–271, 2001.

[16] P. Hamm and R. M. Hochstrasser, "Structure and dynamics of proteins and peptides: femtosecond two-dimensional Infrared spectroscopy," in *Ultrafast Infrared and Raman Spectroscopy*, pp. 285–359, CRC Press, 2001.

[17] A. Tokmakoff, M. Lang, D. Larsen, G. Fleming, V. Chernyak, and S. Mukamel, "Two-dimensional Raman spectroscopy of vibrational interactions in liquids," *Phys. Rev. Lett.*, vol. 79, no. 14, p. 2702, 1997.

[18] O. Golonzka, M. Khalil, N. Demirdöven, and A. Tokmakoff, "Vibrational anharmonicities revealed by coherent two-dimensional Infrared spectroscopy," *Phys. Rev. Lett.*, vol. 86, no. 10, p. 2154, 2001.

[19] A. T. Krummel and M. T. Zanni, "DNA vibrational coupling revealed with two-dimensional Infrared spectroscopy: insight into why vibrational spectroscopy is sensitive to DNA structure," *J. Phys. Chem. B*, vol. 110, no. 28, pp. 13991–14000, 2006.

[20] M. Vrakking, "Chemical physics: Electronic movies," *Nature*, vol. 460, no. 7258, p. 960, 2009.

[21] P. Emma, R. Akre, J. Arthur, R. Bionta, C. Bostedt, J. Bozek, A. Brachmann, P. Bucksbaum, R. Coffee, F.-J. Decker, *et al.*, "First lasing and operation of an ångstrom-wavelength free-electron laser," *Nat. Photonics*, vol. 4, no. 9, p. 641, 2010.

[22] G. Sciaini and R. D. Miller, "Femtosecond electron diffraction: heralding the era of atomically resolved dynamics," *Rep. Prog. Phys.*, vol. 74, no. 9, p. 096101, 2011.

[23] M. J. Vrakking, "Showtime for molecular movies," *Physics*, vol. 9, p. 112, 2016.

[24] D. Shorokhov and A. H. Zewail, "Perspective: 4D ultrafast electron microscopy—evolutions and revolutions," *J. Chem. Phys.*, vol. 144, no. 8, p. 080901, 2016.

[25] R. Schoenlein, L. Peteanu, R. Mathies, and C. Shank, "The first step in vision: femtosecond isomerization of rhodopsin," *Science*, vol. 254, no. 5030, pp. 412–415, 1991.

[26] B. O. Roos, "Theoretical studies of electronically excited states of molecular systems using multiconfigurational perturbation theory," *Acc. Chem. Res.*, vol. 32, no. 2, pp. 137–144, 1999.

[27] D. Polli, P. Altoè, O. Weingart, K. M. Spillane, C. Manzoni, D. Brida, G. Tomasello, G. Orlandi, P. Kukura, R. A. Mathies, *et al.*, "Conical intersection dynamics of the primary photoisomerization event in vision," *Nature*, vol. 467, no. 7314, p. 440, 2010.

[28] M. Hentschel, R. Kienberger, C. Spielmann, G. A. Reider, N. Milosevic, T. Brabec, P. Corkum, U. Heinzmann, M. Drescher, and F. Krausz, "Attosecond metrology," *Nature*, vol. 414, no. 6863, p. 509, 2001.

[29] A. L. Cavalieri, N. Müller, T. Uphues, V. S. Yakovlev, A. Baltuška, B. Horvath, B. Schmidt, L. Blümel, R. Holzwarth, S. Hendel, *et al.*, "Attosecond spectroscopy in condensed matter," *Nature*, vol. 449, no. 7165, p. 1029, 2007.

[30] L. Gallmann, C. Cirelli, and U. Keller, "Attosecond science: recent highlights and future trends," *Annu. Rev. Phys. Chem.*, vol. 63, no. 1, p. 447–469, 2012.

[31] M. Nisoli, P. Decleva, F. Calegari, A. Palacios, and F. Martin, "Attosecond electron dynamics in molecules," *Chem. Rev.*, vol. 16, no. 117, pp. 10760–10825, 2017.

[32] M. Ben-Nun, J. Quenneville, and T. J. Martínez, "Ab initio multiple spawning: photochemistry from first principles quantum molecular dynamics," *J. Phys. Chem. A*, vol. 104, no. 22, pp. 5161–5175, 2000.

[33] A. M. Virshup, C. Punwong, T. V. Pogorelov, B. A. Lindquist, C. Ko, and T. J. Martinez, "Photodynamics in complex environments: ab initio multiple spawning quantum mechanical/molecular mechanical dynamics," *J. Phys. Chem. B*, vol. 113, no. 11, pp. 3280–3291, 2008.

[34] H.-D. Meyer, F. Gatti, and G. A. Worth, *Multidimensional quantum dynamics: MCTDH theory and applications*. John Wiley & Sons, 2009.

[35] T. Yonehara, S. Takahashi, and K. Takatsuka, "Non-Born–Oppenheimer electronic and nuclear wavepacket dynamics," *J. Chem. Phys.*, vol. 130, no. 21, p. 214113, 2009.

[36] B. F. Curchod, I. Tavernelli, and U. Rothlisberger, "Trajectory-based solution of the nonadiabatic quantum dynamics equations: an on-the-fly approach for molecular dynamics simulations," *Phys. Chem. Chem. Phys.*, vol. 13, no. 8, pp. 3231–3236, 2011.

[37] J. Caillat, J. Zanghellini, M. Kitzler, O. Koch, W. Kreuzer, and A. Scrinzi, "Correlated multielectron systems in strong laser fields: a multiconfiguration time-dependent Hartree-Fock approach," *Phys. Rev. A*, vol. 71, no. 1, p. 012712, 2005.

[38] L. Wang, H.-D. Meyer, and V. May, "Femtosecond laser pulse control of multidimensional vibrational dynamics: computational studies on the pyrazine molecule," *J. Chem. Phys.*, vol. 125, no. 1, p. 014102, 2006.

[39] T. Yonehara and K. Takatsuka, "Nonadiabatic electron wavepacket dynamics of molecules in an intense optical field: an ab initio electronic state study," *J. Chem. Phys.*, vol. 128, no. 15, p. 154104, 2008.

[40] N. L. Doltsinis and D. Marx, "First principles molecular dynamics involving excited states and nonadiabatic transitions," *J. Chem. Theory Comput.*, vol. 1, no. 02, pp. 319–349, 2002.

[41] M. Baer, *Beyond Born-Oppenheimer: electronic nonadiabatic coupling terms and conical intersections*. John Wiley & Sons, 2006.

[42] E. Tapavicza, I. Tavernelli, and U. Rothlisberger, "Trajectory surface hopping within linear response time-dependent density-functional theory," *Phys. Rev. Lett.*, vol. 98, no. 2, p. 023001, 2007.

[43] R. Car and M. Parrinello, "Unified approach for molecular dynamics and density-functional theory," *Phys. Rev. Lett.*, vol. 55, no. 22, p. 2471, 1985.

[44] D. Marx and J. Hutter, *Ab initio molecular dynamics: basic theory and advanced methods*. Cambridge University Press, 2009.

[45] H. B. Schlegel, "Ab initio molecular dynamics with Born-Oppenheimer and Extended Lagrangian methods using atom centered basis functions," *Bull. Korean Chem. Soc.*, vol. 24, no. 6, pp. 837–842, 2003.

[46] A. M. Niklasson and M. J. Cawkwell, "Generalized Extended Lagrangian Born-Oppenheimer molecular dynamics," *J. Chem. Phys.*, vol. 141, no. 16, p. 164123, 2014.

[47] X. Li, J. C. Tully, H. B. Schlegel, and M. J. Frisch, "Ab initio Ehrenfest dynamics," *J. Chem. Phys.*, vol. 123, no. 8, p. 084106, 2005.

[48] W. Liang, C. M. Isborn, A. Lindsay, X. Li, S. M. Smith, and R. J. Levis, "Time-dependent density functional theory calculations of Ehrenfest dynamics of laser controlled dissociation of NO^+: pulse length and sequential multiple single-photon processes," *J. Phys. Chem. A*, vol. 114, no. 21, pp. 6201–6206, 2010.

[49] H. B. Schlegel, J. M. Millam, S. S. Iyengar, G. A. Voth, A. D. Daniels, G. E. Scuseria, and M. J. Frisch, "Ab initio molecular dynamics: propagating the density matrix with gaussian orbitals," *J. Chem. Phys.*, vol. 114, no. 22, pp. 9758–9763, 2001.

[50] H. B. Schlegel, S. S. Iyengar, X. Li, J. M. Millam, G. A. Voth, G. E. Scuseria, and M. J. Frisch, "Ab initio molecular dynamics: propagating the density matrix with gaussian orbitals. III. Comparison with Born–Oppenheimer dynamics," *J. Phys. Chem.*, vol. 117, no. 19, pp. 8694–8704, 2002.

[51] S. S. Iyengar, H. B. Schlegel, G. A. Voth, J. M. Millam, G. E. Scuseria, and M. J. Frisch, "Ab initio molecular dynamics: propagating the density matrix with gaussian orbitals. IV. Formal analysis of the deviations from Born-Oppenheimer dynamics," *Israel J. Chem.*, vol. 42, no. 2-3, pp. 191–202, 2002.

[52] N. Rega, S. S. Iyengar, G. A. Voth, H. B. Schlegel, T. Vreven, and M. J. Frisch, "Hybrid ab-initio/empirical molecular dynamics: combining the ONIOM scheme with the atom-centered density matrix propagation (ADMP) approach," *J. Phys. Chem. B*, vol. 108, no. 13, pp. 4210–4220, 2004.

[53] A. P. Scott and L. Radom, "Harmonic vibrational frequencies: an evaluation of Hartree-Fock, Møller-Plesset, quadratic configuration interaction, density functional theory, and semiempirical scale factors," *J. Phys. Chem.*, vol. 100, no. 41, pp. 16502–16513, 1996.

[54] S. Andrade, L. C. Gonçalves, and F. E. Jorge, "Scaling factors for fundamental vibrational frequencies and zero-point energies obtained from HF, MP2, and DFT/DZP and TZP harmonic frequencies," *J. Mol. Struct.*, vol. 864, no. 1-3, pp. 20–25, 2008.

[55] O. Bąk and P. Borowski, "Scaling procedures in vibrational spectroscopy," in *Molecular Spectroscopy—Experiment and Theory*, pp. 49–95, Springer, 2019.

[56] P. Carbonniere and V. Barone, "Performances of different density functionals in the computation of vibrational spectra beyond the harmonic approximation," *Chem. Phys. Lett.*, vol. 399, no. 1-3, pp. 226–229, 2004.

[57] M. Biczysko, P. Panek, G. Scalmani, J. Bloino, and V. Barone, "Harmonic and anharmonic vibrational frequency calculations with the double-hybrid B2PLYP method: analytic second derivatives and benchmark studies," *J. Chem. Theory Comput.*, vol. 6, no. 7, pp. 2115–2125, 2010.

[58] V. Barone, M. Biczysko, J. Bloino, M. Borkowska-Panek, I. Carnimeo, and P. Panek, "Toward anharmonic computations of vibrational spectra for large molecular systems," *Int. J. Quant. Chem.*, vol. 112, no. 9, pp. 2185–2200, 2012.

[59] V. Barone, M. Biczysko, and J. Bloino, "Fully anharmonic IR and Raman spectra of medium-size molecular systems: accuracy and interpretation," *Phys. Chem. Chem. Phys.*, vol. 16, no. 5, pp. 1759–1787, 2014.

[60] T. Fornaro, I. Carnimeo, and M. Biczysko, "Toward feasible and comprehensive computational protocol for simulation of the spectroscopic properties of large molecular systems: the anharmonic Infrared spectrum of uracil in the solid state by the reduced dimensionality/hybrid VPT2 approach," *J. Phys. Chem. A*, vol. 119, no. 21, pp. 5313–5326, 2014.

[61] J. Bloino, M. Biczysko, and V. Barone, "Anharmonic effects on vibrational spectra intensities: Infrared, Raman, vibrational circular dichroism, and Raman optical activity," *J. Phys. Chem. A*, vol. 119, no. 49, pp. 11862–11874, 2015.

[62] M.-P. Gaigeot and M. Sprik, "Ab initio molecular dynamics computation of the Infrared spectrum of aqueous uracil," 2003.

[63] S. Yang and M. Cho, "IR spectra of N-MethylAcetamide in water predicted by combined quantum mechanical/molecular mechanical molecular dynamics simulations," *J. Chem. Phys.*, vol. 123, no. 13, p. 134503, 2005.

[64] M. a. Gaigeot, R. Vuilleumier, M. Sprik, and D. Borgis, "Infrared spectroscopy of N-MethylAcetamide revisited by ab initio molecular dynamics simulations," *J. Chem. Theory Comput.*, vol. 1, no. 5, pp. 772–789, 2005.

[65] M.-P. Gaigeot, M. Martinez, and R. Vuilleumier, "Infrared spectroscopy in the gas and liquid phase from first principle molecular dynamics simulations: application to small peptides," *Mol. Phys.*, vol. 105, no. 19-22, pp. 2857–2878, 2007.

[66] M.-P. Gaigeot, "Theoretical spectroscopy of floppy peptides at room temperature. a DFTMD perspective: gas and aqueous phase," *Phys. Chem. Chem. Phys.*, vol. 12, no. 14, pp. 3336–3359, 2010.

[67] M. Thomas, M. Brehm, R. Fligg, P. Vöhringer, and B. Kirchner, "Computing vibrational spectra from ab initio molecular dynamics," *Phys. Chem. Chem. Phys.*, vol. 15, no. 18, pp. 6608–6622, 2013.

[68] A. Strachan, "Normal modes and frequencies from covariances in molecular dynamics or Monte Carlo simulations," *J. Chem. Phys.*, vol. 120, no. 1, pp. 1–4, 2004.

[69] M. Schmitz and P. Tavan, "Vibrational spectra from atomic fluctuations in dynamics simulations. I. Theory, limitations, and a sample application," *J. Chem. Phys.*, vol. 121, no. 24, pp. 12233–12246, 2004.

[70] M. Schmitz and P. Tavan, "Vibrational spectra from atomic fluctuations in dynamics simulations. II. Solvent-induced frequency fluctuations at femtosecond time resolution," *J. Chem. Phys.*, vol. 121, no. 24, pp. 12247–12258, 2004.

[71] M. Martinez, M.-P. Gaigeot, D. Borgis, and R. Vuilleumier, "Extracting effective normal modes from equilibrium dynamics at finite temperature," *J. Chem. Phys.*, vol. 125, no. 14, p. 144106, 2006.

[72] N. Rega, "Vibrational analysis beyond the harmonic regime from ab-initio molecular dynamics," *Theor. Chem. Acc.*, vol. 116, no. 1-3, pp. 347–354, 2006.

[73] E. Sejdić, I. Djurović, and J. Jiang, "Time–frequency feature representation using energy concentration: An overview of recent advances," *Digit. Signal Process.*, vol. 19, no. 1, pp. 153–183, 2009.

[74] G. Donati, D. B. Lingerfelt, C. M. Aikens, and X. Li, "Molecular vibration induced plasmon decay," *J. Phys. Chem. C*, vol. 121, no. 28, pp. 15368–15374, 2017.

[75] I. Daubechies, *Ten Lectures on Wavelets*, vol. 61. Siam, 1992.

[76] S. Mallat, *A Wavelet Tour of Signal Processing*. Elsevier, 1999.

[77] A. Petrone, G. Donati, P. Caruso, and N. Rega, "Understanding THz and IR signals beneath time-resolved fluorescence from excited-state ab initio dynamics," *J. Am. Chem. Soc.*, vol. 136, no. 42, pp. 14866–14874, 2014.

[78] G. Donati, A. Petrone, P. Caruso, and N. Rega, "The mechanism of a green fluorescent protein proton shuttle unveiled in the time-resolved frequency domain by excited state ab initio dynamics," *Chem. Sci.*, vol. 9, no. 5, pp. 1126–1135, 2018.

[79] M. G. Chiariello, U. Raucci, F. Coppola, and N. Rega, "Unveiling anharmonic coupling by means of excited state ab-initio dynamics: Application to diarylethene photoreactivity," *Phys. Chem. Chem. Phys.*, vol. 21, no. 21, pp. 3606–3614, 2019.

[80] G. Donati, D. B. Lingerfelt, A. Petrone, N. Rega, and X. Li, ""watching" polaron pair formation from first-principles electron–nuclear dynamics," *J. Phys. Chem. A*, vol. 120, no. 37, pp. 7255–7261, 2016.

[81] M. G. Chiariello and N. Rega, "Exploring nuclear photorelaxation of pyranine in aqueous solution: an integrated ab-initio molecular dynamics and time resolved vibrational analysis approach," *J. Phys. Chem. A*, vol. 122, no. 11, pp. 2884–2893, 2018.

[82] M. M. Martin and J. T. Hynes, *Femtochemistry and femtobiology: ultrafast events in molecular science*. Elsevier, 2004.

[83] R. R. Jones, D. C. Hooper, L. Zhang, D. Wolverson, and V. K. Valev, "Raman techniques: Fundamentals and frontiers," *Nanoscale Res. Lett.*, vol. 14, no. 1, pp. 1–34, 2019.

[84] Y.-S. Huang, T. Karashima, M. Yamamoto, T. Ogura, and H.-o. Hamaguchi, "Raman spectroscopic signature of life in a living yeast cell," *J. Raman Spectrosc.*, vol. 35, no. 7, pp. 525–526, 2004.

[85] I. B. Hutchinson, R. Ingley, H. G. Edwards, L. Harris, M. McHugh, C. Malherbe, and J. Parnell, "Raman spectroscopy on Mars: identification of geological and bio-geological signatures in martian analogues using miniaturized Raman spectrometers," *Philos. Trans. Royal Soc. A*, vol. 372, no. 2030, p. 20140204, 2014.

[86] F. Casadio, C. Daher, and L. Bellot-Gurlet, "Raman spectroscopy of cultural heritage materials: overview of applications and new frontiers in instrumentation, sampling modalities, and data processing," in *Analytical Chemistry for Cultural Heritage*, pp. 161–211, Springer, 2017.

[87] S. E. Bell, "Tutorial review. Time-resolved resonance Raman spectroscopy," *Analyst*, vol. 121, no. 11, pp. 107R–120R, 1996.

[88] P. Kukura, D. W. McCamant, and R. A. Mathies, "Femtosecond stimulated Raman spectroscopy," *Annu. Rev. Phys. Chem.*, vol. 58, pp. 461–488, 2007.

[89] R. R. Frontiera and R. A. Mathies, "Femtosecond stimulated Raman spectroscopy," *Laser Photonics Rev.*, vol. 5, no. 1, pp. 102–113, 2011.

[90] J. Dasgupta, R. Frontiera, C. Fang, and R. Mathies, "Femtosecond stimulated Raman spectroscopy," *Encyclopedia of Biophysics*, pp. 745–759, 2013.

[91] P. Kukura, R. Frontiera, and R. A. Mathies, "Direct observation of anharmonic coupling in the time domain with femtosecond stimulated Raman scattering," *Phys. Rev. Lett.*, vol. 96, no. 23, p. 238303, 2006.

[92] C. Fang, R. R. Frontiera, R. Tran, and R. A. Mathies, "Mapping GFP structure evolution during proton transfer with femtosecond Raman spectroscopy," *Nature*, vol. 462, no. 7270, pp. 200–204, 2009.

[93] D. P. Hoffman, S. R. Ellis, and R. A. Mathies, "Characterization of a conical intersection in a charge-transfer dimer with two-dimensional time-resolved stimulated Raman spectroscopy," *J. Phys. Chem. A*, vol. 118, no. 27, pp. 4955–4965, 2014.

[94] S. R. Ellis, D. P. Hoffman, M. Park, and R. A. Mathies, "Difference bands in time-resolved femtosecond stimulated Raman spectra of photoexcited intermolecular electron transfer from chloronaphthalene to tetracyanoethylene," *J. Phys. Chem. A*, vol. 122, no. 14, pp. 3594–3605, 2018.

[95] V. Balzani, *Electron Transfer in Chemistry*. Vch Verlagsgesellschaft Mbh, 2001.

[96] G. Saito and T. Murata, "Mixed valency in organic charge transfer complexes," *Philos. Trans. Royal Soc. A*, vol. 366, no. 1862, pp. 139–150, 2007.

[97] E. Sjulstok, J. M. H. Olsen, and I. A. Solov'yov, "Quantifying electron transfer reactions in biological systems: what interactions play the major role?," *SIAM Rev.*, vol. 5, p. 18446, 2015.

[98] A. de la Lande, N. S. Babcock, J. Řezáč, B. Lévy, B. C. Sanders, and D. R. Salahub, "Quantum effects in biological electron transfer," *Phys. Chem. Chem. Phys.*, vol. 14, no. 17, pp. 5902–5918, 2012.

[99] Y. Lin, Y. Li, and X. Zhan, "Small molecule semiconductors for high-efficiency organic photovoltaics," *Chem. Soc. Rev.*, vol. 41, no. 11, pp. 4245–4272, 2012.

[100] F. Liu, Z. Zhou, C. Zhang, T. Vergote, H. Fan, F. Liu, and X. Zhu, "A thieno [3, 4-b] thiophene-based non-fullerene electron acceptor for high-performance bulk-heterojunction organic solar cells," *J. Am. Chem. Soc.*, vol. 138, no. 48, pp. 15523–15526, 2016.

[101] A. V. Akimov, A. J. Neukirch, and O. V. Prezhdo, "Theoretical insights into photoinduced charge transfer and catalysis at oxide interfaces," *Chem. Rev.*, vol. 113, no. 6, pp. 4496–4565, 2013.

[102] Y. Cai and Y. P. Feng, "Review on charge transfer and chemical activity of TiO_2: mechanism and applications," *Prog. Surf. Sci.*, vol. 91, no. 4, pp. 183–202, 2016.

[103] J.-L. Brédas, D. Beljonne, V. Coropceanu, and J. Cornil, "Charge-transfer and energy-transfer processes in π-conjugated oligomers and polymers: A molecular picture," *Chem. Rev.*, vol. 104, no. 11, pp. 4971–5004, 2004.

[104] P. Roy, A. Jha, V. B. Yasarapudi, T. Ram, B. Puttaraju, S. Patil, and J. Dasgupta, "Ultrafast bridge planarization in donor-π-acceptor copolymers drives intramolecular charge transfer," *Nat. Chem.*, vol. 8, no. 1, p. 1716, 2017.

[105] W. R. Silva and R. R. Frontiera, "Excited state structural evolution during charge-transfer reactions in betaine-30," *Phys. Chem. Chem. Phys.*, vol. 18, no. 30, pp. 20290–20297, 2016.

[106] B. Carlotti, R. Flamini, I. Kikaš, U. Mazzucato, and A. Spalletti, "Intramolecular charge transfer, solvatochromism and hyperpolarizability of compounds bearing ethenylene or ethynylene bridges," *Chem. Phys.*, vol. 407, pp. 9–19, 2012.

[107] X. Niu, P. Gautam, Z. Kuang, P. Y. Craig, Y. Guo, H. Song, Q. Guo, J. M. Chan, and A. Xia, "Intramolecular charge transfer and solvation dynamics of push–pull dyes with different π-conjugated linkers," *Phys. Chem. Chem. Phys.*, vol. 21, no. 31, pp. 17323–17331, 2019.

[108] P. Arpaçay, P. Maity, A. M. El-Zohry, A. Meindl, S. Plunkett, S. Akca, M. O. Senge, W. J. Blau, and O. F. Mohammed, "Controllable charge-transfer mechanism at push-pull porphyrin/nanocarbon interfaces," *J. Phys. Chem. C*, no. 123, pp. 14283–14291, 2019.

[109] Q. Zhang, T. Komino, S. Huang, S. Matsunami, K. Goushi, and C. Adachi, "Triplet exciton confinement in green organic light-emitting diodes containing luminescent charge-transfer Cu(I) complexes," *Adv. Func. Mater.*, vol. 22, no. 11, pp. 2327–2336, 2012.

[110] M. G. Hilfiger, M. Chen, T. V. Brinzari, T. M. Nocera, M. Shatruk, D. T. Petasis, J. L. Musfeldt, C. Achim, and K. R. Dunbar, "An unprecedented charge transfer induced spin transition in an Fe–Os cluster," *Angew. Chem. Int. Ed.*, vol. 49, no. 8, pp. 1410–1413, 2010.

[111] Y.-J. Cho, S.-Y. Kim, M. Cho, K.-R. Wee, H.-J. Son, W.-S. Han, D. W. Cho, and S. O. Kang, "Ligand-to-ligand charge transfer in heteroleptic Ir-complexes: Comprehensive investigations of its fast dynamics and mechanism," *Phys. Chem. Chem. Phys.*, vol. 18, no. 22, pp. 15162–15169, 2016.

[112] P. Anderson, P. Lee, and M. Saitoh, "Remarks on giant conductivity in TTF-TCNQ," *Solid State Commun.*, vol. 13, no. 5, pp. 595–598, 1973.

[113] P. M. Grant, R. Greene, G. C. Wrighton, and G. Castro, "Temperature dependence of the near-Infrared optical properties of tetrathiofulvalinium tetracyanoquinodimethane (TTF-TCNQ)," *Phys. Rev. Lett.*, vol. 31, no. 21, p. 1311, 1973.

[114] J. Ferraris, D. Cowan, V. t. Walatka, and J. Perlstein, "Electron transfer in a new highly conducting donor-acceptor complex," *J. Am. Chem. Soc.*, vol. 95, no. 3, pp. 948–949, 1973.

[115] A. Bright, A. Garito, and A. J. Heeger, "Optical properties of (TTF)(TCNQ) in the visible and Infrared," *Solid State Commun.*, vol. 13, no. 7, pp. 943–948, 1973.

[116] K. P. Goetz, D. Vermeulen, M. E. Payne, C. Kloc, L. E. McNeil, and O. D. Jurchescu, "Charge-transfer complexes: New perspectives on an old class of compounds," *J. Mater. Chem. C*, vol. 2, no. 17, pp. 3065–3076, 2014.

[117] S. Ullbrich, J. Benduhn, X. Jia, V. C. Nikolis, K. Tvingstedt, F. Piersimoni, S. Roland, Y. Liu, J. Wu, A. Fischer, *et al.*, "Emissive and charge-generating donor–acceptor interfaces for organic optoelectronics with low voltage losses," *Nat. Mater.*, vol. 18, no. 5, p. 459, 2019.

[118] V. Lemaur, M. Steel, D. Beljonne, J.-L. Brédas, and J. Cornil, "Photoinduced charge generation and recombination dynamics in model donor/acceptor pairs for organic solar cell applications: a full quantum-chemical treatment," *J. Am. Chem. Soc.*, vol. 127, no. 16, pp. 6077–6086, 2005.

[119] J.-L. Brédas, J. E. Norton, J. Cornil, and V. Coropceanu, "Molecular understanding of organic solar cells: the challenges," *Acc. Chem. Res.*, vol. 42, no. 11, pp. 1691–1699, 2009.

[120] B. Kippelen and J.-L. Brédas, "Organic photovoltaics," *Energ. Environ. Sci.*, vol. 2, no. 3, pp. 251–261, 2009.

[121] C. Deibel, T. Strobel, and V. Dyakonov, "Role of the charge transfer state in organic donor–acceptor solar cells," *Adv. Mater.*, vol. 22, no. 37, pp. 4097–4111, 2010.

[122] D. S. Chemla, *Nonlinear Optical Properties of Organic Molecules and Crystals*, vol. 1. Elsevier, 2012.

[123] M. Khalid, R. Hussain, A. Hussain, B. Ali, F. Jaleel, M. Imran, M. A. Assiri, M. Usman Khan, S. Ahmed, S. Abid, *et al.*, "Electron donor and acceptor influence on the nonlinear optical response of diacetylene-functionalized organic materials (DFOMs): Density functional theory calculations," *Molecules*, vol. 24, no. 11, p. 2096, 2019.

[124] A. Popczyk, A. Aamoum, A. Migalska-Zalas, P. Płóciennik, A. Zawadzka, J. Mysliwiec, and B. Sahraoui, "Selected organometallic compounds for third order nonlinear optical application," *Nanomaterials*, vol. 9, no. 2, p. 254, 2019.

[125] R. Mulliken and W. B. Person, "Donor-acceptor complexes," *Annu. Rev. Phys. Chem.*, vol. 13, no. 1, pp. 107–126, 1962.

[126] R. S. Mulliken and W. B. Person, *Molecular complexes: a lecture and reprint volume*. Wiley-Interscience, 1969.

[127] H. Bakker, S. R. Meech, and E. J. Heilweil, "Time-resolved vibrational spectroscopy," 2018.

[128] T. Buckup and J. Léonard, *Multidimensional Time-Resolved Spectroscopy*. Springer, 2018.

[129] H. H. Fielding and G. A. Worth, "Using time-resolved photoelectron spectroscopy to unravel the electronic relaxation dynamics of photoexcited molecules," *Chem. Soc. Rev.*, vol. 47, no. 2, pp. 309–321, 2018.

[130] B. O. Roos, M. Fülscher, P.-Å. Malmqvist, M. Merchán, and L. Serrano-Andrés, "Theoretical studies of the electronic spectra of organic molecules," in *Quantum Mechanical Electronic Structure Calculations with Chemical Accuracy*, pp. 357–438, Springer, 1995.

[131] K. Hirao, *Recent Advances in Multireference Methods*, vol. 4. World Scientific, 1999.

[132] L. Serrano-Andrés and M. Merchán, "Quantum chemistry of the excited state: 2005 overview," *J. Mol. Struct.*, vol. 729, no. 1-2, pp. 99–108, 2005.

[133] J. Townsend, J. K. Kirkland, and K. D. Vogiatzis, "Post-Hartree-Fock methods: configuration interaction, many-body perturbation theory, coupled-cluster theory," in *Mathematical Physics in Theoretical Chemistry*, pp. 63–117, Elsevier, 2019.

[134] M. G. Delcey, L. K. Sørensen, M. Vacher, R. C. Couto, and M. Lundberg, "Efficient calculations of a large number of highly excited states for multiconfigurational wavefunctions," *J. Comput. Chem.*, vol. 40, pp. 1789—1799, 2019.

[135] M.-S. Liao, Y. Lu, and S. Scheiner, "Performance assessment of density-functional methods for study of charge-transfer complexes," *J. Comput. Chem.*, vol. 24, no. 5, pp. 623–631, 2003.

[136] T. Stein, L. Kronik, and R. Baer, "Reliable prediction of charge transfer excitations in molecular complexes using time-dependent density functional theory," *J. Am. Chem. Soc.*, vol. 131, no. 8, pp. 2818–2820, 2009.

[137] G. Sini, J. S. Sears, and J.-L. Brédas, "Evaluating the performance of DFT functionals in assessing the interaction energy and ground-state charge transfer of donor/acceptor complexes: Tetrathiafulvalene–tetracyanoquinodimethane (TTF-TCNQ) as a model case," *J. Chem. Theory Comput.*, vol. 7, no. 3, pp. 602–609, 2011.

[138] J. Arago, J. C. Sancho-Garcia, E. Orti, and D. Beljonne, "Ab initio modeling of donor–acceptor interactions and charge-transfer

excitations in molecular complexes: the case of terthiophene–tetracyanoquinodimethane," *J. Chem. Theory Comput.*, vol. 7, no. 7, pp. 2068–2077, 2011.

[139] S. Kümmel, "Charge-transfer excitations: A challenge for time-dependent density functional theory that has been met," *Adv. Energy Mater.*, vol. 7, no. 16, p. 1700440, 2017.

[140] A. Dreuw, J. L. Weisman, and M. Head-Gordon, "Long-range charge-transfer excited states in time-dependent density functional theory require non-local exchange," *J. Chem. Phys.*, vol. 119, no. 6, pp. 2943–2946, 2003.

[141] M. Dion, H. Rydberg, E. Schröder, D. C. Langreth, and B. I. Lundqvist, "van der Waals density functional for general geometries," *Phys. Rev. Lett.*, vol. 92, no. 24, p. 246401, 2004.

[142] A. Hesselmann, G. Jansen, and M. Schütz, "Density-functional theory-symmetry-adapted intermolecular perturbation theory with density fitting: a new efficient method to study intermolecular interaction energies," *J. Chem. Phys.*, vol. 122, no. 1, p. 014103, 2005.

[143] J.-D. Chai and M. Head-Gordon, "Long-range corrected hybrid density functionals with damped atom–atom dispersion corrections," *Phys. Chem. Chem. Phys.*, vol. 10, no. 44, pp. 6615–6620, 2008.

[144] O. A. Von Lilienfeld, I. Tavernelli, U. Rothlisberger, and D. Sebastiani, "Optimization of effective atom centered potentials for London dispersion forces in density functional theory," *Phys. Rev. Lett.*, vol. 93, no. 15, p. 153004, 2004.

[145] A. J. Cohen, P. Mori-Sánchez, and W. Yang, "Challenges for density functional theory," *Chem. Rev.*, vol. 112, no. 1, pp. 289–320, 2011.

[146] E. G. Hohenstein, S. T. Chill, and C. D. Sherrill, "Assessment of the performance of the M05- 2x and M06- 2x exchange-correlation functionals for noncovalent interactions in biomolecules," *J. Chem. Theory Comput.*, vol. 4, no. 12, pp. 1996–2000, 2008.

[147] K. E. Riley, M. Pitonák, P. Jurecka, and P. Hobza, "Stabilization and structure calculations for noncovalent interactions in extended molecular systems based on wave function and density functional theories," *Chem. Rev.*, vol. 110, no. 9, pp. 5023–5063, 2010.

[148] L. Ferrighi, Y.-x. Pan, H. Grönbeck, and B. Hammer, "Study of alkylthiolate self-assembled monolayers on Au (111) using a semilocal meta-GGA density functional," *J. Phys. Chem. C*, vol. 116, no. 13, pp. 7374–7379, 2012.

[149] L. Goerigk, "Treating London-dispersion effects with the latest Minnesota density functionals: problems and possible solutions," *J. Phys. Chem. Lett.*, vol. 6, no. 19, pp. 3891–3896, 2015.

[150] N. Mardirossian and M. Head-Gordon, "How accurate are the minnesota density functionals for noncovalent interactions, isomerization energies, thermochemistry, and barrier heights involving molecules composed of main-group elements?," *J. Chem. Theory Comput.*, vol. 12, no. 9, pp. 4303–4325, 2016.

[151] D. E. Taylor, J. G. Ángyán, G. Galli, C. Zhang, F. Gygi, K. Hirao, J. W. Song, K. Rahul, O. Anatole von Lilienfeld, R. Podeszwa, *et al.*, "Blind test of density-functional-based methods on intermolecular interaction energies," *J. Chem. Phys.*, vol. 145, no. 12, p. 124105, 2016.

[152] Y. Liu and W. A. I. Goddard, "A universal damping function for empirical dispersion correction on density functional theory," *Mater. Trans.*, vol. 50, no. 7, pp. 1664–1670, 2009.

[153] S. Grimme, S. Ehrlich, and L. Goerigk, "Effect of the damping function in dispersion corrected density functional theory," *J. Comput. Chem.*, vol. 32, no. 7, pp. 1456–1465, 2011.

[154] S. Grimme, "Density functional theory with London dispersion corrections," *WIREs Comput. Mol. Sci.*, vol. 1, no. 2, pp. 211–228, 2011.

[155] S. Ehrlich, J. Moellmann, and S. Grimme, "Dispersion-corrected density functional theory for aromatic interactions in complex systems," *Acc. Chem. Res.*, vol. 46, no. 4, pp. 916–926, 2012.

[156] T. Risthaus and S. Grimme, "Benchmarking of London dispersion-accounting density functional theory methods on very large molecular complexes," *J. Chem. Theory Comput.*, vol. 9, no. 3, pp. 1580–1591, 2013.

[157] S. Grimme, "Do special noncovalent π–π stacking interactions really exist?," *Angew. Chem. Int. Ed.*, vol. 47, no. 18, pp. 3430–3434, 2008.

[158] S. Grimme, "Accurate description of van der Waals complexes by density functional theory including empirical corrections," *J. Comput. Chem.*, vol. 25, no. 12, pp. 1463–1473, 2004.

[159] S. Grimme, "Semiempirical GGA-type density functional constructed with a long-range dispersion correction," *J. Comput. Chem.*, vol. 27, no. 15, pp. 1787–1799, 2006.

[160] E. A. Briggs and N. A. Besley, "Modelling excited states of weakly bound complexes with density functional theory," *Phys. Chem. Chem. Phys.*, vol. 16, no. 28, pp. 14455–14462, 2014.

[161] T. W. Kelley, P. F. Baude, C. Gerlach, D. E. Ender, D. Muyres, M. A. Haase, D. E. Vogel, and S. D. Theiss, "Recent progress in organic electronics: Materials, devices, and processes," *Chem. Mater.*, vol. 16, no. 23, pp. 4413–4422, 2004.

[162] C. Wöll, *Physical and Chemical Aspects of Organic Electronics: From Fundamentals to Functioning Devices*. John Wiley & Sons, 2009.

[163] R. Farchioni and G. Grosso, *Organic electronic materials: conjugated polymers and low molecular weight organic solids*, vol. 41. Springer Science & Business Media, 2013.

[164] Q. Miao, *Polycyclic Arenes and Heteroarenes: Synthesis, Properties, and Applications*. John Wiley & Sons, 2015.

[165] S. Rajaram, R. Shivanna, S. K. Kandappa, and K. Narayan, "Nonplanar perylene diimides as potential alternatives to fullerenes in organic solar cells," *J. Phys. Chem. Lett.*, vol. 3, no. 17, pp. 2405–2408, 2012.

[166] E. Kozma and M. Catellani, "Perylene diimides based materials for organic solar cells," *Dyes Pigm.*, vol. 98, no. 1, pp. 160–179, 2013.

[167] Y. Zhong, M. T. Trinh, R. Chen, W. Wang, P. P. Khlyabich, B. Kumar, Q. Xu, C.-Y. Nam, M. Y. Sfeir, C. Black, *et al.*, "Efficient organic solar cells with helical perylene diimide electron acceptors," *J. Am. Chem. Soc.*, vol. 136, no. 43, pp. 15215–15221, 2014.

[168] D. Meng, D. Sun, C. Zhong, T. Liu, B. Fan, L. Huo, Y. Li, W. Jiang, H. Choi, T. Kim, *et al.*, "High-performance solution-processed non-fullerene organic solar cells based on selenophene-containing perylene bisimide acceptor," *J. Am. Chem. Soc.*, vol. 138, no. 1, pp. 375–380, 2015.

[169] A. Zhang, C. Li, F. Yang, J. Zhang, Z. Wang, Z. Wei, and W. Li, "An electron acceptor with porphyrin and perylene bisimides for efficient non-fullerene solar cells," *Angew. Chem. Int. Ed.*, vol. 56, no. 10, pp. 2694–2698, 2017.

[170] Y. Terao, H. Sasabe, and C. Adachi, "Correlation of hole mobility, exciton diffusion length, and solar cell characteristics in phthalocyanine/fullerene organic solar cells," *Appl. Phys. Lett.*, vol. 90, no. 10, p. 103515, 2007.

[171] A. Pivrikas, N. S. Sariciftci, G. Juška, and R. Österbacka, "A review of charge transport and recombination in polymer/fullerene organic solar cells," *Prog. Photovoltaics.*, vol. 15, no. 8, pp. 677–696, 2007.

[172] S. Pfuetzner, J. Meiss, A. Petrich, M. Riede, and K. Leo, "Improved bulk heterojunction organic solar cells employing C70 fullerenes," *Appl. Phys. Lett.*, vol. 94, no. 22, p. 145, 2009.

[173] I. A. Howard, R. Mauer, M. Meister, and F. Laquai, "Effect of morphology on ultrafast free carrier generation in polythiophene: fullerene organic solar cells," *J. Am. Chem. Soc.*, vol. 132, no. 42, pp. 14866–14876, 2010.

[174] P. Sonar, J. P. F. Lim, and K. L. Chan, "Organic non-fullerene acceptors for organic photovoltaics," *Energ. Environ. Sci.*, vol. 4, no. 5, pp. 1558–1574, 2011.

[175] P. E. Schwenn, K. Gui, A. M. Nardes, K. B. Krueger, K. H. Lee, K. Mutkins, H. Rubinstein-Dunlop, P. E. Shaw, N. Kopidakis, P. L. Burn, *et al.*, "A small molecule non-fullerene electron acceptor for organic solar cells," *Adv. Energy Mater.*, vol. 1, no. 1, pp. 73–81, 2011.

[176] Y. Lin and X. Zhan, "Non-fullerene acceptors for organic photovoltaics: an emerging horizon," *Mater. Horiz.*, vol. 1, no. 5, pp. 470–488, 2014.

[177] C. B. Nielsen, S. Holliday, H.-Y. Chen, S. J. Cryer, and I. McCulloch, "Non-fullerene electron acceptors for use in organic solar cells," *Acc. Chem. Res.*, vol. 48, no. 11, pp. 2803–2812, 2015.

[178] D. Sun, D. Meng, Y. Cai, B. Fan, Y. Li, W. Jiang, L. Huo, Y. Sun, and Z. Wang, "Non-fullerene-acceptor-based bulk-heterojunction organic solar cells with efficiency over 7%," *J. Am. Chem. Soc.*, vol. 137,

no. 34, pp. 11156–11162, 2015.

[179] K. Cnops, G. Zango, J. Genoe, P. Heremans, M. V. Martinez-Diaz, T. Torres, and D. Cheyns, "Energy level tuning of non-fullerene acceptors in organic solar cells," *J. Am. Chem. Soc.*, vol. 137, no. 28, pp. 8991–8997, 2015.

[180] W. Ni, M. Li, B. Kan, F. Liu, X. Wan, Q. Zhang, H. Zhang, T. P. Russell, and Y. Chen, "Fullerene-free small molecule organic solar cells with a high open circuit voltage of 1.15 V," *Chem. Commun.*, vol. 52, no. 3, pp. 465–468, 2016.

[181] J. Hou, O. Inganäs, R. H. Friend, and F. Gao, "Organic solar cells based on non-fullerene acceptors," *Nat. Mater.*, vol. 17, no. 2, pp. 119–128, 2018.

[182] X. Gu, W. A. Luhman, E. Yagodkin, R. J. Holmes, and C. J. Douglas, "Diarylindenotetracenes via a selective cross-coupling/c–h functionalization: Electron donors for organic photovoltaic cells," *Org. Lett.*, vol. 14, no. 6, pp. 1390–1393, 2012.

[183] L. J. Purvis, X. Gu, S. Ghosh, Z. Zhang, C. J. Cramer, and C. J. Douglas, "Synthesis and characterization of electron-deficient asymmetrically substituted diarylindenotetracenes," *J. Org. Chem.*, vol. 83, no. 4, pp. 1828–1841, 2018.

[184] W. Shockley and H. J. Queisser, "Detailed balance limit of efficiency of p-n junction solar cells," *J. Appl. Phys.*, vol. 32, no. 3, pp. 510–519, 1961.

[185] M. Hanna and A. Nozik, "Solar conversion efficiency of photovoltaic and photoelectrolysis cells with carrier multiplication absorbers," *J. Appl. Phys.*, vol. 100, no. 7, p. 074510, 2006.

[186] M. B. Smith and J. Michl, "Singlet fission," *Chem. Rev.*, vol. 110, no. 11, pp. 6891–6936, 2010.

[187] M. B. Smith and J. Michl, "Recent advances in singlet fission," *Annu. Rev. Phys. Chem.*, vol. 64, pp. 361–386, 2013.

[188] J. C. Johnson, A. J. Nozik, and J. Michl, "High triplet yield from singlet fission in a thin film of 1, 3-diphenylisobenzofuran," *J. Am. Chem. Soc.*, vol. 132, no. 46, pp. 16302–16303, 2010.

[189] A. D. Poletayev, J. Clark, M. W. Wilson, A. Rao, Y. Makino, S. Hotta, and R. H. Friend, "Triplet dynamics in pentacene crystals: Applications to fission-sensitized photovoltaics," *Adv. Mater.*, vol. 26, no. 6, pp. 919–924, 2014.

[190] D. N. Congreve, J. Lee, N. J. Thompson, E. Hontz, S. R. Yost, P. D. Reusswig, M. E. Bahlke, S. Reineke, T. Van Voorhis, and M. A. Baldo, "External quantum efficiency above 100% in a singlet-exciton-fission–based organic photovoltaic cell," *Science*, vol. 340, no. 6130, pp. 334–337, 2013.

[191] S. Singh, W. Jones, W. Siebrand, B. Stoicheff, and W. Schneider, "Laser generation of excitons and fluorescence in anthracene crystals," *J. Chem. Phys.*, vol. 42, no. 1, pp. 330–342, 1965.

[192] I. Paci, J. C. Johnson, X. Chen, G. Rana, D. Popović, D. E. David, A. J. Nozik, M. A. Ratner, and J. Michl, "Singlet fission for dye-sensitized solar cells: Can a suitable sensitizer be found?," *J. Am. Chem. Soc.*, vol. 128, no. 51, pp. 16546–16553, 2006.

[193] L. Melby, R. Harder, W. Hertler, W. Mahler, R. Benson, and W. Mochel, "Substituted quinodimethans. II. Anion-radical derivatives and complexes of 7, 7, 8, 8-tetracyanoquinodimethan," *J. Am. Chem. Soc.*, vol. 84, no. 17, pp. 3374–3387, 1962.

[194] M. J. Cohen, L. Coleman, A. Garito, and A. Heeger, "Electrical conductivity of tetrathiofulvalinium tetracyanoquinodimethan (TTF)(TCNQ)," *Phys. Rev. B*, vol. 10, no. 4, p. 1298, 1974.

[195] J. B. Torrance, "The difference between metallic and insulating salts of tetracyanoquinodimethone (TCNQ): how to design an organic metal," *Acc. Chem. Res.*, vol. 12, no. 3, pp. 79–86, 1979.

[196] T.-C. Tseng, C. Urban, Y. Wang, R. Otero, S. L. Tait, M. Alcamí, D. Écija, M. Trelka, J. M. Gallego, N. Lin, *et al.*, "Charge-transfer-induced structural rearrangements at both sides of organic/metal interfaces," *Nat. Chem.*, vol. 2, no. 5, p. 374, 2010.

[197] M. G. Kaplunov, T. P. Panova, E. B. Yagubskii, and Y. G. Borod'ko, "The vibrational spectra of tetracyanoquinodimethane and its complexes," *J. Struct. Chem.*, vol. 13, pp. 411–417, 1972.

[198] H. Tamaya, Y. Torii, T. Ishikawa, H. Nakano, and T. Iimori, "Photophysics and inverted solvatochromism of 7,7,8,8-tetracyanoquinodimethane (TCNQ)," *ChemPhysChem*, vol. 20, pp. 2531–2538, 2019.

[199] R. Otero, R. Miranda, and J. M. Gallego, "A comparative computational study of the adsorption of TCNQ and F4-TCNQ on the coinage metal surfaces," *ACS Omega*, vol. 4, no. 16, pp. 16906–16915, 2019.

[200] R. Berera, R. van Grondelle, and J. T. Kennis, "Ultrafast transient absorption spectroscopy: Principles and application to photosynthetic systems," *Photosynth. Res.*, vol. 101, no. 2-3, pp. 105–118, 2009.

[201] M. A. Robb, *Theoretical Chemistry for Electronic Excited States*, vol. 12. Royal Society of Chemistry, 2018.

[202] A. D. Becke, "Density-functional thermochemistry. III. The role of exact exchange," *J. Chem. Phys.*, vol. 98, p. 5648, 1993.

[203] C. Lee, W. Yang, and R. G. Parr, "Development of the Colle-Salvetti correlation-energy formula into a functional of the electron density," *Phys. Rev. B*, vol. 37, no. 2, p. 785, 1988.

[204] B. Miehlich, A. Savin, H. Stoll, and H. Preuss, "Results obtained with the correlation energy density functionals of Becke and Lee, Yang and Parr," *Chem. Phys. Lett.*, vol. 157, no. 3, pp. 200–206, 1989.

[205] T. Yanai, D. P. Tew, and N. C. Handy, "A new hybrid exchange–correlation functional using the Coulomb-Attenuating Method (CAM-B3LYP)," *Chem. Phys. Lett.*, vol. 393, no. 1-3, pp. 51–57, 2004.

[206] R. Kobayashi and R. D. Amos, "The application of CAM-B3LYP to the charge-transfer band problem of the zincbacteriochlorin–bacteriochlorin complex," *Chem. Phys. Lett.*, vol. 420, no. 1-3, pp. 106–109, 2006.

[207] Z.-L. Cai, M. J. Crossley, J. R. Reimers, R. Kobayashi, and R. D. Amos, "Density functional theory for charge transfer: the nature of the n-bands of porphyrins and chlorophylls revealed through CAM-B3LYP, CASPT2, and SAC-CI calculations," *J. Phys. Chem. B*, vol. 110, no. 31, pp. 15624–15632, 2006.

[208] I. V. Rostov, R. D. Amos, R. Kobayashi, G. Scalmani, and M. J. Frisch, "Studies of the ground and excited-state surfaces of the retinal chromophore using CAM-B3LYP," *J. Phys. Chem. B*, vol. 114, no. 16, pp. 5547–5555, 2010.

[209] R. Li, J. Zheng, and D. G. Truhlar, "Density functional approximations for charge transfer excitations with intermediate spatial overlap," *Phys. Chem. Chem. Phys.*, vol. 12, no. 39, pp. 12697–12701, 2010.

[210] M. Petersilka, U. Gossmann, and E. Gross, "Excitation energies from time-dependent density-functional theory," *Phys. Rev. Lett.*, vol. 76, no. 8, p. 1212, 1996.

[211] B. Champagne, E. A. Perpète, S. J. van Gisbergen, E.-J. Baerends, J. G. Snijders, C. Soubra-Ghaoui, K. A. Robins, and B. Kirtman, "Assessment of conventional density functional schemes for computing the polarizabilities and hyperpolarizabilities of conjugated oligomers: an ab initio investigation of polyacetylene chains," *J. Chem. Phys.*, vol. 109, no. 23, pp. 10489–10498, 1998.

[212] A. Dreuw and M. Head-Gordon, "Failure of time-dependent density functional theory for long-range charge-transfer excited states: the zincbacteriochlorin-bacteriochlorin and bacteriochlorophyll-spheroidene complexes," *J. Am. Chem. Soc.*, vol. 126, no. 12, pp. 4007–4016, 2004.

[213] R. Magyar and S. Tretiak, "Dependence of spurious charge-transfer excited states on orbital exchange in TDDFT: Large molecules and clusters," *J. Chem. Theory Comput.*, vol. 3, no. 3, pp. 976–987, 2007.

[214] M. J. Peach, P. Benfield, T. Helgaker, and D. J. Tozer, "Excitation energies in density functional theory: an evaluation and a diagnostic test," *J. Chem. Phys.*, vol. 128, no. 4, p. 044118, 2008.

[215] A. D. Dwyer and D. J. Tozer, "Effect of chemical change on TDDFT accuracy: Orbital overlap perspective of the hydrogenation of retinal," *Phys. Chem. Chem. Phys.*, vol. 12, no. 12, pp. 2816–2818, 2010.

[216] H. Iikura, T. Tsuneda, T. Yanai, and K. Hirao, "A long-range correction scheme for generalized-gradient-approximation exchange functionals," *J. Chem. Phys.*, vol. 115, no. 8, pp. 3540–3544, 2001.

[217] T. Stein, L. Kronik, and R. Baer, "Prediction of charge-transfer excitations in coumarin-based dyes using a range-separated functional tuned from first principles," *J. Chem. Phys.*, vol. 131, no. 24, p. 244119, 2009.

[218] B. M. Wong, M. Piacenza, and F. Della Sala, "Absorption and fluorescence properties of oligothiophene biomarkers from long-range-corrected time-dependent density functional theory," *Phys. Chem. Chem. Phys.*, vol. 11, no. 22, pp. 4498–4508, 2009.

[219] N. Mardirossian, J. A. Parkhill, and M. Head-Gordon, "Benchmark results for empirical post-GGA functionals: Difficult exchange problems and independent tests," *Phys. Chem. Chem. Phys.*, vol. 13, no. 43, pp. 19325–19337, 2011.

[220] A. D. Laurent and D. Jacquemin, "TD-DFT benchmarks: a review," *Int. J. Quant. Chem.*, vol. 113, no. 17, pp. 2019–2039, 2013.

[221] R. Derian, K. Tokar, B. Somogyi, A. Gali, and I. Stich, "Optical gaps in pristine and heavily doped silicon nanocrystals: DFT versus quantum Monte Carlo benchmarks," *J. Chem. Theory Comput.*, vol. 13, no. 12, pp. 6061–6067, 2017.

[222] A. Petrone, R. A. Beck, J. M. Kasper, X. Li, Y. Huang, M. Crane, and P. Pauzauskie, "Electronic structures and spectroscopic signatures of silicon-vacancy containing nanodiamonds," *Phys. Rev. B*, vol. 98, no. 20, p. 205405, 2018.

[223] J. P. Perdew, M. Ernzerhof, and K. Burke, "Rationale for mixing exact exchange with density functional approximations," *J. Chem. Phys.*, vol. 105, no. 22, pp. 9982–9985, 1996.

[224] C. Adamo and V. Barone, "Toward reliable density functional methods without adjustable parameters: the PBE0 model," *J. Chem. Phys.*, vol. 110, no. 13, pp. 6158–6170, 1999.

[225] S. Grimme, S. Ehrlich, and L. Goerigk, "Effect of the damping function in dispersion corrected density functional theory," *J. Comput. Chem.*, vol. 32, no. 7, pp. 1456–1465, 2011.

[226] S. Grimme, J. Antony, S. Ehrlich, and H. Krieg, "A consistent and accurate ab initio parametrization of density functional dispersion correction (DFT-D) for the 94 elements H-Pu," *J. Chem. Phys.*, vol. 132,

no. 15, p. 154104, 2010.

[227] M. J. Frisch, G. W. Trucks, H. B. Schlegel, G. E. Scuseria, M. A. Robb, J. R. Cheeseman, G. Scalmani, V. Barone, G. A. Petersson, H. Nakatsuji, X. Li, M. Caricato, A. V. Marenich, J. Bloino, B. G. Janesko, R. Gomperts, B. Mennucci, H. P. Hratchian, J. V. Ortiz, A. F. Izmaylov, J. L. Sonnenberg, D. Williams-Young, F. Ding, F. Lipparini, F. Egidi, J. Goings, B. Peng, A. Petrone, T. Henderson, D. Ranasinghe, V. G. Zakrzewski, J. Gao, N. Rega, G. Zheng, W. Liang, M. Hada, M. Ehara, K. Toyota, R. Fukuda, J. Hasegawa, M. Ishida, T. Nakajima, Y. Honda, O. Kitao, H. Nakai, T. Vreven, K. Throssell, J. A. Montgomery, Jr., J. E. Peralta, F. Ogliaro, M. J. Bearpark, J. J. Heyd, E. N. Brothers, K. N. Kudin, V. N. Staroverov, T. A. Keith, R. Kobayashi, J. Normand, K. Raghavachari, A. P. Rendell, J. C. Burant, S. S. Iyengar, J. Tomasi, M. Cossi, J. M. Millam, M. Klene, C. Adamo, R. Cammi, J. W. Ochterski, R. L. Martin, K. Morokuma, O. Farkas, J. B. Foresman, and D. J. Fox, "Gaussian~16 Revision A.06," 2016. Gaussian Inc. Wallingford CT.

[228] J. M. Millam, V. Bakken, W. Chen, W. L. Hase, and H. B. Schlegel, "Ab initio classical trajectories on the Born–Oppenheimer surface: Hessian-based integrators using fifth-order polynomial and rational function fits," *J. Chem. Phys.*, vol. 111, no. 9, pp. 3800–3805, 1999.

[229] K. Bolton, W. Hase, and G. Peslherbe, "Modern methods for multidimensional dynamics computation in chemistry," *Direct dynamics of reactive systems. World Scientific, Singapore*, p. 143, 1998.

[230] E. Glendening, A. Reed, and J. Carpenter, "NBO version 3.1.(b) glendening, ed; weinhold, f," *J. Comput. Chem.*, vol. 19, p. 628, 1998.

[231] F. Weinhold, "Natural bond orbital analysis: a critical overview of relationships to alternative bonding perspectives," *J. Comput. Chem.*, vol. 33, no. 30, pp. 2363–2379, 2012.

[232] A. E. Reed, L. A. Curtiss, and F. Weinhold, "Intermolecular interactions from a natural bond orbital, donor-acceptor viewpoint," *Chem. Rev.*, vol. 88, no. 6, pp. 899–926, 1988.

[233] A. E. Reed, R. B. Weinstock, and F. Weinhold, "Natural population analysis," *J. Chem. Phys.*, vol. 83, no. 2, pp. 735–746, 1985.

[234] F. Weinhold, C. Landis, and E. Glendening, "What is NBO analysis and how is it useful?," *Int. Rev. Phys. Chem.*, vol. 35, no. 3, pp. 399–440, 2016.

[235] S. J. Grabowski, "Non-covalent interactions–QTAIM and NBO analysis," *J. Mol. Mod.*, vol. 19, no. 11, pp. 4713–4721, 2013.

[236] I. Garcıa-Cuesta, A. M. Sánchez de Merás, and H. Koch, "Coupled cluster calculations of the vertical excitation energies of tetracyanoethylene," *J. Chem. Phys.*, vol. 118, no. 18, pp. 8216–8222, 2003.

[237] J. C. Stires Iv, E. J. McLaurin, and C. P. Kubiak, "Infrared spectroscopic determination of the degree of charge transfer in complexes of TCNE with methyl-substituted benzenes," *Chem. Commun.*, no. 28, pp. 3532–3534, 2005.

[238] B. Milián, R. Pou-Amérigo, M. Merchán, and E. Ortí, "Theoretical study of the electronic excited states of tetracyanoethylene and its radical anion," *Comp. Phys. Comm.*, vol. 6, no. 3, pp. 503–510, 2005.

[239] I. Rubtsov and K. Yoshihara, "Vibrational coherence in electron donor-acceptor complexes," *J. Phys. Chem. A*, vol. 103, no. 49, pp. 10202–10212, 1999.

[240] N. S. Kumar, M. D. Gujrati, and J. N. Wilson, "Evidence of preferential π-stacking: a study of intermolecular and intramolecular charge transfer complexes," *Chem. Commun.*, vol. 46, no. 30, pp. 5464–5466, 2010.

[241] J. Tomasi, B. Mennucci, and R. Cammi, "Quantum mechanical continuum solvation models," *Chem. Rev.*, vol. 105, no. 8, pp. 2999–3094, 2005.

[242] G. Brancato, N. Rega, and V. Barone, "A hybrid explicit/implicit solvation method for first-principle molecular dynamics simulations," *J. Chem. Phys.*, vol. 128, no. 14, p. 04B607, 2008.

[243] M. Cossi, V. Barone, R. Cammi, and J. Tomasi, "Ab initio study of solvated molecules: a new implementation of the polarizable continuum model," *Chem. Phys. Lett.*, vol. 255, no. 4-6, pp. 327–335, 1996.

[244] M. Cossi, G. Scalmani, N. Rega, and V. Barone, "New developments in the polarizable continuum model for quantum mechanical and classical

calculations on molecules in solution," *J. Chem. Phys.*, vol. 117, no. 1, pp. 43–54, 2002.

[245] B. Mennucci, "Polarizable continuum model," *WIREs Comput. Mol. Sci.*, vol. 2, no. 3, pp. 386–404, 2012.

[246] M. Cossi and V. Barone, "Solvent effect on vertical electronic transitions by the polarizable continuum model," *J. Chem. Phys.*, vol. 112, no. 5, pp. 2427–2435, 2000.

[247] G. García, C. Adamo, and I. Ciofini, "Evaluating push–pull dye efficiency using TD-DFT and charge transfer indices," *Phys. Chem. Chem. Phys.*, vol. 15, no. 46, pp. 20210–20219, 2013.

[248] M. Savarese, U. Raucci, C. Adamo, P. A. Netti, I. Ciofini, and N. Rega, "Non-radiative decay paths in rhodamines: New theoretical insights," *Phys. Chem. Chem. Phys.*, vol. 16, no. 38, pp. 20681–20688, 2014.

[249] M. Campetella, F. Maschietto, M. J. Frisch, G. Scalmani, I. Ciofini, and C. Adamo, "Charge transfer excitations in TDDFT: A ghost-hunter index," *J. Comput. Chem.*, vol. 38, no. 25, pp. 2151–2156, 2017.

[250] F. Maschietto, M. Campetella, M. J. Frisch, G. Scalmani, C. Adamo, and I. Ciofini, "How are the charge transfer descriptors affected by the quality of the underpinning electronic density?," *J. Comput. Chem.*, vol. 39, no. 12, pp. 735–742, 2018.

[251] M. Campetella, A. Perfetto, and I. Ciofini, "Quantifying partial hole-particle distance at the excited state: a revised version of the DCT index," *Chem. Phys. Lett.*, vol. 714, pp. 81–86, 2019.

[252] R. Send and F. Furche, "First-order nonadiabatic couplings from time-dependent hybrid density functional response theory: Consistent formalism, implementation, and performance," *J. Chem. Phys.*, vol. 132, no. 4, p. 044107, 2010.

[253] D. B. Lingerfelt, D. B. Williams-Young, A. Petrone, and X. Li, "Direct ab initio (meta-) surface-hopping dynamics," *J. Chem. Theory Comput.*, vol. 12, no. 3, pp. 935–945, 2016.

[254] J. S. Miller, "Tetracyanoethylene (TCNE): the characteristic geometries and vibrational absorptions of its numerous structures," *Angew. Chem. Int. Ed.*, vol. 45, no. 16, pp. 2508–2525, 2006.

[255] R. E. Del Sesto, J. S. Miller, P. Lafuente, and J. J. Novoa, "Exceptionally long ($\geq$ 2.9 å) CC bonding interactions in π-$[TCNE]_2^{2-}$ dimers: Two-electron four-center cation-mediated CC bonding interactions involving π* electrons," *Chem. Eur. J.*, vol. 8, no. 21, pp. 4894–4908, 2002.

[256] B. M. Britt, H. B. Lueck, and J. L. McHale, "Application of transform theory to the resonance Raman spectra of the 1:1 hexamethylbenzene:TCNE electron donor—acceptor complex," *Chem. Phys. Lett.*, vol. 190, no. 6, pp. 528–532, 1992.

[257] K. Kulinowski, I. R. Gould, and A. B. Myers, "Absorption, fluorescence, and resonance Raman spectroscopy of the hexamethylbenzene/tetracyanoethylene charge-transfer complex: Toward a self-consistent model," *J. Phys. Chem.*, vol. 99, no. 22, pp. 9017–9026, 1995.

[258] D. L. Jeanmaire, M. R. Suchanski, and R. P. Van Duyne, "Resonance Raman spectroelectrochemistry. I. Tetracyanoethylene anion radical," *J. Am. Chem. Soc.*, vol. 97, no. 7, pp. 1699–1707, 1975.

[259] F. Markel, N. S. Ferris, I. R. Gould, and A. B. Myers, "Mode-specific vibrational reorganization energies accompanying photoinduced electron transfer in the hexamethylbenzene/tetracyanoethylene charge-transfer complex," *J. Am. Chem. Soc.*, vol. 114, no. 15, pp. 6208–6219, 1992.

[260] K. Kaya, A. Nakatsuka, N. Kubota, and M. Ito, "Charge transfer excited state of electron-donor-acceptor complex as an intermediate electronic state of the vibrational Raman scattering," *J. Raman Spectrosc.*, vol. 1, no. 6, pp. 595–604, 1973.

[261] M. Rossi and E. Haselbach, "Spectral properties of some weak electron-donor-acceptor (EDA)-complexes in the far infrared (FIR.) region (40–400 cm^{-1})," *Helv. Chim. Acta*, vol. 62, no. 1, pp. 140–151, 1979.

[262] M. Hayashi, T.-S. Yang, J. Yu, A. Mebel, and S. Lin, "On the theoretical investigation on spectroscopy of the electron donor-acceptor complex TCNE-HMB," *J. Phys. Chem. A*, vol. 101, no. 23, pp. 4156–4162, 1997.

[263] J. Stanley, D. Smith, B. Latimer, and J. Devlin, "The Infrared spectra of the anion and weak charge-transfer complexes of tetracyanoethylene," *J. Phys. Chem.*, vol. 70, no. 6, pp. 2011–2016, 1966.

[264] C. Jurgensen, M. Peanasky, and H. Drickamer, "The effect of high pressure on the electronic and Infrared spectra of TCNE and its charge transfer complexes with hexamethylbenzene," *J. Chem. Phys.*, vol. 83, no. 12, pp. 6108–6112, 1985.

[265] D. A. Dixon and J. S. Miller, "Crystal and molecular structure of the charge-transfer salt of decamethylcobaltocene and tetracyanoethylene (2:1):$\{[Co(C_5Me_5)_2]^+\}_2$ $[(NC)_2CC(CN)_2]^{2-}$. The electronic structures and spectra of $[TCNE]^n$ (n= 0, 1-, 2-)," *J. Am. Chem. Soc.*, vol. 109, no. 12, pp. 3656–3664, 1987.

[266] D. T. Chase, A. G. Fix, B. D. Rose, C. D. Weber, S. Nobusue, C. E. Stockwell, L. N. Zakharov, M. C. Lonergan, and M. M. Haley, "Electron-accepting 6, 12-diethynylindeno [1, 2-b] fluorenes: synthesis, crystal structures, and photophysical properties," *Angew. Chem. Int. Ed.*, vol. 50, no. 47, pp. 11103–11106, 2011.

[267] T. Taima, J. Sakai, T. Yamanari, and K. Saito, "Realization of large open-circuit photovoltage in organic thin-film solar cells by controlling measurement environment," *Jpn. J. Appl. Phys.*, vol. 45, no. 10L, p. L995, 2006.

[268] M. D. Perez, C. Borek, S. R. Forrest, and M. E. Thompson, "Molecular and morphological influences on the open circuit voltages of organic photovoltaic devices," *J. Am. Chem. Soc.*, vol. 131, no. 26, pp. 9281–9286, 2009.

[269] H. Najafov, B. Lee, Q. Zhou, L. C. Feldman, and V. Podzorov, "Observation of long-range exciton diffusion in highly ordered organic semiconductors," *Nat. Mater.*, vol. 9, no. 11, pp. 938–943, 2010.

[270] S. M. Hart, W. R. Silva, and R. R. Frontiera, "Femtosecond stimulated Raman evidence for charge-transfer character in pentacene singlet fission," *Chem. Sci.*, vol. 9, no. 5, pp. 1242–1250, 2018.

[271] K. Bera, C. J. Douglas, and R. R. Frontiera, "Femtosecond Raman microscopy reveals structural dynamics leading to triplet separation in

rubrene singlet fission," *J. Phys. Chem. Lett.*, vol. 8, no. 23, pp. 5929–5934, 2017.

[272] R. L. Martin, "Natural transition orbitals," *J. Chem. Phys.*, vol. 118, no. 11, pp. 4775–4777, 2003.

[273] J. J. Burdett and C. J. Bardeen, "The dynamics of singlet fission in crystalline tetracene and covalent analogs," *Accounts of chemical research*, vol. 46, no. 6, pp. 1312–1320, 2013.

[274] WaveMetrics, Inc., "Igor pro; v. 7.08; https://www.wavemetrics.com/."